New Optical Method for Heat Flux Measurements in Stagnation Point Laminar Methane/Air Flames and Hydrogen/Methane/Air Flames using Thermographic Phosphors

Von der Fakultät für Ingenieurwissenschaften, Abteilung Maschinenbau der
Universität Duisburg-Essen
zur Erlangung des akademischen Grades

DOKTOR-INGENIEUR

genehmigte Dissertation

von

Mohamed Salem Elmnefi
aus
Benghazi / Libyen

Referent: Univ.-Prof. Dr. rer. nat. Burak Atakan
Korreferent: Univ.-Prof. Dr. rer. nat. Volker Buck
Tag der mündlichen Prüfung: 24.11.2010

Abstract

In the present study, a new optical method was implemented to study the heat transfer from flat stagnation point flames which can be regarded as one-dimensional in the central part. Premixed methane-air flames and hydrogen-methane-air flames were investigated. The effects of burner-to-plate distance and the fresh gas mixture velocity on heat transfer were examined. Experiments were performed using light induced phosphorescence from thermographic phosphors to study the wall temperatures and heat fluxes of nearly one-dimensional flat premixed flames impinging upward normally on a horizontal water cooled circular flat plate.

The investigated flames were stoichiometric, lean and rich laminar methane/air flames with different equivalence ratios of φ =1, φ = 0.75 and φ = 1.25 and stoichiometric laminar hydrogen/methane/air flames. Mixtures of air with 10, 25, 50 and 75 % hydrogen in methane (CH_4) as well as a pure hydrogen flames at ambient pressure were investigated. The central part of this plate was an alumina ceramic plate coated from both sides with chromium doped alumina (ruby) and excited with a Nd:YAG laser or a green light emitting diode (LED) array to measure the wall temperature from both sides and thus the heat flux rate from the flame. The outlet velocity of the gases was varied from 0.1 m/s to 1.2 m/s. The burner to plate distance ranged from 0.5 to 2 times the burner exit diameter (d = 30 mm).The accuracy of the method was evaluated. The measured heat flux indicate the change of the flame stabilization mechanism from a burner stabilized to a stagnation plate stabilized flame.

The results were compared to modeling results of a one dimensional stagnation point flow, with a detailed reaction mechanism. In order to prove the model, also measured gas phase temperatures by OH LIF for a stoichiometric stagnation point flame were discussed. It turns out that the flame stabilization mechanism and with it the heat fluxes change from low to high mass fluxes. This experimental setup should be well suited for further studies of the flame wall interaction.

Zusammenfassung

In der vorliegenden Arbeit wurde eine neue optische Methode zur Untersuchung der Wärmeübertragung bei ebenen eindimensionalen Flammen in Staupunktgeometrie eingesetzt. Untersucht wurden vorgemischte Methan-Luft- und Wasserstoff-Methan-Luft-Flammen und der Einfluss des Abstands von Brenner zu Platte sowie der Geschwindigkeit der Frischgasmischung auf die Wärmeübertragung. Mittels Licht-induzierter Phosphoreszenz von thermographischen Phosphoren wurde die Oberflächen-temperatur gemessen. Aus den Oberflächentemperaturen konnte anschließend die Wärmestromdichte durch eine Keramikplatte, die von der einen Seite mit Wasser gekühlt und von der anderen Seite mit der 1-dimensionalen Flamme beheizt wurde, berechnet werden.Die untersuchten Flammen waren stöchiometrische, magere und brennstoffreiche Methan-Luft-Flammen mit Äquivalenzverhältnissen von φ=1, φ=0,75 und φ=1,25, sowie stöchio-metrisch-laminare Wasserstoff-Methan-Luft-Flammen mit 10%, 25%, 50% und 75% Wasser-stoff in Methan, sowie reine Wasserstoffflammen. Der zentrale Teil des Aufbaus ist eine Platte aus Aluminiumoxid-Keramik, die von beiden Seiten mit chrom-dotiertem Aluminium-oxid (Rubin) beschichtet ist. Diese wurde auf der Flammenseite mit einem Nd:YAG-Laser (532 nm) oder einer Licht-emittierenden Diode (LED) (530 nm) und auf der Wasserseite mit einer LED (530 nm) zur Phosphoreszenz angeregt. Mit dieser Messmethode kann die Wandtemperatur von beiden Seiten gemessen und die Wärmestromdichte durch die Platte berechnet werden, die Genauigkeit des Verfahrens wird diskutiert und ist relativ hoch. Die Austrittsgeschwindigkeit der Gase wurde von 0,1 bis 1,2 m/s variiert. Der Abstand zwischen Brenner und Platte war 0,5 bis 2-mal so groß wie der Brennerdurchmesser (d=30 mm).

Die berechneten Wärmestromdichten zeigen die Änderung des Flammenstabilisierungs-mechanismus von einer brennerstabilisierten zu einer stauplattenstabilisierten Flamme.Die Ergebnisse wurden mit den Resultaten der Modellrechnung einer 1-dimensionalen Staupunktströmung mit detailliertem Reaktionsmechanismus verglichen. Um die Modellrechnung zu überprüfen, werden auch gemessene Gasphasentemperaturen einer stöchiometrischen Staupunktflamme mittels OH-LIF

diskutiert. Es stellt sich heraus, dass mit der Vergrößerung des Massenflusses, sich der Flammenstabilisierungs-mechanismus ändert und mit ihm die Wärmestromdichte zunimmt. Damit sollte dieser Versuchsaufbau auch für weitere Untersuchungen der Flamme-Wand-Interaktionen geeignet sein.

Dedication

To

My parents

My Wife

and

My Children

Mohamed Salem Elmnefi

Acknowledgment

I would like to express my sincere gratitude and indebtedness to my supervisor, Professor. Dr. rer. nat. Burak Atakan , for his inspiration, guidance, encouragement and help which prodded me to complete this work.

While many other persons have contributed either directly or indirectly to this work, I would like to thank, Dr. Ulf Bergmann for his continued interest and support.

This work could not have been completed with out the incredible amount of cooperation and support, I received from my colleagues and friends and become my duty to acknowledge their contribution here.

Special thanks to all academic and technical staff of thermodynamics (institute for combustion and gas dynamics). I am so grateful to Dipl.-Ing. Andreas Görnt and Mr. Manfred Richter for their many helpful suggestions and technical support.

Special thanks are also due to my parents, my wife, and my lovely children from whom I always get support and lovely care.

Duisburg, 09.08.2010

Mohamed Salem Elmnefi

Contents

List of Figures

List of Tables

CHAPTER ONE

INTRODUCTION

1 Introduction

Combustion has always played an important role in the history of mankind: from prehistoric times when fire was used for cooking food and keeping wild animals at bay, to modern times in which combustion is an applied science that is important in transportation, power generation, industrial processes, and chemical engineering. Nowadays the combustion of fossil fuels provides more than 80% of the world's energy.

Combustion related research is driven mainly by three objectives: obtaining maximum efficiency, with an eye towards the limited supply of fossil fuels, minimizing pollution to preserve the environment, and achieving safe and stable operation for the end customer. The main challenge for combustion researchers, however, is to accomplish these goals simultaneously.

1.1 Flame impingement heating

Flame-impingement heating is often used for domestic purposes, e. g cooking as well as industrial applications to achieve intense heating. The combustion enthalpy release of gas flames is often transferred to surfaces as heat from direct impinging jets. The convective heat transfer rates are high in such process. Flame impingement heating is widely used in many industrial applications such as heating and melting of both glass and metal. For the production of synthetic diamond coatings by chemical vapor deposition, premixed impinging flame jets have been used as well (Cappelli, [1]). Stagnation flames are also being used to modify the surface properties of various materials. For example, premixed methane-air flames can beneficially alter the properties of polymer films [2]. In addition, some interesting new materials processing applications take advantage of flames that impinge on surfaces. For example, an atmospheric-pressure, high speed, premixed acetylene-hydrogen-oxygen flame that impinges on a 850°C deposition surface is found to grow high-quality polycrystalline diamond films [3, 4]. Other flame-diamond processes use a similar flow Configuration, but with low-pressure, burner-stabilized flames [5].

The heat transfer from such jets, which are in general at least two dimensional, is often described empirically in the vocabulary of non reacting heat transfer by some function of Nusselt number, Reynolds number and a dimensionless distance. The gas velocity relative to the flame speed is usually not considered to be an important parameter. This parameter can be investigated in detail in one dimensional stagnation point geometries, which can also be modeled easily in the laminar regime using elementary mechanisms. One dimensional flame impingement is so far mainly studied in relation to diamond CVD, while the heat transfer from such laminar flames was not in the center of interest.

For a single flame jet impinging on a flat surface many studies are available in the literature, most of them performed at relatively large distances between burner and surface and thus conducted at least two dimensional, many of them also being turbulent [6-11] A number of experimental, empirical, semi-analytical and numerical studies have been conducted. Excellent review papers [12-18] have been published highlighting different issues. Carefully controlled experiments are required to improve the understanding of convective and radiative heat transfer. All the authors mentioned in their review papers that flame impingement heat transfer needs further research because of its vast applications in industrial and domestic heating systems.

Very recently, (Remie et al.[19]) have presented analytical relations for the calculation of heat fluxes in the hot spot around the stagnation point for both two-dimensional and axisymmetric situations of laminar fuel-oxygen flames impinging on a flat plate. The analysis assumes that a plug flow is generated after the flame front and thus does not take into account flame stabilization. According to reference [20] this assumption, however, is not quite appropriate for fuel-air flames, because for these flames, the acceleration of the velocity component normal to the flame front after expansion, the gases flow sideways, causing a dip in the velocity field above the flame tip. The resulting flow of burnt gases, therefore, is not a perfect plug flow. In contrast, the burning velocity of a fuel–oxygen flame is very small compared to the unburnt gas velocity, the burnt gases only diverge sideways after the expansion. Therefore the dip in the velocity field above the flame tip is a lot smaller and the

resulting flow is closer to a perfect plug flow so, the theoretical and experimental results show good agreement.

Kleijn [21] carried out a numerical study of heat transfer from laminar, premixed methane/air flames impinging on a flat surface at relatively large distances between burner and plate, so that a two dimensional flow pattern arises. He presented streamlines and isotherms for various cases. He also presented a simple model for stagnation point heat flux in terms of a flame-tip-to-surface distance. However, detailed analysis of how the centerline velocity and temperature as well as the flame length get affected by the plate was not presented. In the combustion literature, there are also studies on the structure of a Bunsen flame (see e.g.[22]) which are related to this problem.

In combustion and related applications it is important for gaining a better understanding of heat transfer phenomena and helping to determine precisely the heat transfer from flames. This can be achieved, if the temperature measured accurately. As temperature is a fundamental thermodynamical parameter for describing physical, chemical and biological processes, much effort has been made to measure temperature precisely in a wide variety of applications, making temperature one of the most extensively measured parameters.

A variety of techniques are available enabling both invasive measurement, where the monitoring device is installed in the medium of interest, and noninvasive measurement where the monitoring system observes the medium of interest remotely [23]. One of the pioneers in combustion diagnostics is J. Wolfrum who used in his group a variety of optical methods for temperature and concentration measurements in combustion environments in the gas phase and on reacting surfaces (Wolfrum [24]; Kohse Höinghaus et al.[25]).

Surface temperature measurement is especially crucial for the determination of heat transfer from flames to solid walls. Often temperature is measured by using thermocouples or optical pyrometry. However, these techniques have their limits. Thermocouples need a very good thermal contact, which is difficult to achieve,

especially when the temperatures of moving parts (e.g. in machines) have to be measured. In these cases pyrometry would be an alternative, but the emissivity of the monitored surface has to be known, which again is difficult to achieve especially in processes where the emissivity varies with time.

Thermographic phosphors overcome these above mentioned drawbacks. Thermographic phosphors are rare earth-doped ceramics that fluoresce when exposed to light. The emission wavelength, intensity, and decay rate are all temperature dependent, so any of these properties can be measured to determine temperature. This method is good for surface temperature measurements and proven to be useful and accurate for a variety of thermal measurement applications [26-30].

OH laser induced fluorescence (LIF) is a commonly used method to determine the temperature in flames (see e.g Hartlieb et al. [31] ; Tian et al. [32]).with the advantage of a relatively simple experimental setup. OH is abundant in the hot zones of the stoichiometric flames investigated in this study, thus eliminating the need for seeding as would have been necessary for NO-LIF.

1.2 The objective of this thesis

The objective of this thesis was to design a new experimental setup using an optical method. This method use thermographic phosphors was capable to measure the steady state temperatures of (nearly) one-dimensional impinging premixed flames to solid walls. From the surface temperature also the local heat fluxes were determined. The one dimensional character of premixed stagnation flames presents a great advantage for numerical modeling and generally allows easier comparison between model and experiment. Moreover, the structure of these flames is representative for many practical flames.

In the first part of this work, the stagnation point heat flux measurements were made for one dimensional premixed laminar methane/air flame impinging on a flat surface. The Methane/air flames are studied at relatively small distances between burner and surface (H=15mm, 30 mm, and 60 mm) for different flow velocities.The investi-

gated flames were stoichiometric, lean and rich laminar methane/air flames. As methane is the major constituent of natural gas, the present research will be useful for understanding the stagnation point heat transfer for many industrial and domestic heating applications.

The hydrogen enrichment of hydrocarbon fuels is one strategy to reduce the emissions of carbon dioxide from combustion processes. The hydrogen could in principle come from regenerative energy sources, like solar thermal water splitting. However, the amount will probably not be sufficient to replace natural gas totally in the near future. Thus, mixtures of natural gas with hydrogen are of some interest. Most of the previous study for hydrogen/methane flames focused only on the effects of addition of hydrogen gas on turbulent flames characteristics and the laminar burning velocity [33-37].

However, the second part of this study was performed in order to get some understanding of the role of hydrogen addition to the methane gas on the heat transfer to walls. Stoichiometric premixed laminar hydrogen /methane/air flames impinging on a flat surface were studied at small distance between burner and plate (H=15 mm). Surface temperatures were measured using thermographic phosphors. The heat flux from the nearly one-dimensional flames was also determined. Mixtures of air with, 10, 25, 50 and 75 % hydrogen in methane (CH_4) (referred to as 10 % H_2, 25 % H_2, 50 % H_2, and 75 % hydrogen, respectively) for stoichiometric flames were investigated. The experimental results of both parts of the work were compared to modeling results using detailed chemistry. In order to validate the model, gas phase temperatures were measured by OH LIF for a stoichiometric stagnation point flame.

1.3 Outline of this thesis

The outline of the thesis will be as follows: Some fundamentals of combustion processes and aspects of physics and chemistry of laminar flames will be given in Chapter 2, and in Chapter 3 an overview of diagnostic techniques for temperature measurements with focus on the new phosphor thermometry technique will be given.

Chapter 4 provides the reader with a description of the experimental set up and experimental procedure for the work presented in the thesis. In chapter 5 a detailed error analysis of the experimental results will be presented. The results and discussion will be described in Chapter 6. Finally, in chapter 7 summary and conclusions are presented.

CHAPTER TWO

LAMINAR FLAME FUNDAMENTALS

2 Laminar flame fundamentals

A flame is a flow with a strong exothermic oxidation reaction, which is coupled with a strong temperature increase and a luminescent appearance [38]. A flame is a complex physical-chemical process consisting of a lot of sub processes like flow, diffusion and mixing, reaction kinetics, heat conduction and radiation, turbulence, phase change, and quenching effects. Considering the whole combustion process it can be divided into 4 sub processes:

- **Mixing** of fuel and oxidant; it must occur on a molecular level, to fulfill the initial conditions for reaction.

- **Heating** of the reactants to the ignition temperature; for reaction initiation the fuel and oxidant must have a minimum temperature to start the combustion reactions. The activation barrier of the initial reaction must be surmounted by addition of ignition source (spark, hot wire, auxiliary flame). In the present study the flames were ignited using ignition torch.

- **Combustion reaction** in the flame; here the formerly named reaction and exchange processes take place.

- **Heat loss** to recipient or environment; depends on the individual application. The character of the heat transfer affects the reaction and flow processes in the flame.

2.1 Flame Classification

Flames are often divided with respect to their premixedness and flow type [39]. Flames may be either stationary flames on a burner and propagating into a flow of gas from a burner tube, or they may be freely propagating flames traveling in an initially quiescent gas mixture [40]. Stationary flames are of two general types:

- Premixed flames where the fuel and the oxidizer are mixed before approaching the flame region. These flames can only be obtained if the initial fuel and oxidant mixture lies between certain composition limits called the flammability limits.

- Non premixed flames, also called diffusion flames where both mixing of the fuel and the oxidizer and the combustion occur at the interface. Both premixed and non premixed flames can further be classified as either laminar or turbulent depending on the regime of gas flow.

The two types of flames are also differentiated physically in that, for defined thermodynamic starting conditions, the premixed system has a defined equilibrium adiabatic flame temperature and for the idealized situation of planar flame in a one dimensional flow field, it has a defined adiabatic burning velocity or equivalent mass flux in a direction normal to its surface. An unstrained diffusion flame has no such simply defined parameters. The tasks of combustion flow diagnostics are to increase the fundamentals of combustion and to improve the performance of those engineering devices that utilize it.

Many practical combustion problems can be examined most conveniently under the well defined, controlled conditions which the laminar flame provides. In premixed flames, the laminar burning velocity and flame structure data can be extremely useful in the analysis of fundamental processes such as ignition, NO, and soot formation, and flame quenching. Also**,** turbulent flame models often prescribe the turbulent burning velocity as a function of laminar burning velocity. Thus**,** detailed information describing the dependence of the laminar burning velocity, flame thickness, ignition temperature, heat release rate and flame quenching on various system parameters can be a valuable diagnostic and design aid. Typical examples of laboratory flames are sketched on figure 2.1:

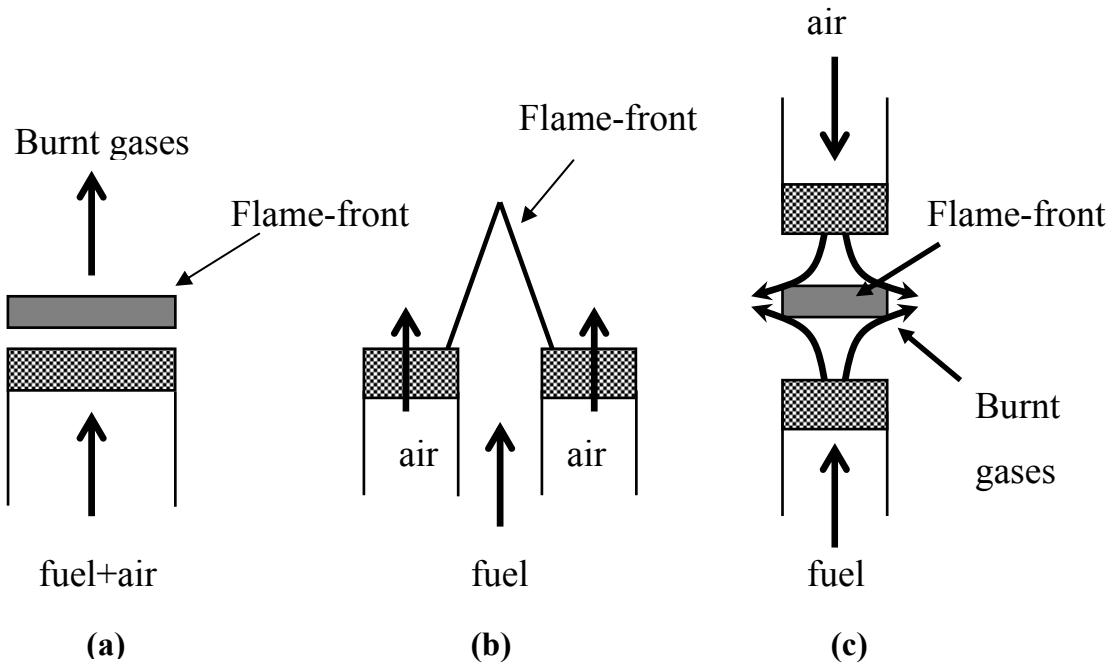

Figure 2-1 Schematic illustrations of laminar flames

The one dimensional flat premixed flame (Fig. 2.1a) is an example of a model flame system, which was used in this study for both methane/air and hydrogen/methane/air flames. It is also useful for understanding the primary flame front in most domestic gas appliances, and is also often studied to understand the microscopic structure of premixed turbulent flames in gas engines and low-NOx turbines.

Laminar non premixed flames are used as models to gain insight into the microscopic flame structure of turbulent non premixed flames in large boilers, industrial burners, power plants, etc. These flames are usually used in two geometries: coflow and counterflow. In the coflow geometry (Fig.2.1b), the convective fluxes of the fuel and the oxidizer are parallel to each other. In the counterflow geometry (Fig. 2.1c), the fuel and the oxidizer flow in opposite directions.

2.2 Combustion Terminology

In the following sub-sections, let us first consider some important terms, that are commonly used in flames and combustion analysis. These terms are very crucial to know, in order to understand flame combustion processes.

2.2.1 Stoichiometric Reaction

Stoichiometric reaction is one in which all of the oxygen atoms react chemically to appear in the products. This means that the amount of oxidant present in the reaction is just enough to completely burn the fuel to carbon dioxide and water. Air is the most common oxidizer. Assuming that air consists of 21% oxygen and 79% nitrogen by volume, the equation for a stoichiometric reaction of an air-methane mixture on a mole basis is:

$$CH_4 + 2(O_2 + 3.76N_2) \rightarrow CO_2 + 2H_2O + 7.52N_2 \qquad (2.1)$$

The minimum amount of air that is provided is just enough for complete combustion of the fuel is called the theoretical amount of air. If more air is provided, it is called excess air, and the extra oxygen and nitrogen will appear in the products in different proportions than before. Excess air is sometimes employed to ensure complete combustion or to reduce the product temperature. If less amount of air is provided, this is called excess fuel, and unburned fuel, soot, smoke, and carbon monoxide will produced.

2.2.2 Equivalence Ratio

The proportion with which the fuel and the oxidizer are mixed is commonly described by the equivalence ratio (φ). The equivalence ratio is one of the most important parameters for combustion analysis and is normally reported in terms of a non dimensional variable, which is the actual fuel/oxidant ratio normalized by the stoichiometric fuel/oxidant ratio, usually the oxidant amount varied and the fuel amount unchanged:

$$\varphi = \frac{(\text{Fuel}/\text{Oxidant})_{\text{actual}}}{(\text{Fuel}/\text{Oxidant})_{\text{stoich}}} \tag{2.2}$$

φ = 1.0 is defined as stoichiometric condition. Conditions where there is an excess of oxidant present in the mixture are "lean", φ < 1.0. Similarly, mixtures with an excess of fuel are "rich", φ > 1.0. Equation 2.2 is valid when the ratio is calculated on both mass and mole basis, provided that the actual and stoichiometric ratios are calculated consistently.

2.2.3 Flammability limits

Flammability limits bracket the rich-to-lean fuel-air mixture range beyond whic-h fuel-air can not bum after an ignition source is removed, even if the mixture is at its ignition temperature. For the stoichiometric case, if an ignition source is introduced into the mixture even at a very low temperature and at reasonable pressures (e.g., 1 atm), the gases about the ignition source reach a sufficient temperature so that the local mixture moves into the explosive region and a flame propagates. This flame, of course, continues to propagate even after the ignition source is removed. There are mixture ratios, however, that will not self-support the flame after the ignition source is removed. These mixture ratios fall at the lean and rich end of the concentration spectrum. The leanest and richest concentrations that will just self-support a flame are called the lean and rich flammability limits, respectively.

2.2.4 Flame Temperature

Another important combustion parameter is the flame temperature. The flame temperature T_f is determined by the energy balance between the reactants and the products at equilibrium. If the reaction zone is spatially very thin in comparison to the rest of the domain of interest, then it is a common practice to denote the maximum temperature in the reaction zone to be the flame temperature. If the combustion process takes place adiabatically, and with no work, or changes in the kinetic or

potential energy, then the flame temperature is referred to as the adiabatic flame temperature T_{af}. This is the maximum temperature that can be achieved for the given reactants because any heat transfer from the reaction zone and any incomplete combustion would tend to lower the temperature of the products. Experimental measurements of T_{af} are very difficult and in most cases a calculated value is more reliable than the experimental measurements [41]. According to laminar flame theory, T_f has a substantial effect on the flame speed.

2.2.5 Flame Speed

The flame speed is defined as the local velocity of the reactant mixture normal to the reaction zone, just as the gases move into the reaction zone. It is widely perceived that T_f essentially determines the flame speed and significantly influences the formations of the products of combustion. A primary objective of premixed laminar flame theory involves the determination of the laminar burning velocity, S_L. Different theories with varying assumptions are presented [42], that result in expressions for S_L that are functions of various transport properties. In 1883, Mallard and Le Chatelier proposed a simple theory which predicted that the laminar flame speed, S_L is related to the overall reaction rate and the thermal diffusivity [43]. Mallard and Le Chatelier divided the flame into two zones; the preheat zone in which the gases are heated by conduction and reach ignition at ignition boundary and the second zone, in which chemical enthalpy is converted into sensible enthalpy. The energy balance of the preheat zone gives:

$$\dot{m}C_p\left(T_i - T_0\right) = k\frac{T_f - T_i}{\delta} \tag{2.3}$$

where k is the thermal conductivity, Cp is the specific heat and δ is the thickness of the reaction zone. The subscripts f, 0 and i stands for flame, unburned and ignition. The mass flow rate per unit area, $\dot{m}$ is defined as:

$$\dot{m} = \rho_u S_L \tag{2.4}$$

where ρ_u is the density of unburned gas and S_L is the laminar flame speed.

From equations (2.3) and (2.4), the burning velocity is given by:

$$S_L = \left(\frac{k(T_f - T_i)}{\rho_u c_p (T_i - T_0)} \frac{1}{\delta} \right) \tag{2.5}$$

If τ_r is the reaction time, then

$$\delta = S_L \tau_r = S_L \frac{1}{d\varepsilon/dt} \tag{2.6}$$

where $d\varepsilon/dt$ is the rate of reaction (RR) and ε is the reaction-progress variable then:

$$\delta \alpha \; S_L \frac{1}{RR} \tag{2.7}$$

Substituting equation (2.6) in equation (2.5) will give:

$$S_L = \left(\left(\frac{k}{\rho_u C_p} \right) \frac{T_f - T_i}{T_i - T_0} \left(\frac{d\varepsilon}{dt} \right) \right)^{0.5} \propto (\alpha.RR)^{0.5} \tag{2.8}$$

In the above equation the reaction rate RR was not specified by Mallard and Le Chatelier at any particular temperature. However, their analysis suggests that the flame speed is proportional to the square root of the product of thermal diffusivity and reaction rate. This result is one of the most important relationships in laminar flames theories. As stated previously, the flame speed is essentially determined by the value of T_f. Therefore, the variation of the flame speed S_L at adiabatic conditions due to changes in φ is primarily determined by the variation of adiabatic flame temperature

T_{af} (Kuo [42] and Williams [44]) discuss several methods which are currently used to experimentally determine S_L.

2.2.6 Flashback and Blow off

In premixed flames, there are situations when the supply velocity of the reactant, just prior to the flame front is not sufficient to oppose the flame speed. Under such conditions, the flame propagates upstream into the incoming reactants. This is known as flashback. On the other extreme, there are conditions where the local supply velocity of the reactant is greater than the flame speed. Under such situations the flame moves downstream, a phenomenon termed as blow off. If the supply velocity of the reactant is equal to the flame speed, the flame will keep its position relative to the burner surface and known as burner stabilized flame.

2.3 Flat laminar premixed flames

Flat laminar premixed flames are the workhorse of many combustion laboratories, since the one-dimensional character of these steady flames offers great advantages for modeling, and allow a straightforward comparison with experiments. In a flat laminar premixed flame, fuel and oxidizer (for example methane and air) are fully mixed prior to combustion. The premixed gas composition, as stated previously in equation (2.2), is usually expressed in terms of the equivalence ratio (φ), which is defined as the molar ratio of fuel and oxidizer with respect to that at stoichiometric conditions. A premixed flame is considered stoichiometric if oxidizer and fuel are in the ratio prescribed by the balanced chemical equation for combustion, for example:

$$CH_4 + 2O_2 \rightarrow CO_2 + H_2O \tag{2.9}$$

The coupling of heat and mass transport and chemical reaction leads to a spatial structure, the flame, which determines the path from reactants to products. Figure 2.2 shows schematically the structure of a flat laminar-premixed flame.

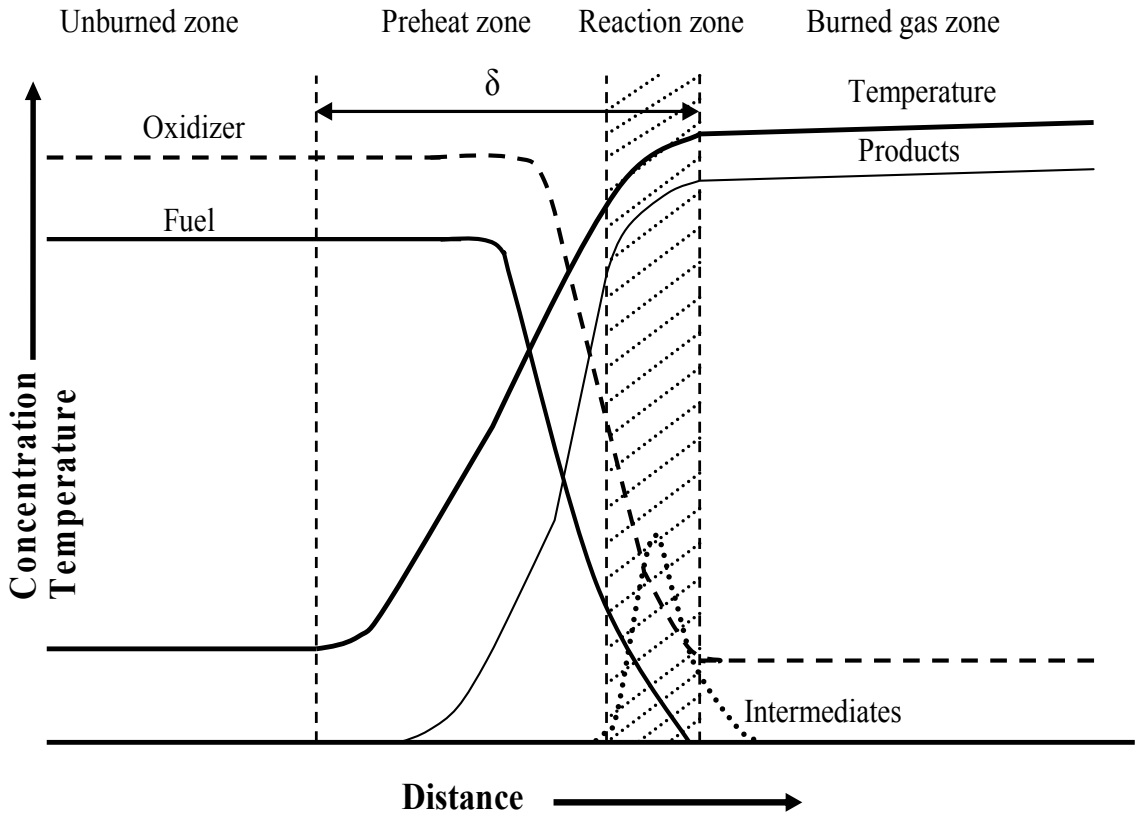

Figure 2-2 Schematic representation of premixed flame structure

Premixed flame structure can be divided into four zones: unburned zone, preheat zone, reaction zone and burned gas zone [45]. The unburned mixture of fuel and oxidizer is delivered to the preheat zone at ambient conditions, where the mixture is warmed by upstream heat transfer from the reaction zone. In the reaction zone, the fuel is rapidly consumed and the bulk of chemical energy is released. The thickness of the flame front (δ, see Figure 2.2) is ~ 0.5 mm at atmospheric pressure and ~ 5 mm at 25 Torr and depends not only on pressure but also on initial temperature and equivalence ratio [46, 47].

This thin flame front implies steep gradients of species and temperature, which provide the driving forces for the flame to be self-sustaining (i.e the flame continues to propagate even after the ignition source is removed). In the reaction zone, temperature is high enough for creating a large radical pool. Finally, in the burned

zone, radicals recombine, and both temperature and major species concentrations approach their equilibrium values. However, the concentrations of minor species in this region can deviate substantially from their equilibrium values.

In the laboratory frame, where the unburned fuel/oxidizer mixture propagates with velocity V, the speed of the flame front V_{fr} is ($V-S_L$). In practice, one-dimensional flames are created by supplying the fuel/oxidizer mixture through the porous material, effectively creating a uniform flow field, which is schematically illustrated in Figure 2.3.

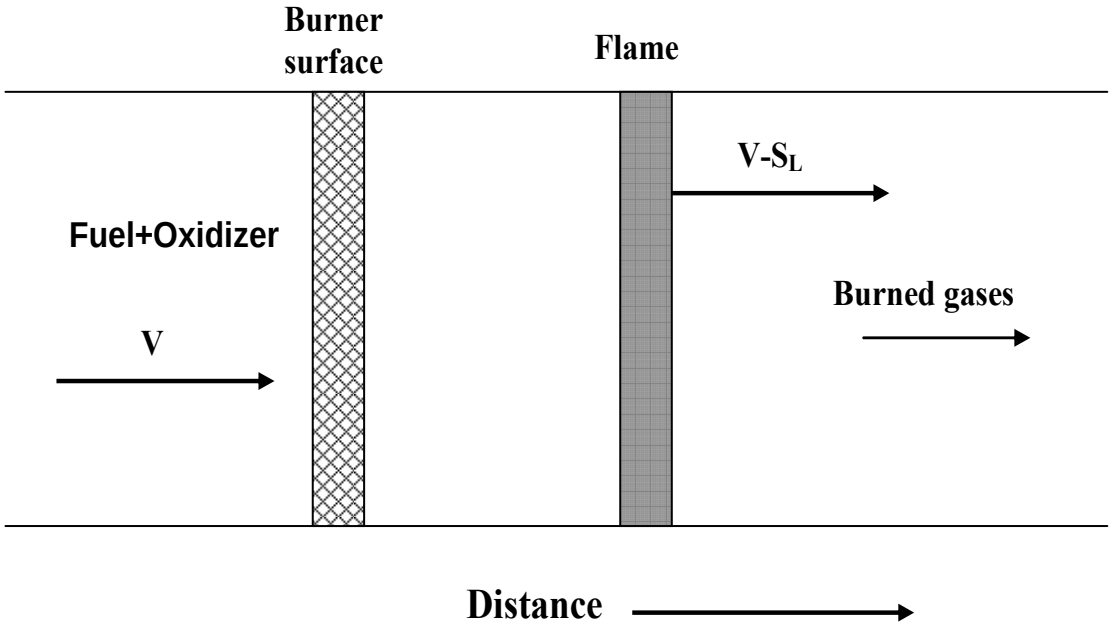

Figure 2-3 Schematic illustration of flame burning downstream of a matrix Burner, where V is unburned gas velocity, S_L is laminar burning velocity

Since the laboratory frame is attached to the burner, three possible situations may occur, depending on the relation between V and S_L. First, if $V>S_L$ the flame will move away from the burner, i.e., the flame will blow off. If $V=S_L$, the flame will keep its position relative to the burner surface, and be aerodynamically stabilized. In this case, neglecting possible radiative losses from the flame to the surroundings, the

enthalpy in the fuel is solely manifest in the temperature of the burned gases, and the flame is referred to as an adiabatic or free flame. The temperature corresponding to an adiabatic flame is the maximum flame temperature that can be achieved for a given fuel oxidizer composition. If $V<S_L$, the flame will become unstable and move towards the burner and will attempt to enter the burner and this situation is un safe and should be prevent to occurs in real operation. Since the pores of the idealized burner are assumed to prevent the flame from entering the burner, the flame will transfer heat to the burner to lower the actual burning velocity to the flow velocity; in this condition the flame is referred to be as being stabilized by the burner surface.

2.3.1 Conservation equations for a one-dimensional laminar flame

In a one-dimensional steady flame at constant pressure, the effects of viscosity, radiation and gravitation are generally neglected [47, 48]. In this case, the governing equations can be written as shown below [48].

Overall conservation of mass

The conservation of total mass states:

$$\frac{d(\rho v)}{dx} = \frac{dM}{dx} = 0 \tag{2.10}$$

where v is the mass averaged flow velocity, x is the distance along the stream line to the stagnation point normal to the burner surface and M is called the mass flux. From equation (2.10) follows that the product of the density and the velocity, the mass flux, is constant and independent of x.

Conservation of mass of a particular species *i*

$$\frac{d}{dx}\left[y_i \rho (v + V_i)\right] = R_i \qquad (i = 1.....K) \tag{2.11}$$

where y_i is the species mass fraction and V_i is the species diffusion velocity, expressing the molecular transport caused by concentration gradients of species i. When the concentration of i^{th} component is low, Fick's law [47] can be used to calculate V_i. An important property is that the system of equations (2.10) and (2.11), contains K linearly independent equations. Because the chemical reaction does not change the elemental composition, the total mass production rate $\Sigma R_i = 0$.Therefore, summation of equation (2.11) over K yields equation (2.10).

In flames, the time scales of transport processes, such as diffusion and heat conduction are comparable to the time scales of chemical reactions. Therefore, determining combustion properties requires information on the rates of both transport processes and chemical reactions.

Equation of state

The equation of state for compressible flow is given by:

$$P = RT\sum_i \frac{y_i \rho}{M_i} \tag{2.12}$$

where P is the pressure, R the universal gas constant, T the temperature and M_i the molar mass of species *i* . Assuming that the dependence of the diffusion velocity V_i on the temperature and species concentrations is known, the above described system consists of (K+1) linearly independent equations and contains (K+2) unknown parameters: y_i,ν, ρ and T. Thus, the system contains more unknown parameters than equations and a solution is only possible if one of the parameters is specified, or if an extra equation is added to the system, such as the equation for the conservation of energy.

Conservation of energy

The conservation of energy for stagnation point along stream line is expressed as:

$$\frac{d}{dx}\left[\sum_i y_i \rho H_i (\nu + V_i) - \lambda \frac{dT}{dx}\right] = 0 \tag{2.13}$$

where, H_i is the specific enthalpy of the i^{th} species and λ the thermal conductivity of the mixture. The conservation of energy states that the sum of energy transport by means of convection (first term), diffusion (second term) and conduction (third term) must be equal to zero. With proper choice of the boundary conditions for one-dimensional flame its, possible to solve the governing equations [47].

2.3.2 Chemical kinetics

The equation of conservation of species (2.11) includes the net rate of change of species due to chemical reactions. The quantity R_i expresses the time derivatives of the concentration of some species *i* involved in the reaction. Consider the chemical reaction of the general type:

$$aA + bB + cC + ... \underset{k_r}{\overset{k_f}{\Leftrightarrow}} dD + eE + fF + ..., \tag{2.14}$$

where A, B, C, … represent the different species involved in the reaction, a, b, c, denote the numbers of moles of species A, B, C,…, k_f and k_r are rates constant of forward and reverse reactions. Then, the law of change rate of species A for an elementary reaction is written as follows,

$$K_A = \frac{dA}{dt} = -k_f N_A^a N_B^b N_C^c ..... + k_r N_D^d N_E^e N_F^f ..... \tag{2.15}$$

In equilibrium, the net rate of change of species A should be zero, therefore

$$\frac{N_D^d N_E^e N_F^f}{N_A^a N_B^b N_C^c} = \frac{k_f}{k_r} = K_{eq}, \tag{2.16}$$

where K_{eq} is the equilibrium constant, which can be found from thermodynamics [48] and N the molar number density. Thus the rate of change of A species is expressed through the following equation,

$$k_A = \left(N_A^a N_B^b N_C^c .... - \frac{N_D^d N_E^e N_F^f}{K_{eq}} \right), \tag{2.17}$$

The rate constant is often a strong nonlinear function of temperature and usually expressed most simply in the Arrhenius law form as:

$$k = A \ \exp\left(-\frac{E_a}{RT} \right) \tag{2.18}$$

where

A = pre-exponential factor

E_a = Activation energy of the reaction

R = ideal gas constant

T = Temperature

The modified Arrhenius equation [49], in which the pre-exponential factor is proportional to T^n where T is the temperature and n a constant is expressed as:

$$k = BT^n \exp\left(-\frac{E_a}{RT} \right) \tag{2.19}$$

B is a temperature-independent constant.

2.4 Impinging flame jets

The flow field in impinging jets can be divided into three characteristic regimes [15] (Figure 2.4): the free jet region, the stagnation region and the wall jet region. The stagnation region is characterized by pressure gradients, which stop the flow in the axial direction and turn it radially outward. The static pressure distribution around the impingement surface is also used to determine the extent of the stagnation region. This region is defined as the region where the static pressure (P_{st}) exceeds the distant ambient pressure. The boundary of the stagnation region, parallel to the wall, defines the start of the so called wall jet region. This is a boundary layer flow.

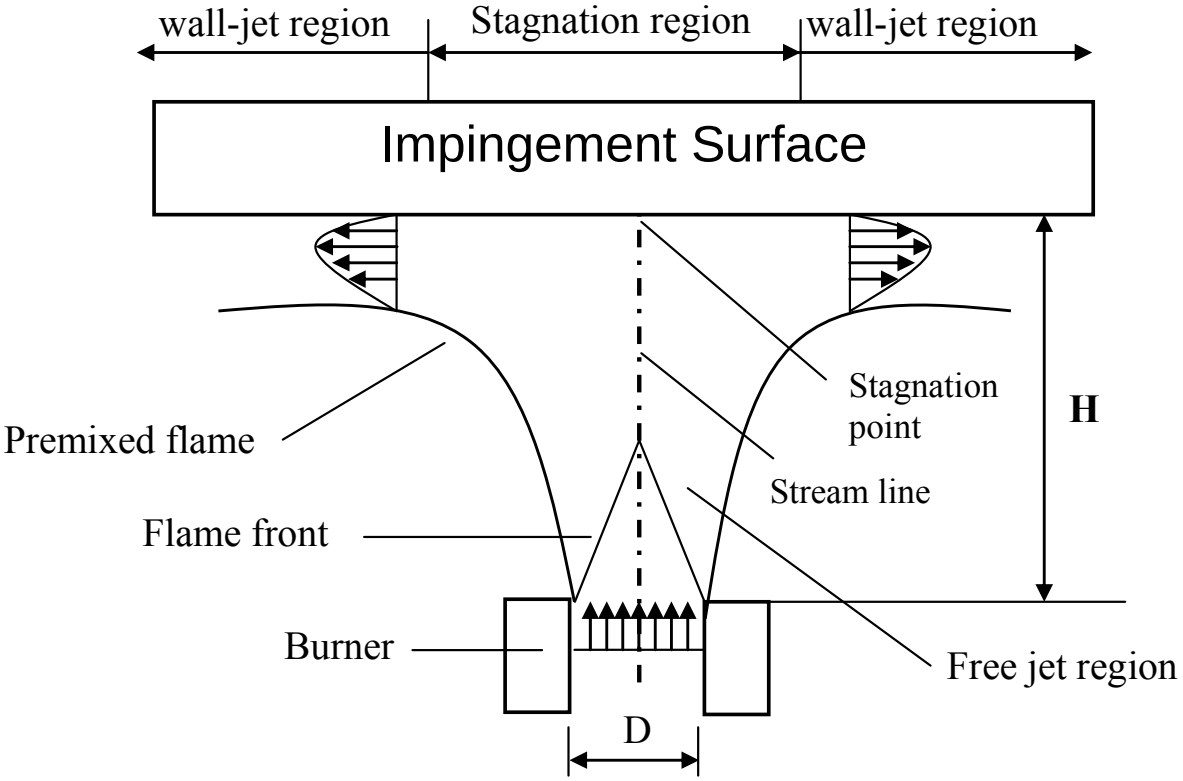

Figure 2-4 Schematic overview of a stagnation flame impinging on a plane surface

The wall jet region is free gradients of mean pressure. The flow decelerates and spreads here. The flow issuing from the nozzle is either laminar or turbulent, depending on the nozzle type and the Reynolds number (Re). The flames used in the current study are laminar and look like the above flame structure. Figure 2.5 show a

flame photo of the methane laminar flame impinging on the water cooled plate of the current experimental study. According to (Viskanta [13]), the aerodynamics of the single flame jet is similar to those of the isothermal jet. The pressure and axial velocity profiles of the flame jet are very similar to those of the isothermal jet [6].

Figure 2-5 Photograph of the investigated laminar methane flame impinging on water-cooled plate (φ =1 and v= 1 m/s)

The experimental results of (Van der Meer [50]) also reveal this similarity but show that the flame jet axial velocity decays slightly faster than in the isothermal jet. The primary difference between the flame jet and the isothermal jet is the presence of the reaction zone in the free jet and possibly in the stagnation and the wall jet regions along with the temperature gradient in the flame jet.

Flat flames can be made to impinge onto surfaces. Such “strained” flames can be used for a variety of purposes. On the one hand, these flames can be used in the laboratory to study the effects of strain on flame structure, and thus improve understanding of the fluid mechanical effects encountered in turbulent flows. It may also be interesting to discover how a cool surface (e.g., an engine or furnace wall)

affects flame structure. Even though the stagnation-flow situation is two-dimensional in the sense that there are two velocity components, the problem can be reduced to a one-dimensional model by "similarity," This is just the behavior that is required to realize the stagnation-flow similarity, on which the one-dimensional models are based. This is also valid for 2-D similarity model.

In the following subsections several heat-transfer mechanisms will be discussed more extensively. Let us first consider some non dimensional numbers that are commonly used in heat transfer analysis:

The Reynolds number:

The Reynolds number (Re) determines the ratio of the inertial forces to the viscous forces in a flow:

$$\mathrm{Re} = \frac{\rho U L}{\mu} = \frac{U L}{\nu} \tag{2.20}$$

where ρ the fluid density [kg/m^3], U the fluid velocity [m/s], L the characteristic length scale (e.g., diameter for a pipe for flow through a pipe and for one dimensional stagnation flame the distance between the burner surface and the stagnation surface can be considered as the characteristic length[51]), μ the dynamic viscosity [kg/(m· s)] and ν the kinematic viscosity [m^2/s].

The Reynolds number is low for laminar flows and high for turbulent flows, with transition flow at values in between. Up to a Reynolds number of Re = 2300, an impinging jet is considered to be laminar [52]. In the current study values of Reynolds numbers for various cold gas velocities were calculated using the axial distance between the burner surface and the stagnation point along the stream line, which are all confirms laminar flow.

The Prandtl number:

The ratio of momentum diffusivity to thermal diffusivity is expressed by the Prandtl number (Pr):

$$\mathrm{Pr} = \frac{\nu}{\alpha} \tag{2.21}$$

where $\alpha = k / (\rho \cdot c_p)$ is the thermal diffusivity [m^2/s], with k the thermal conductivity [W/(m·K)] and c_p the specific heat at constant pressure [J/(kg·K)]. For many gases, the Prandtl number is typically equal to Pr = 0.7.

The Nusselt number:

The Nusselt number (Nu) is defined as the ratio of the convective to the conductive heat transfer rates:

$$\mathrm{Nu} = \frac{hL}{k} \tag{2.22}$$

where h is the heat-transfer coefficient [$W/(m^2 \cdot K)$]. The Nusselt number is typically a function of Re and Pr for forced convection flows and is used to determine the convective heat-transfer rate. The stagnation point heat flux can be correlated in terms of a relationship between the Reynolds number and the Nusselt number. As mentioned previously the heat flux is determined from Fourier's law by evaluating the temperature gradient at the surface:

$$q = -k\frac{dT}{dx} = -k\frac{\Delta T}{L}\frac{d\hat{T}}{d\hat{x}} \tag{2.23}$$

where $\hat{T}$ and $\hat{x}$ are the non dimensional variables of the temperature and position.The heat flux can also represented in terms of a heat transfer coefficient in form of Newton's law of cooling as:

$$q = h\Delta T \tag{2.24}$$

Combining these provides a relationship for the Nusselt number, which is a non dimensional heat-transfer coefficient:

$$Nu = \frac{hL}{K} = -\frac{d\hat{T}}{d\hat{x}} \tag{2.25}$$

Once the system of equations has been solved, the nondimensional temperature gradient can be easily evaluated at the surface, providing the Nusselt number. It should be expected that the heat transfer depends on the boundary-layer thickness, which in turn depends on the flow field, which is principally governed by the Reynolds number. For Reynolds number greater than about 5, the Nusselt-number correlation depends on the square root of the Reynolds number [51]:

$$Nu = \frac{hL}{k} = 0.67\sqrt{Re} = 0.67\sqrt{\frac{UL}{\nu}} \tag{2.26}$$

The Lewis number:

The Lewis number (Le) defines the ratio of the heat diffusion to the species diffusion:

$$Le = \frac{k}{\rho cpD} \tag{2.27}$$

with D the species diffusivity coefficient [m^2/s].

The Eckert number:

The Eckert (E_c) expresses the relationship between a flow's kinetic energy and enthalpy, and is used to characterize dissipation:

$$E_c = \frac{V^2}{cp\Delta T} \tag{2.28}$$

where V is a characteristic velocity of the flow, c_p is the constant-pressure specific heat of the flow, and ΔT is a characteristic temperature difference of the flow.

2.5 Heat Transfer Mechanisms

Six heat transfer mechanisms have been identified in previous flame impingement studies: convection (forced and natural), conduction (steady-state and transient), radiation (surface, luminous, and nonluminous), thermochemical heat release(TCHR) (equilibrium, catalytic, and mixed), water vapor condensation, and boiling (internal and external) [53, 54]. All of the mechanisms are not usually present simultaneously and depend on the specific problem. Figure 2.6 shows schematically the heat transfer mechanisms for a water-cooled target.

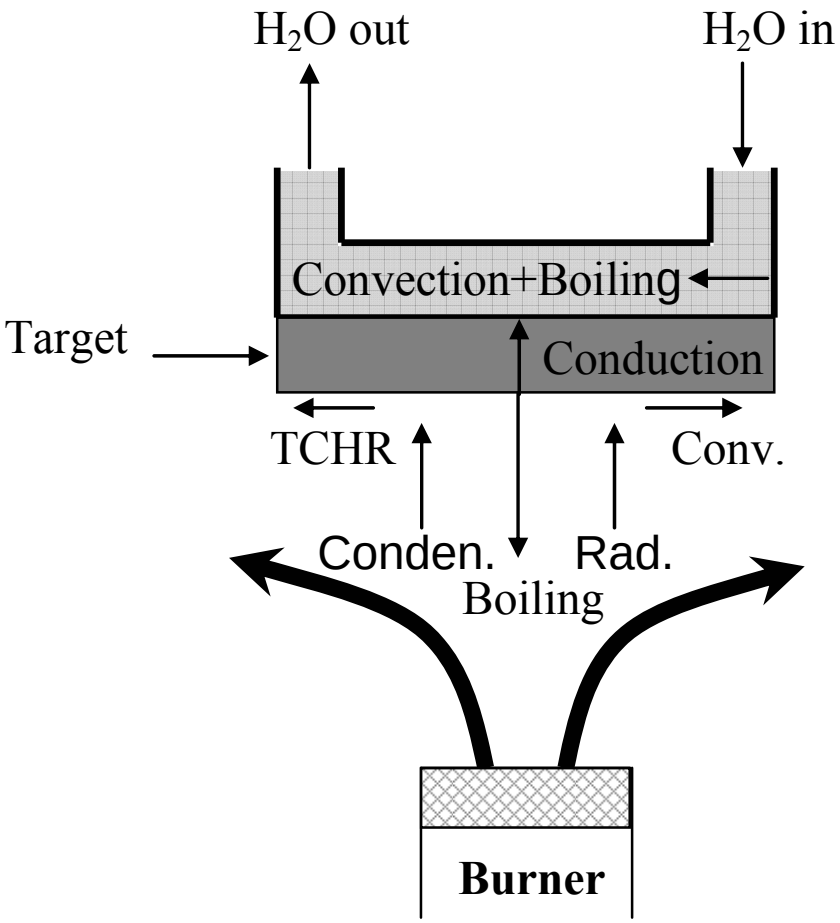

Figure 2-6 Heat transfer mechanisms in flame impingement on a water-cooled target

Originally, heat-transfer relations applicable for impinging flame jets were taken from aerospace technology. Heat-transfer correlations concerning flame jet impingement show a lot of resemblances with aerospace applications [55]. High temperatures at the stagnation point of aerospace vehicles are produced as these vehicles travel through the atmosphere. Therefore, very high heat fluxes arise in that region.

In the aerospace applications, the vehicle moves through the atmosphere where the gases are relatively stagnant. In the case of impinging flame jets, the burnt gases move around a stationary target. Therefore, the relative motion is similar in both cases and the solutions found for the heat transfer in aerospace situations are used for flame-impingement heating studies as well. In the following subsections we will discuss some of the heat transfer mechanisms more extensively. More detailed information on the other mechanisms are available in reference [54].

2.5.1 Conduction

Thermal conduction has played an important role in many flame impingement heating applications. In some processes, high thermal conduction rates are desired. An example is a rapid reheat furnace. There, the goal is to raise the temperature of metal parts. Because metals generally have high thermal conductivities, heat can be quickly conducted through the part. This reduces the temperature gradient between the surface and the interior of the part. High gradients may cause the part to warp or deform. In other applications, low thermal conduction is desired.

In the current study, the conduction heat flux in flame impingement was determined. The heat flux for one dimensional steady flow was determined from Fourier's law of conduction by evaluating the surface temperatures on both sides of the coated ceramic plate. With known values of thermal conductivity of the used alumina plate, K (in current study the average values of the thermal conductivity of both side of the plate were taken) and also the known thickness of the plate (6 mm), the local heat flux $\dot{q}$ in the center of the plate, which is equal to the amount of heat

transfer by convection from the flame to the plate under steady flow condition and given by:

$$\dot{q} = \frac{\dot{Q}}{A} = -k\frac{\Delta T}{L} \tag{2.29}$$

$\dot{q}$ =Heat flux (kW/m²)

k =Thermal conductivity (kW/m·K)

ΔT =Temperature difference across the plate (K)

L =Thickness of the plate (m)

A = area (m²)

$\dot{Q}$ = heat flow rate (kW)

2.5.2 Convection

Convective heat transfer is depending on several factors like the fluid dynamics of the jet, the turbulence intensity, the separation distance between burner and target surface, the shape of the target, the fuel-oxidizer combination, the stoichiometry, recombination of radicals at the target and whether the jet is a premixed or diffusion flame [13]. The effect of the equivalence ratio was studied by Hargrave et al. [56]. The results show that variations in equivalence ratio away from approximately stoichiometric conditions lead to a shifting of the flame reaction zone downstream and to a decrease in the maximum rate of heat transfer from the flame.

Experimental results [56] show that the equivalence ratio also affects the local heat-flux distribution, since it effects the entire combustion process. Rigby and Webb [7] found that the heat flux to a disk is relatively constant for natural gas-air diffusion flames for larger nozzle-to-plate spacing. Mizuno [57] experimentally found that the heat flux increases with decreasing separation distance for premixed methane-air flames. This result was explained by the fact that the smaller separation distance allowed less entrainment of cold ambient air into the flame, resulting in a higher burnt gas temperature and thus a higher heat flux.

In many conventional furnace heating processes, forced convection is only a small fraction of the total heat transfer to the product. Most of the heating emanates from the radiation from the hot refractory walls. However, in flame impingement, with no furnace enclosure, forced convection may be 70% − 90% [57, 58]. For flames with temperatures up to about 1700 K, forced convection is the dominant mechanism in flame impingement heat transfer [59]. Burner exit velocities typically are high enough, so buoyancy effects can be neglected. For air/fuel flames combustion systems, forced convection has generally been the only mechanism considered. In highly dissociated oxygen/fuel flames, a large fraction of the heat release is from exothermic reactions, which is known as thermochemical heat release, which will explained in details the following subsection. However, even for those flames, forced convection is still an important contributor to the overall heat transfer to the target.

2.5.3 Thermochemical Heat Release

Flame jets can be operated with an increase of the amount of oxygen in the oxidizer stream, which leads to a higher burning velocity of the flame [60]. Therefore, the flame jet can be operated with higher gas velocities. For instance, stoichiometric methane-air flames have a temperature of about 2200 K, while stoichiometric methane oxygen flames reach temperatures of about 3000 K. The higher unburnt gas velocity as well as the increased flame temperature cause the effect that higher heat-transfer rates are obtained.

As mentioned previously, the products of many combustion processes contain dissociated species. The degree of dissociation increases as the flame temperature increases. Since oxygen enriched flames reach high temperatures, their products contain a lot of free radicals due to dissociation. As the gases cool down due to impingement near the cold surface, they exothermically recombine to more stable products. The radical recombination causes an additional heat release. This mechanism is called Thermochemical Heat Release (TCHR). TCHR can be of the same order of magnitude as forced convection at high temperatures. Two chemical mechanisms are identified which initiate Thermochemical Heat Release, namely equilibrium TCHR and catalytic TCHR [61]. If the chemical reaction time scale is

smaller than the diffusion time scale, equilibrium TCHR comes into play. The chemical reactions take place in the boundary layer. In the case of catalytic TCHR, that is if the radicals have insufficient time to react before they reach the surface, recombination may take place at the surface. In other word, equilibrium TCHR occurs in the gas phase between the burner and the target, outside the boundary layer, which has been greatly exaggerated. CO combines with radicals to produce CO_2. Catalytic TCHR occurs when the gases contact the surface, which catalytically promotes the reaction of CO to CO_2 in the presence of radical species. Mixed TCHR is a combination of equilibrium and catalytic TCHR.

2.5.4 Radiation

The influence of radiation on the heating process is highly dependent on whether the target is isolated or placed in an enclosure [62, 63]. Two components contribute to the thermal radiation heat transfer at the target surface, if the target is isolated: nonluminous radiation and luminous radiation. The luminous flame contains particles that glow and radiate heat to the target. In contrast, the nonluminous flame contains no radiating particles, so that only gaseous radiation from CO_2 and H_2O are commonly present. In the presence of a confinement such as a furnace, surface radiation will contribute a significant part of the total heat flux.

Nonluminous radiation is occurs by gaseous combustion products such as carbon dioxide and water vapor. The amount of radiation produced by the gases depends on the gas temperature, partial pressures of the emitting species, concentration of each emitting species and the optical path length through the gas. Although some studies indicate that nonluminous radiation amounts to a significant part of the total heat flux to the target [7, 64] , most studies consider radiative heat transfer in nonluminous flames negligible , since it is present very small amount comparing to the total heat flux [13, 16, 21, 59, 65].

If a flame produces a lot of soot, luminous radiation can be a significant component of the radiation heat transfer. The soot particles will radiate approximately as a black body. This mechanism is especially important when solid and liquid fuels are

used. It is not commonly significant if gaseous fuels are combusted, except when the flames are very fuel rich or if diffusion flames are applied, which have a tendency to produce soot. Surface radiation contributes significantly to the total heat transfer if the target is heated inside an oven or furnace. Beer and Chigier [58] examined the radiation contribution to the total heat transfer for a stoichiometric air-coke oven gas flames impinging on the hearth of a furnace. The measured radiation was at least 10% of the total heat flux. Ivernel and Vernotte [64] calculated that radiation from furnace walls accounted for up to 42% of the total heat flux. From these results it is clear that radiation from the surrounding surfaces becomes very important in high-temperature furnaces.

CHAPTER THREE

THERMOGRAPHIC PHOSPHORS

3 Thermographic Phosphors (TPs)

3.1 TPs and other temperature measurement techniques

Temperature is both a thermodynamic property and a fundamental parameter for describing physical, chemical and biological processes. Its measurement is critical to many aspects of human activity from the thermodynamic improvement of heat engines to process control and health applications. Surface temperature measurement is especially crucial for the determination of heat transfer from flames to solid walls. Much effort has been made to measure temperature precisely in a wide variety of applications, making temperature one of the most extensively measured parameters [23].

The range of techniques and devices available for surface temperature measurement is extensive. Options include invasive or contact methods such as thermocouples and resistance thermometers to non-invasive techniques using, for example, infrared detectors. In addition, recent developments in optical methods and micro manufacturing have resulted in the wider spread availability and use of advanced techniques such as coherent anti-Stokes Raman scattering [66] and thin film transducers for temperature measurement [67, 68].

The requirements for a temperature measurement may allow direct contact with the medium. Alternatively this may not be possible or desirable and a noninvasive method may be used. Temperature cannot be measured directly. Instead the effects on some other physical phenomena must be observed and related to temperature. There are many physical phenomena that are dependent on temperature such as resistance, volumetric expansion, vapour pressure and spectral characteristics. Many such phenomena have been exploited to produce devices to measure temperature.

Temperature measurement techniques can be classified according to the nature of contact between the medium of interest and the device. The categories used here are invasive, semi-invasive and non-invasive:

- Invasive techniques are those where the measuring device is in direct contact with the medium of interest. An example is a liquid in glass thermometer immersed in a liquid or a thermocouple inserted in a gas stream.

- Semi-invasive techniques are those where the medium of interest is treated in some way to enable remote observation. An example is the use of thermo-chromic liquid crystals, which change color with temperature. A surface can be sprayed with these and then observed remotely with, say, a CCD (charged coupled device) camera, which improves resolution compared with older technologies. A CCD is a light-sensitive integrated circuit that stores and displays the data for an image in such a way that each pixel (picture element) in the image is converted into an electrical charge the intensity of which is related to a color in the color spectrum.

- Non-invasive techniques are those where the medium of interest is observed remotely. An example is the use of infrared thermometry where the sensor is located some distance away from the target material.

However, these techniques have their limits. Thermocouples need a very good thermal contact, which is difficult to achieve, especially when the temperatures of moving parts (e.g. in machines) have to be measured. In these cases pyrometry would be an alternative, but the emissivity of the monitored surface has to be known, which again is difficult to achieve especially in processes where the emissivity varies with time.

In recent years a new technique has been developed for remote measurements of surface temperature using thermographic phosphors. This technique overcome some these above mentioned drawbacks as will be discussed in the following chapter, so that it is a good method for surface temperature measurements. It is used in scientific and industrial applications of surface thermometry to complicated geometries , e.g., rotor engines, turbines engines [69], and also in medicine. During the last years , as

the applications of thermographic phosphors have expanded, some attempts have been made in combustion environment [70]. In addition, this method proven to be useful and accurate for a variety of thermal measurement applications [26-30, 71].

3.2 Thermographic phosphors principles

Phosphors are materials doped with trace elements that emit light when suitably exited by an energy source such as, an electron beam, x-ray source, or ultraviolet light (UV). There are a wide variety of ceramic phosphors that survive harsh physical and chemical environments, are insoluble in water, durable, and easy to apply. Phosphors can be used for a wide range of temperatures from cryogenic levels up to 2000°C [23]. There are two classes of phosphors: organic and inorganic. It is the inorganic types such as Al_2O_3: Cr^{3+}, Al_2O_3:Tm^{3+}, Al_2O_3:Dy^{3+} and TiO_2:Eu^{3+}, whose properties, such as phosphorescence decay time, intensity and spectral distribution, following an excitation with an light source are temperature dependent and tend to be used in thermometric applications [72-77].

The basic principle of thermographic phosphors is well established. Luminescence refers to the absorption of energy by material , with the subsequent emission of light. Fluorescence refers to the same process as luminescence, but with the qualification that the emission is usually in the visible band and has a duration of typically 10^{-9}-10^{-3} s. Phosphorescence is a type of luminescence of greater duration, $\approx 10^{-3}$-10^{3} s [26].

Phosphor thermometry takes advantage of the thermal dependence of the phosphorescence properties, such as intensity, line-width, line position, and decay rate. Usually phosphorescence decay time, also known as lifetime, is the parameter that is measured to determine the temperature. This technique offers high sensitivities and accuracies (Allison and Gillies [26]). This technique was used in different combustion environments (e.g. see [78, 79]).

The molecule which was in an excited state will return to the ground state, emitting the absorbed energy via a number of processes. The main mechanisms by which deexcitation can occur can be categorised into non-radiative and radiative decay processes [80]. These processes are illustrated schematically using a Jablonski diagram (Figure 3.1) [81], which illustrates the energy levels for a typical photoluminescent molecule.

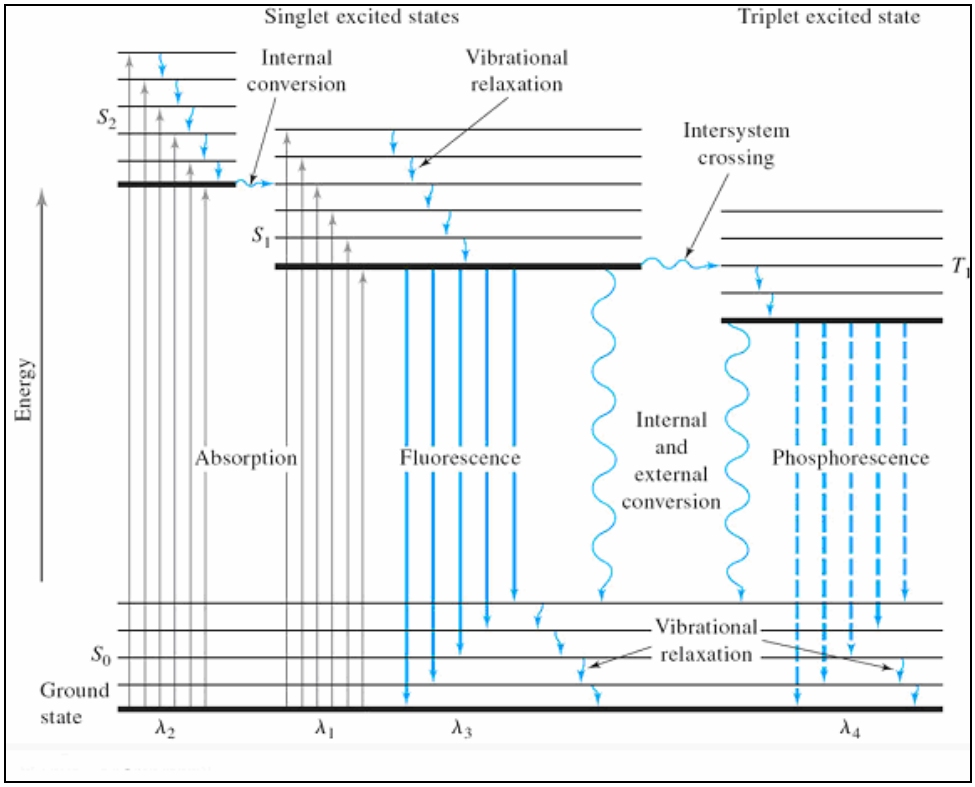

Figure 3-1 A Jablonski diagram or partial energy level diagram for a photoluminescent system showing pathways for the deactivation of an excited state**.**The lowest vibrational energy level for each electronic state is indicated by the thicker line.

If a molecule initially occupies the lowest vibrational energy level of its electronic ground state in a singlet state labeled S_o and then absorbs a photon of the correct energy, it can be excited to one of several vibrational energy levels in the first excited state, S_1, or to higher electronically excited singlet states (e.g. S_2). Relaxation to the ground state can occur by a number of mechanisms that are either radiationless in that

no photons are emitted or involve the emission of a photon. In Figure 3.1, the straight vertical arrows represent fluorescence and phosphorescence, which involve the release of a photon of energy. The other deactivation steps as indicated by "wavy" arrows represent the radiationless processes, which compete with fluorescence. If deactivation by fluorescence is rapid with respect to the radiationless processes, then such emission will have a high probability and intense fluorescence will be observed.

When incident photons excite a phosphor, it begins to reemit at a specific wavelength determined by its electronic band structure. Many factors contribute to the intensity of the phosphor emission, such as material properties, doping, temperature, and excitation source. The measured emission intensity I is proportional to the rate of change of excited luminescence centers n* (Shionoya and Yen [82]), such that:

$$I \propto \frac{dn^*}{dt} \tag{3.1}$$

The number of luminescence centers (electron/hole pairs available for recombination) is governed by the radiative and non-radiative recombination of electrons with holes as:

$$\frac{dn^*}{dt} = -(W_R - W_{NR})n^* \tag{3.2}$$

where W_R and W_{NR} are the radiative and non-radiative transition probabilities respectively, and the negative sign indicates emission. The transition rates are usually treated as a single term, known as the overall lifetime, τ, such that:

$$\tau^{-1} = W_R + W_{NR} \tag{3.3}$$

In general, this lifetime is temperature dependent. When the excitation source is removed, the number of excited electrons n is governed by the differential equation:

$$\tau(T)\frac{dn}{dt} + n = 0 \tag{3.4}$$

where τ (T) is the electron lifetime, which is a function of temperature. Assuming the electron lifetime is constant during the decay, the solution to equation 3.4 is given as:

$$\frac{n}{n_0} = \exp\left(-\frac{t}{\tau}\right) \tag{3.5}$$

where n_0 is the number of electrons at t = 0. By differentiating equation 3.5 and recalling equation 3.1, the intensity can be expressed in terms of the decay time as :

$$\frac{I}{I_0} = \exp\left(-\frac{t}{\tau}\right) \tag{3.6}$$

where:

I = the intensity of the decaying phosphorescence signal at time t

I_0 = Initial phosphorescence signal intensity at t = 0

τ = Phosphorescence decay time

The above equation is used to describe phosphor emission intensity decay in non-contact thermometry. If the temperature is constant, then the decay time, which is a function of temperature, also remains constant. In this case, the emission intensity of a phosphor at a given temperature is recorded, and the decay time is extracted from the emission data. This decay time is specific to a certain temperature.

In this study the chromium–doped aluminum oxide (ruby) is used for the surface temperature measurements. The phosphorescence of ruby is quite strong and can be excited in the green and in the blue spectral range. It is stable at high temperatures , and its luminescent properties are well known and have almost completely analyzed. The phosphorescence is emitted in the red spectral range. It shows two phosphore-scence transitions at 694.3 nm and 692.9 nm (so-called R-lines), and the decay time of

the phosphorescence is relatively long, around 3 ms at room temperature and decreasing at higher temperature. Figure 4.3 shows the measured phosphorescence lifetime for ruby as a function of temperature.

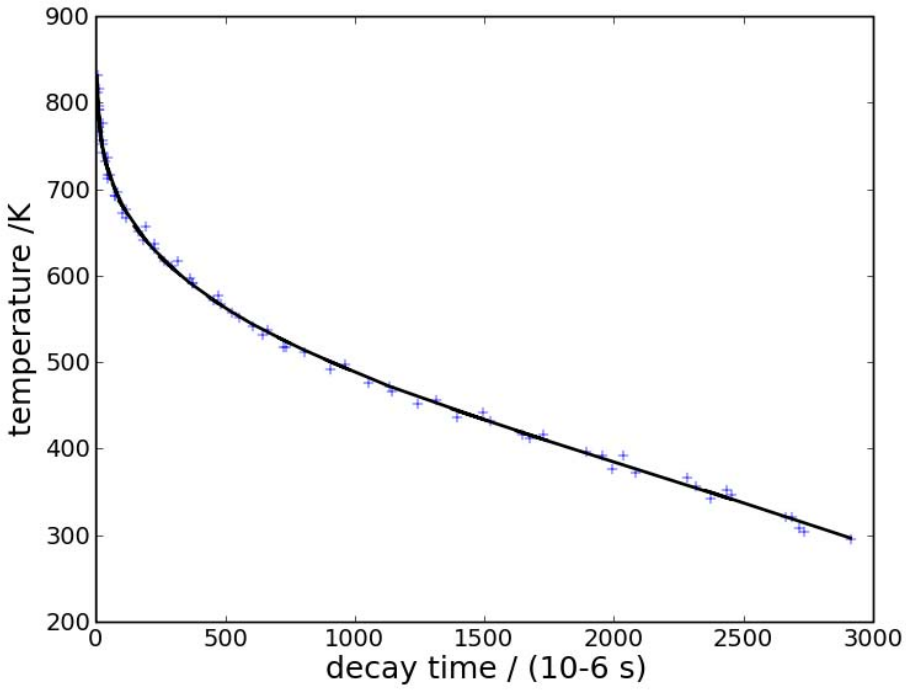

Figure 3-2 Life time decay of Cr:Al_2O_3 at different temperatures

CHAPTER FOUR

EXPERIMENTAL

4 Experimental

4.1 Experimental setup

The experiment was designed in such a way that a one-dimensional stagnation point geometry is approximated. Figure 4.1 shows schematically the first designed experimental setup. The experimental setup consists of two main structural components: the burner for heat generation and the heat receiver for the heat absorption system. In this experiment a moveable sintered bronzed type (SIKA-B 20) burner of 30 mm diameter with porosity of 38 % surrounded by water cooling jaket was used. A one side coated silicon wafer of 100 mm diameter and 0.5 mm thickness was attached to the impingement surface, it was evenly cooled on the reverse side by a cooling water jacket, there was no soot deposition on the surface. Figure 4.2 shows a photograph of the first experimental setup.

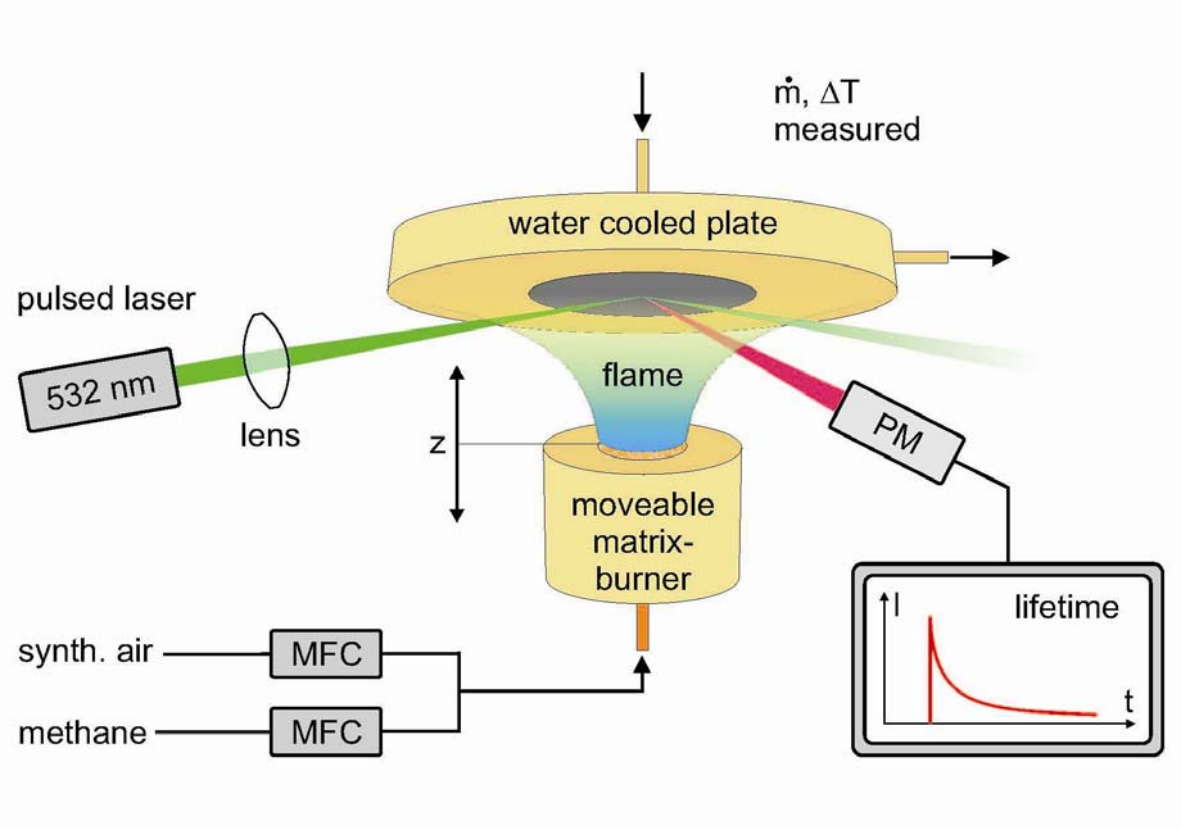

Figure 4-1 The First experimental set up

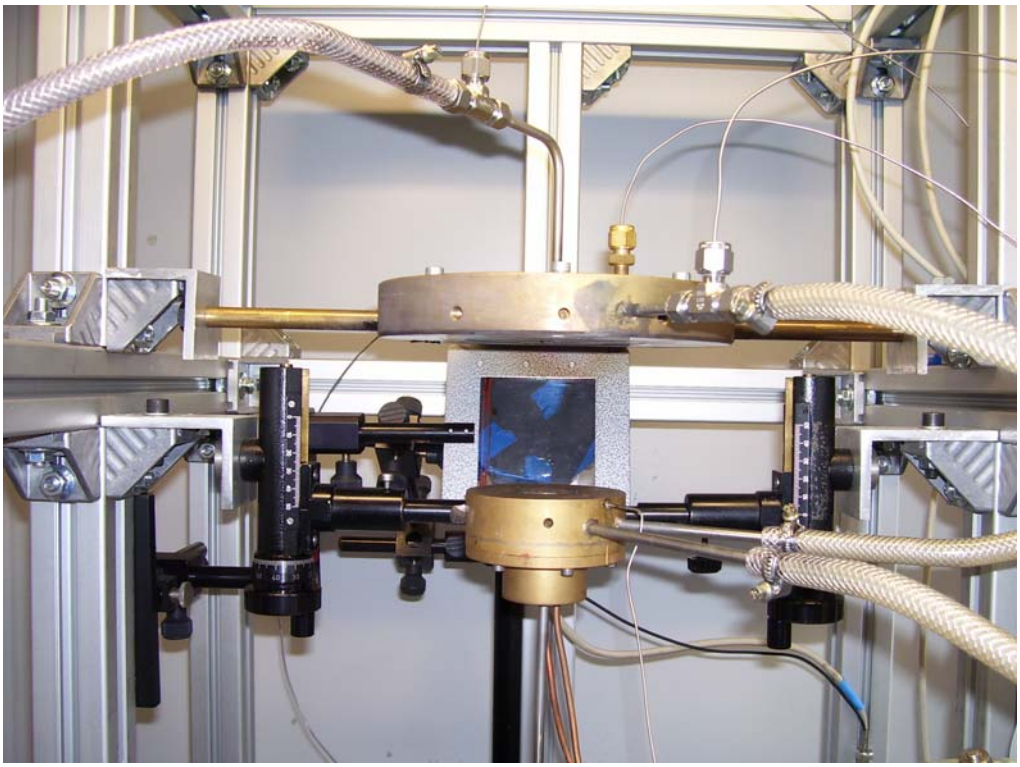

Figure 4-2 The first experimental setup (only surface temperature on the flame side measured using thermographic phosphors)

The above experimental setup can measure the surface temperatures using thermographic phosphors only on the plate flame side, while the heat flow rate obtained from the energy balance would have to be divided by an area, to obtain the heat flux rate. However, the size of the area can be chosen in different ways, so that the results would become ambiguous.

In order to overcome the above mentioned problem a new experimental setup was designed. The new flame impingement setup was designed in such a way, that the surface temperatures on the both sides of ceramic plate can be measured using thermographic phosphors and the one dimensional stagnation point geometry is approached. .Figure 4.2 shows schematically the new experimental setup. The new setup is much better suited to obtain the local heat flux rate than measuring the energy balance of the cooling water, since contributions of larger radial distances do not disturb the present measurements.

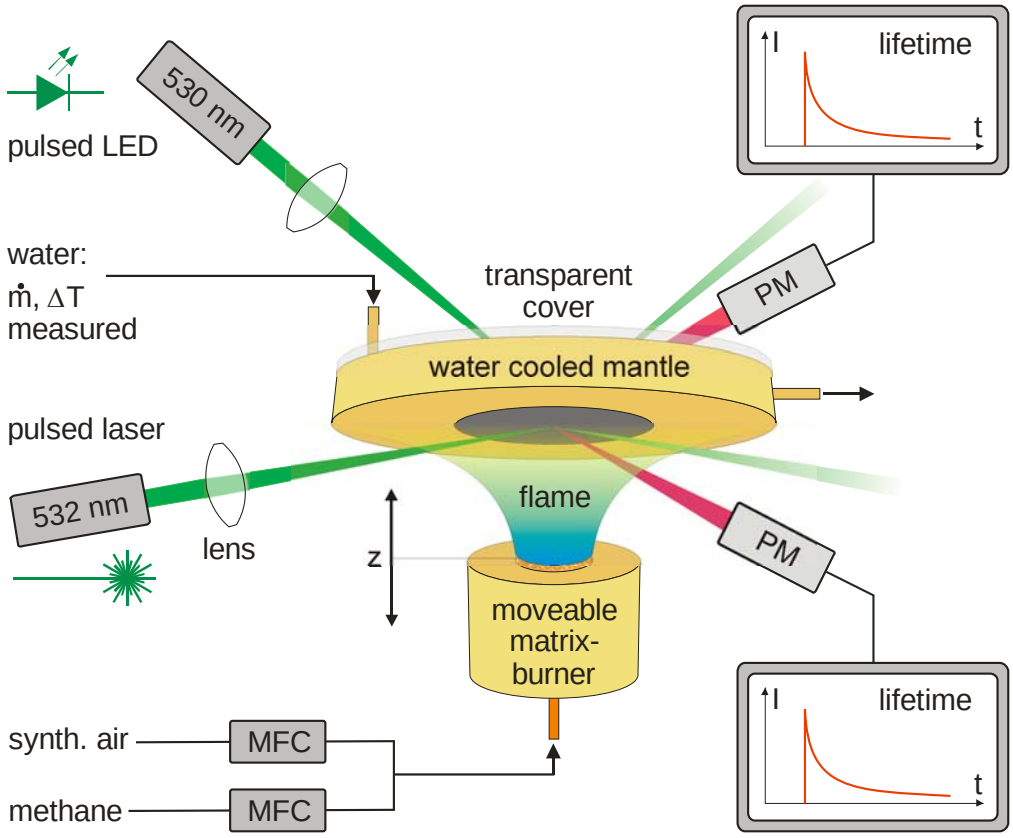

Figure 4-3 The new experimental setup (surface temperature on both sides measured using thermographic phosphors)

The new experimental setup consists of two main structural components: the burner for heat generation and the heat receiver for heat absorption. The heat receiver is made of a hollow water streamed disc of 30 mm thickness and 200 mm outer diameter. It has a brass ring as a frame for the ceramic plate on the flame side, and a transparent acrylic glass cover on the top. The acrylic glass allows for a good transparency in the range of the phosphorescence and excitation wave lengths and is stable in the temperature range of interest (below 120˚C on the pressurized water-cooled side). In addition, the flow of the cooling water can be easily visualized. The temperature of the heated side of the plate was kept relatively low (T< 500 K) because the backside of the ceramic plate was in direct contact with the pressurized cooling water (ca. 3 bar). The ceramic plate is made of aluminium oxide (Al_2O_3) of 6 mm

thickness and 80 mm diameter and was coated on both sides with ruby as a phosphor. Figure 4.4 shows the photograph of the new experimental setups.

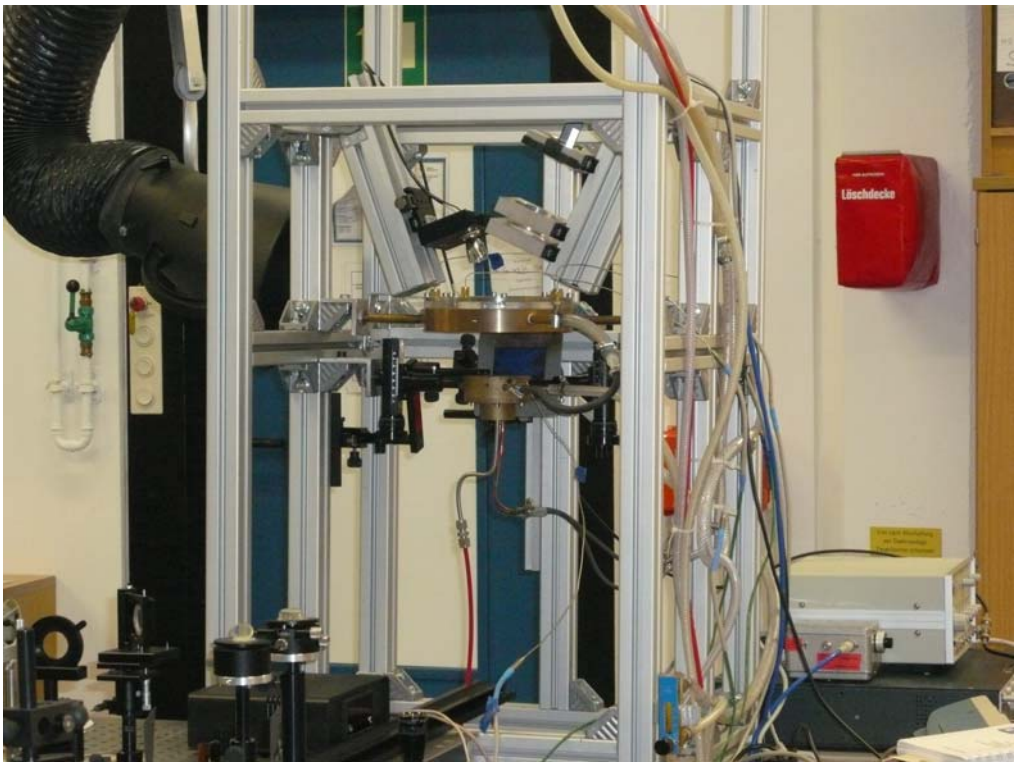

Figure 4-4 The new experimental setup (temperature measured on both sides of the coated ceramic plate using thermographic phosphors)

In order to obtain a laminar one dimensional flame for different fuel air mixture velocities, two different burner types were used: a matrix flat burner surrounded by a water-cooled jacket was used for lower fuel air mixture velocities (0.1 m/s to 0.5 m/s). At higher flow rates the flames show cellular structures on the matrix burner, so simple one-dimensional flow is only observed at low flow rates. For high flow rates, a nozzle burner is more suitable, which was used for a higher fuel air velocities (0.7 m/s to 1.2); however, at lower velocities it is not appropriate, since the flame will stabilize inside the tube. Both burners providing nearly 1D flames at the center as can also be seen from Figures (4.3 and 4.4). This is also deduced from two dimensional OH-LIF images as measured by S. Staude (Salem et al. [83]), at least for the interesting central part of the flame.

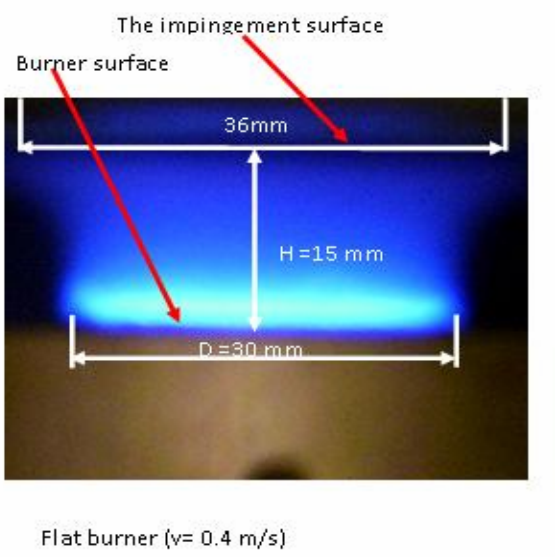

Figure 4-5 Photograph of flat burner flame with dimensions

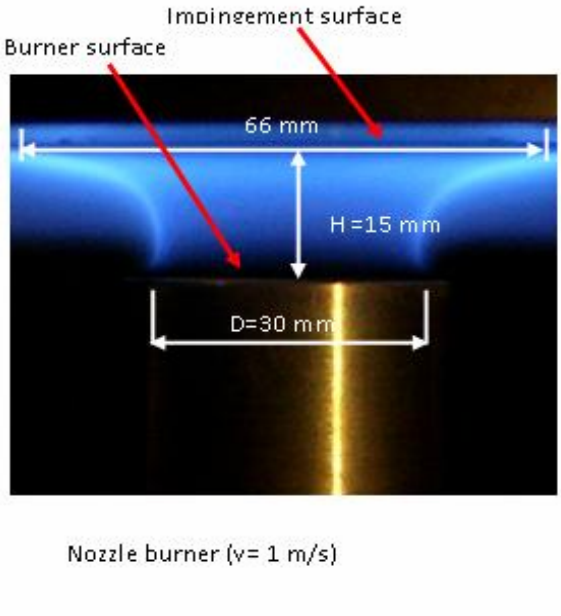

Figure 4-6 Photograph of nozzle burner flame with dimensions

For the temperature measurement on the flame side, the plate was irradiated with the 2nd harmonic of a pulsed Nd: YAG Laser (532 nm). The laser beam was aligned to the centre of the plate and has a beam diameter of about 3 mm on the coated ceramic plate. The cooled side phosphor coating was excited with a green LED

array (Opto Technologies Inc., OTLH-0020-GN) with a peak wave length at 525 nm, emitting a typical power of 2.4 W. Two photomultiplier (PM) tubes (Hamamatsu H6780-03) were used to receive the phosphorescence signal from both sides of the plate. The signal was recorded by a digital oscilloscope (Tektronix TDS 2024) and then transferred to a PC after typically averaging for 128 pulses.

A fast pulse generator (Toellner, TOE7404) was used to provide the input for the green LED. Inlet and outlet temperatures of the cooling water, upper surface temperature of the ceramic plate (i.e. on the cooling water side), and the flat burner surface temperature were measured with platinum resistance thermometers (PT100) and thermocouples (K-type), respectively. Initially, it was intended to measure the upper surface temperature independently with the thermocouple and to compare the results with the thermographic phosphor measurement; however, it was found that the contact resistance was too high for reliable results. All the mentioned temperatures were measured and recorded using a LABVIEW program. The flow of the cooling water was kept constant (20 L/h) for all experiments. Methane with 99.99% purity was used and burnt with synthetic air (volume %: 21% O_2 and 79% N_2) provided from (air-liquid). Three mass flow controllers (MKS instruments) with volume of 100, 10, 5 litters were used to control the flows of air, methane and hydrogen respectively.

In addition, the surface temperatures on both sides of the ceramic plate were measured by using green LEDs. The experimental setup was not changed, only the phosphor on the flame side was excited with a green LED instead of laser. Another fast pulse generator (Toellner, TOE7404) was used to provide the input for the second LED. The experimental measurements were carried out for lower fuel mixture velocities (0.05-0.5 m/s) for stoichiometric methane/air flame and hydrogen/methane/air flames with 10%, and 20% of hydrogen gas at the smallest distance between the burner and the plate (15 mm). Figure shows the experimental setup for the surface temperatures measurement using green LED on both sides of the plate for phosphor excitation.

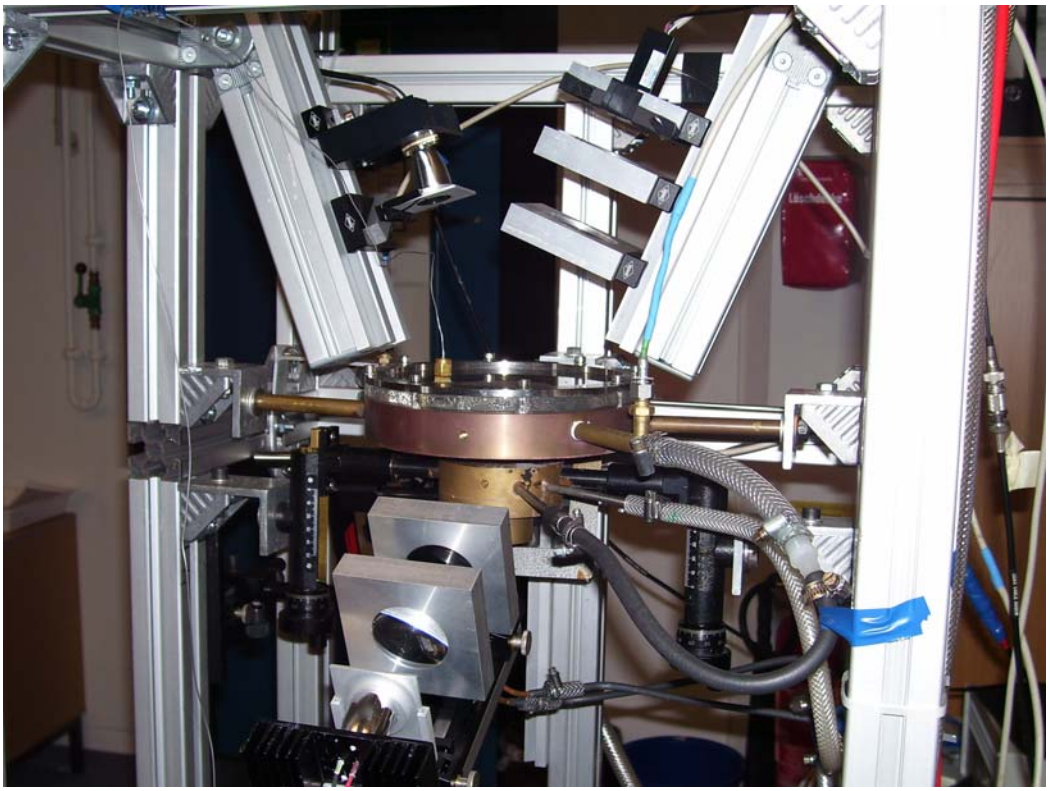

Figure 4-7 New experimental setup (LED excitation on both sides of the plate)

4.1.1 Coating the Ceramic plate surfaces using Sol-gel method

In the present study, a flat alumina ceramic of 6 mm thickness and 80 mm diameter plate acting as the stagnation surface was coated on both sides with a well established phosphor, chromium doped aluminum oxide Al_2O_3:Cr (ruby) (chromium concentration = 1.1%). The coating was produced by the sol-gel method, which is relatively simple to apply [84]. In the sol-gel process a system of colloidal particles in a solution (sol) becomes a macroscopic material (gel), which is interpenetrated by a liquid. Once the liquid evaporates, a strong layer of the coated material remains. The un-doped aluminum oxide was stable at high temperature and chemically rather inert, which makes it suitable to be used.

The preparation procedure for such ruby coating using the sol-gel method is rather simple as no complicated set-up is needed; the ceramic plate just wet with a liquid sol at room temperature, subsequently heated in air at 563 K while forming an

amorphous aluminum film. The coated plate was finally annealed in a tube furnace (Carbolite) at 1403 K for two hours in order to obtain the stable α-phase of aluminum oxide. The sol-gel process was repeated several times in order to obtain a homogenous stable film. The sol with 1.1% Cr (Cr-to-Al-ratios), was prepared from aluminum tri-isopropoxide (ATI), chromium acetyl- acetonate ($Cr(acac)_3$, diethylene glycol monoethylether ($C_6H_{24}O_3$), and acetic acid (CH_3COOH). Figure 4.8 shows the Flowchart of sol-gel processes.

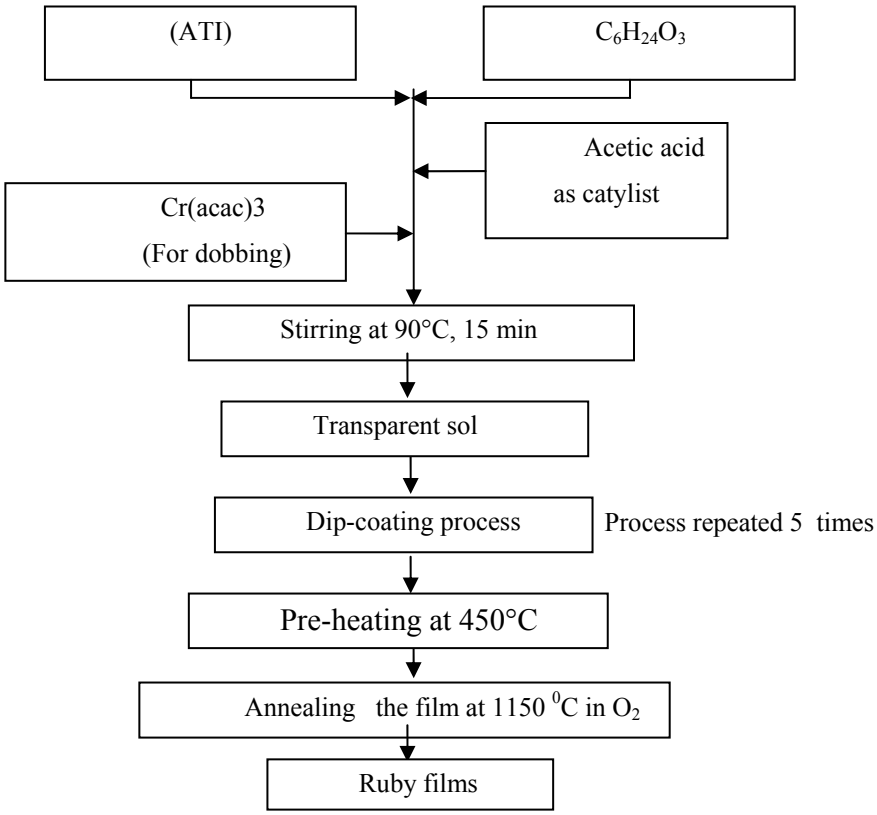

Figure 4-8 Flowchart showing the procedure for preparing Cr^{+3}:Al_2O_3 (ruby) films on ceramic plate (Al_2O_3)

The structure of the coated ceramic plate was analyzed using X-ray diffraction (XRD). Figure 4.6 shows the patterns for the coated plate, which indicate the α-phase of alumina (α-Al_2O_3).

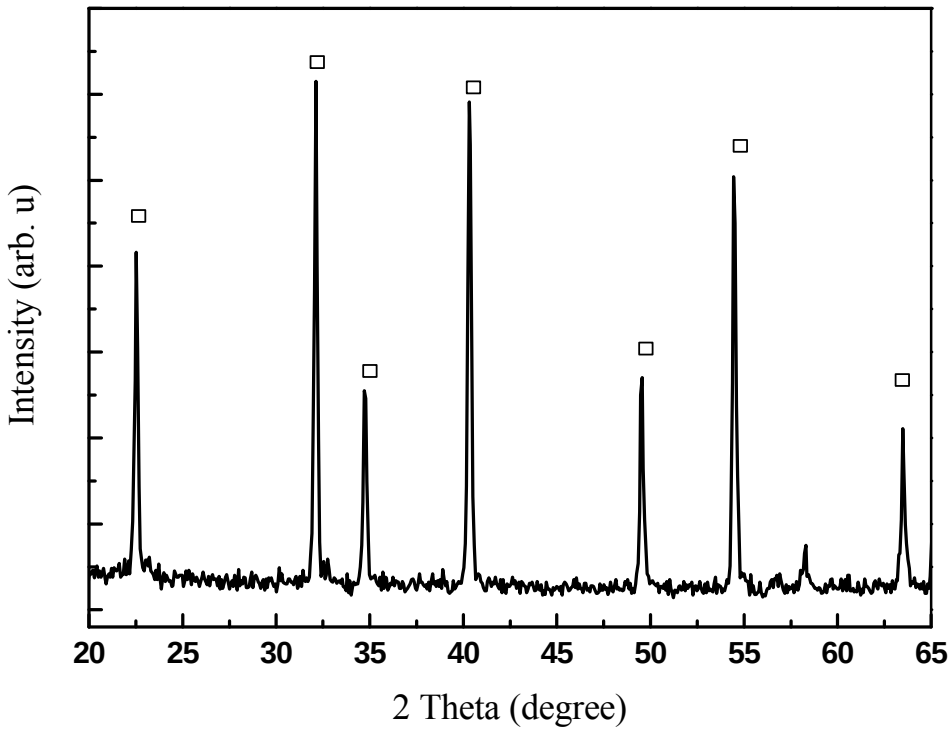

Figure 4-9 XRD patterns Cr^{+3}-doped aluminum oxide film on Al_2O_3 plate;
α-Al_2O_3 reflection (□)

4.1.2 Calibration of thermographic phosphors

For calibration, the Ceramic plate was placed inside a tube furnace (Carbolite), where it was heated gradually and its surface temperatures were measured using a thermocouple in direct contact with plate surface while the phosphorescence from the front side of the plate was detected. The phosphorescence was exited with a green light emitting diode (LED) emitting at 525 nm at about 30 different temperatures in the range of 295-600K. For each measurement, the emission signal of the phosphorescence was recorded and the decay time was evaluated. The ceramic plate side which was used for the surface temperature measurement on the flame side was calibrated, and the phosphorescence was exited with Nd:YAG laser emitting at 532 nm.

The temperature-dependence of the phosphorescence lifetime was determined for both sides of the ceramic plate. Pure ruby has a mono-exponential decay [84] but the plate itself also showed some temperature dependent phosphorescence, so that slight deviations from a mono exponential decay were observed; an algorithm by (Brübach [85]) was used to handle this situation. This algorithm can reduce the multi exponential decay curves to give the lifetime by fitting an analytical waveform to the measured decay curve. Hence a mono-exponential approach is followed in which the fitting window has to be the same for all the measurements. In this algorithm the curve is reduced to a single lifetime by applying an iteratively defined fitting window which depends on the decay characteristics.

In order to validate the calibration data, they were fitted to Seat-Sharp Model [86], which shows a good agreement. This model is relatively accurate for ruby lifetime decay from 300 to 800 K. With proper choice of fit parameters this model can give a very accurate prediction of temperature dependent fluorescence lifetime. The obtained fitted parameters were later used to determine the surface temperature on both sides of the plate. Figure 4.8 shows the calibration curve, where the phosphorescence lifetime was measured as a function of temperature to be ranging from 2.85 ms at 295 K to 0.310 ms at 573 K.

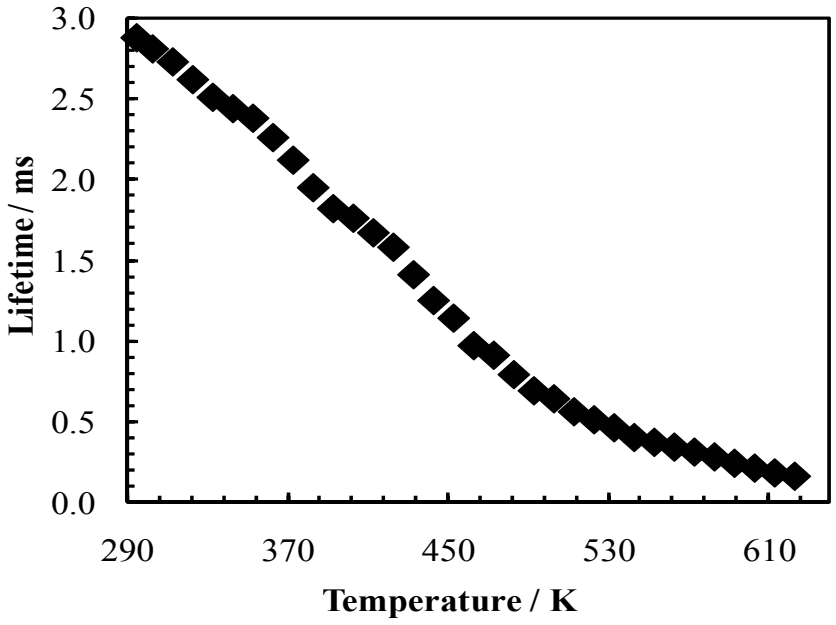

Figure 4-10 Life time decay of Cr:Al_2O_3 at different temperatures

4.2 Experimental procedure

The flow of cooling water was started 15 min before the fuel gas is ignited in order to attain temperature uniformity in the experimental setup. The premixed feed gases, such as methane, hydrogen and air, then enter the burner and are ignited. The lifetime of the phosphorescence from both sides of the plate was measured before the gas mixture was ignited in order to check that the lifetime at the cooling water temperature matches the calibration curve. The following lifetime measurements for the burning flame were taken under steady state conditions, which were considered to be reached when the temperature of the outlet water became constant. The phosphorescence signal from both sides was recorded simultaneously, and each measurement was repeated three times in order to estimate the deviation. The average was taken for further evaluation.

As mentioned previously, two different types of burners were in use; a flat burner for cold feed gas velocities of 0.1 m/s to 0.5 m/s (in steps of 0.1 m/s). These cold gas velocities are below the free flame velocity for the stoichiometric methane air flame, which leading to a burner stabilized flame. At higher velocities, the flames shows cellular structures on the matrix burner. The nozzle burner was used for higher cold feed gas velocities of 0.7 m/s, 0.9 m/s, 1 m/s, and 1.2 m/s; however, at lower velocities, it is not appropriate since the flame will stabilize inside the tube. Experiments for the methane flames were carried out at three stoichiometries, stoichiometric (φ =1), lean (φ = 0.75) and rich (φ = 1.25), at the smallest burner-to-plate distance (H=15 mm). For the stoichiometric flame, the measurements were repeated for larger burner-to-plate distances, namely H = 30mm and H = 60mm. For hydrogen/methane/ air flames all the experiments were carried out for at stoichiometric (φ =1) for mixtures of air with different hydrogen contents.

4.2.1 Surface temperatures and heat flux analysis

In the present study, the aim was to measure surface temperatures and to derive from these the heat fluxes at the stagnation surface. The temperature measurement method is based on measuring the lifetime of the phosphorescence of an excited inorganic phosphor after excitation with a light pulse. The lifetime is a function of temperature, thus the temperatures can be extracted from the time dependent phosphorescence intensity.

As motioned previously in chapter 3, equation (3.6), the decay time is usually found by fitting the experimental signal to a simple exponential function, which describes the signal shape well in the present case:

$$I = I_0 \exp\left(-\frac{t}{\tau}\right) \tag{4.1}$$

The surface temperature on the flame side of the ceramic plate is an important boundary condition for the modeling of the flame. In order to obtain the local heat flux rate in the center of the plate, where the assumption of a one dimensional stagnation flow is reasonable, simultaneous measurement of the temperatures from both sides are needed. This was achieved by using phosphorescence thermometry also from the water cooled back side of the ceramic plate. Figures 4.8 and 4.9 show typical phosphorescence signals on the flame side and on the cooled side of the stagnation plate, leading to temperatures of 377.33 K and 336.65 K, respectively.

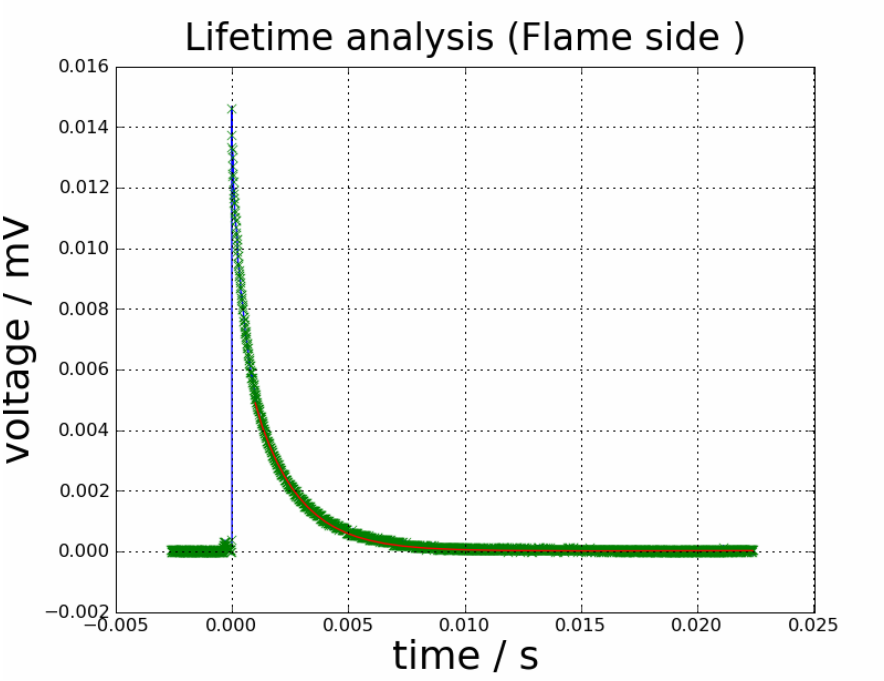

Figure 4-11 Lifetime analysis for the plate, heated side (Laser excitation)
(red: measured, green: fit)

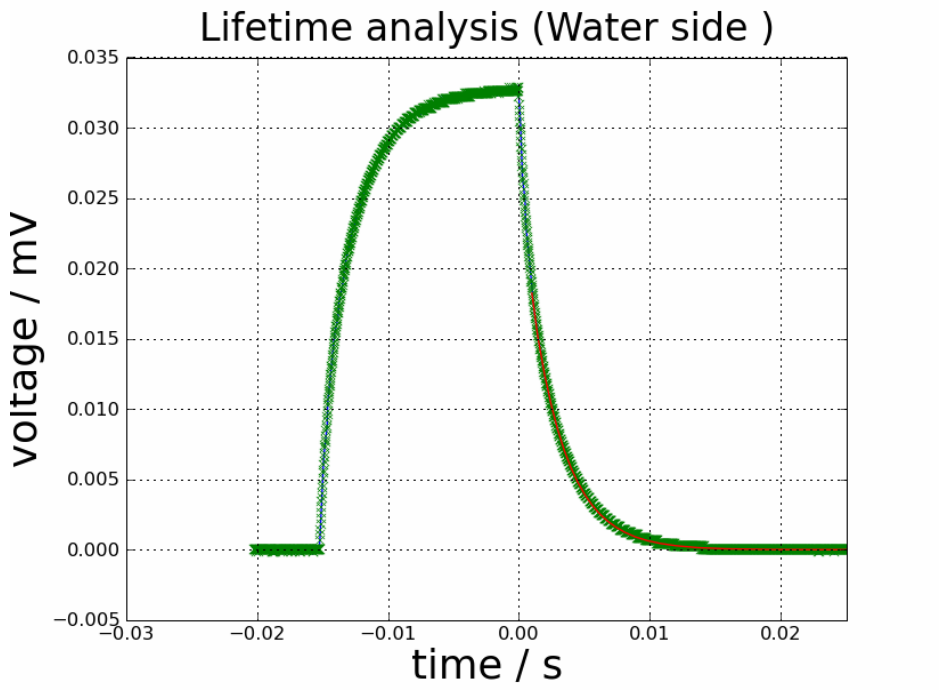

Figure 4-12 Lifetime analysis for the plate, cooled side (LED excitation)
(red: measured, green: fit)

On the above-mentioned figures, fitted curves using the parameters of the calibration measurements are included. As mentioned in 2.5.1, the calculated temperature difference can then be used to determine the one dimensional heat flux through the centre of the ceramic plate:

$$\dot{q} = \frac{\dot{Q}}{A} = -k\frac{\Delta T}{L}$$

4.2.2 Temperature measurement with OH-LIF

In order to validate the modeling results for some of the flames, gas phase temperatures in the central part of the flames were measured using OH-LIF thermometry by S. Staude (Salem et al. [83]).

Laser induced fluorescence (LIF) is one such technique, which is capable of measuring concentration of some radical species such as OH, CH, C2 at the ppm, and even sub-ppm levels [87]. As the determination of the concentrations of these species is important for many combustion studies, LIF offers the advantages that principally each of these species can also used as thermometer without changing the experimental arrangement [88] . Usually, OH serves as the indicator species, because it is found in the reaction zone of the flame and in high temperature regions in high temperature concentrations. In LIF, as shown schematically in Fig. 4.13, the molecule under investigation is excited to an upper electronic level, and the spontaneous emission from the upper level is detected.

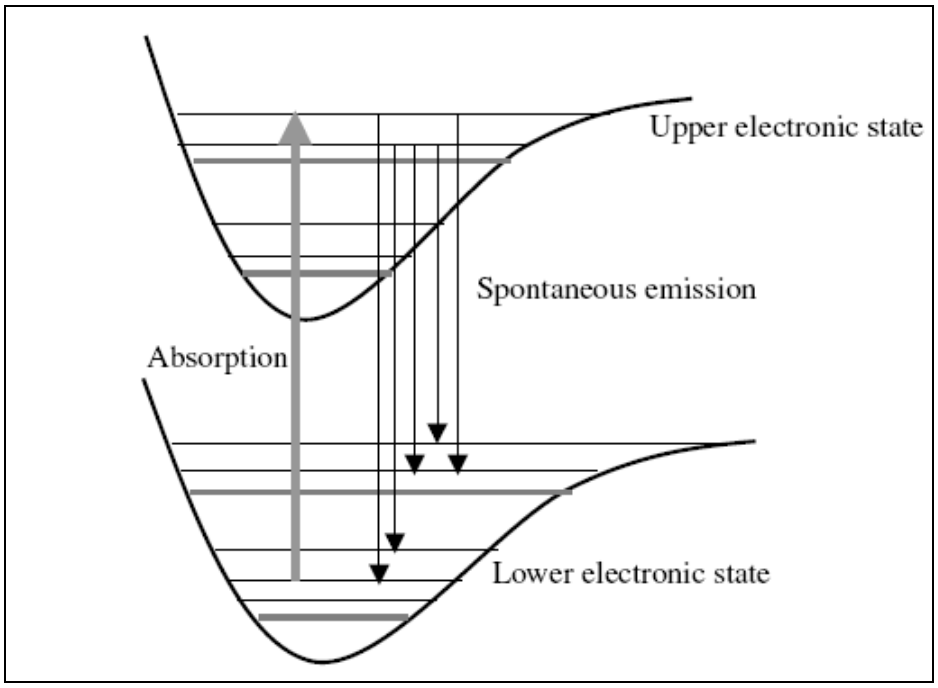

Figure 4-13 Laser induced incandescence (LIF) phenomenon

Often, the detected wavelength is different from the excitation wavelength to avoid the interferences due to Rayleigh or Mie scattering. Resonant absorption has much larger cross section than Raman processes. Therefore, LIF is orders of magnitude stronger than Raman scattering, providing higher detection sensitivity [89].

The fluorescence signal F can be written as:

$$F = h\nu N_2 A_{21} \frac{\Omega}{4\pi} lA, \tag{4.2}$$

where hν is photon energy, Ω is the collection solid angle, l is the axial distance along the laser beam, A_{21} is the spontaneous emission rate and A is the focal area of the laser beam. At low laser irradiances, the fluorescence signal is in the linear regime, that is, linearly proportional to the input laser irradiance. In this situation, when depopulating the excited level is dominated by non-radiative transfer to the ground

state as result of collisions with surrounding molecules (quenching), the fluorescence signal is determined by following equation:

$$F = \frac{h\nu}{c} A_{21} \frac{\Omega}{4\pi} lA \frac{N_1{}^0 B_{12} I^v}{(Q_{21} + A_{21})}, \tag{4.3}$$

where I^v is the incident laser irradiance, B_{12} is the Einstein coefficient for absorption, Q_{21} is the collisional quenching rate and $N_1{}^0$ is total number of molecules. The term $\frac{A_{21}}{A_{21} + Q_{21}}$ is called as the fluorescence yield.

In the current study the OH was excited in the A-X 1-0 vibrational band with a Nd:YAG-pumped, frequency-doubled dye laser in the spectral region from 35357 to 35388 cm^1. In this region there are five distinct peaks of the A-X 1-0 band. The relative sizes of the $P_{21}(5.5)$ and the $Q_1(5.5)$ rotational lines give a good indication of the level of saturation, whilst the three other lines in this spectral range (namely $R_1(14.5)$, $P_1(2.5)$ and $R_2(12.5)$) are very temperature sensitive, since the lines of the R-branch increase in intensity as the temperature increases, whilst the P_1 line decreases with increasing temperature.

For the LIF measurements, the laser beam was formed into a laser sheet of about 10 mm in height and passed through the flame just below the plate. The fluorescence signal was collected at approximately right angles by an intensified CCD camera (PCO) through a UV objective (Nikkon) and a band pass filter (Schott UG11). Within each image was also an area where the laser beam was reflected on the plate some distance from the flame. This region was used as an indication of the laser intensity, so that shot-to-shot variations in the laser strength could be accounted for. The scan was performed in steps of 0.0005 nm; at each wavelength the signal was averaged over 16 shots.

The resulting images were analyzed by pixel row, where one row corresponds to an area of 0.15 mm in height of the flame. For each vertical position in the flame a spectrum was generated by averaging over the central 4 mm of the flame region, then subtracting the measured intensity without a laser signal (baseline) and finally dividing by the relative laser intensity for each image. The resulting spectra were then fitted to simulated spectra using the LIF program of J. Heinze(Atakan et al. [90], with temperature, offset, offset ramp, saturation and laser line shape as fit parameters. A typical spectrum together with a fit is shown in Figure 4.10.

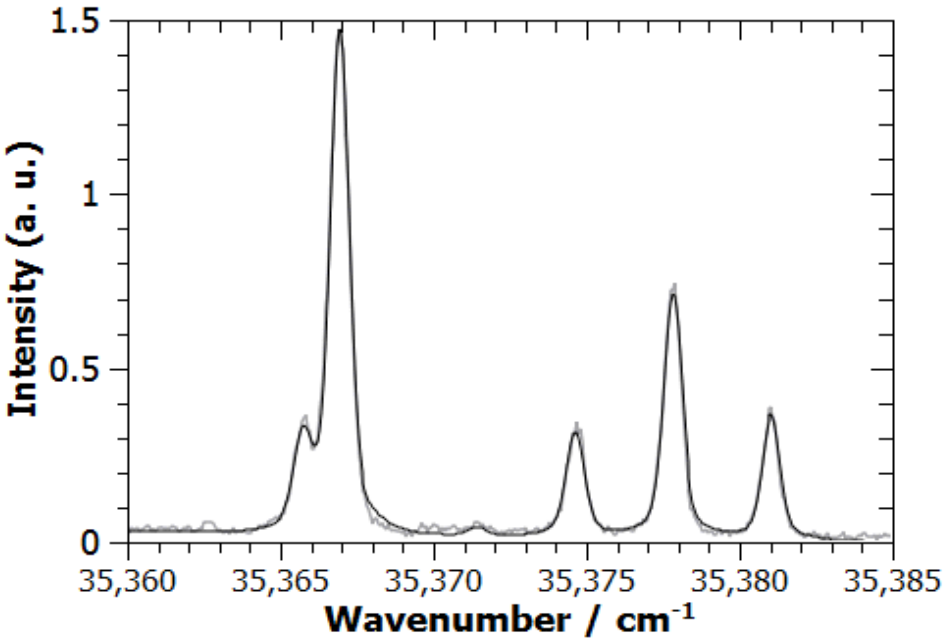

Figure 4-14 LIF absorption spectrum, measured (grey) and fit (black)

4.3 Modeling

The stagnation point flames were modeled as one-dimensional flows with detailed chemistry and transport processes by B. Atakan (Salem et al. [83]) using the Cantera code [91], where the similarity solution for the flow is implemented. The mechanism used was GRI 3.0 including 325 reactions of 53 species and the program solves the one dimensional balances for momentum, energy and species. Regarding the transport coefficients two models are implemented to Cantera: a mixture averaged model and a multispecies model. Calculations were performed using both, leading to similar results, so that the simpler mixture-averaged model results are presented here.

The temperatures at the burner surface and at the stagnation plate were provided as boundary conditions, while no surface reactions were included. Since it was found that changes within 20-40 K at the boundaries did not influence the results strongly, the burner surface temperature at z=0 was fixed to 338 K, in coincidence with a thermocouple measurement. The calculations were repeated for several stagnation surface temperatures, but again finding that the calculated heat flux rates were only weakly influenced by the exact value.

In order to obtain the heat flux from the model, the conductive heat flow to the surface had to be evaluated. For this one-dimensional system, the temperature gradient at the surface on the gas side had to be evaluated as well as the conductivity (k) of the resulting gas mixture adjacent to the stagnation surface. Directly at the surface a no-slip boundary condition is applied, so that conduction of heat is the remaining local mechanism for heat transfer. Using Fourier's law for the gas phase:

$$\dot{q} = k_{gas}\left(\frac{dT}{dz}\right)_{gas,z=surface} \tag{4.4}$$

The gradient was evaluated from the temperatures of the final three grid points adjacent to the surface. The point next to the surface was fixed to a distance of 1μm, while the next points were typically at distances between 10 and 100μm, which ensured that flow velocities contributions to heat transfer at these positions were negligible. A polynomial was calculated from them, and the slope at the surface was taken from the first derivative at the location of the surface. No radiative heat flux is included in the energy balance of the flame model, thus the heat flux may be underestimated. However, an estimation using the values from text books showed that the error should at most be in the area of a percent of the total calculated heat flux.

CHAPTER FIVE

UNCERTAINTY ANALYSIS

5 Uncertainty Analysis

The measurement of a physical quantity can never be made with perfect accuracy, there will always be some error or uncertainty present. For any measurement there are an infinite number of factors that can cause a value obtained experimentally to deviate from the true (theoretical) value. Most of these factors have a negligible effect on the outcome of an experiment and can usually be ignored. However, some effects can cause a significant alteration, or error, in the experimental result. If a measurement is to be useful, it is necessary to have some quantitative idea of the magnitude of the errors. Therefore, when experimental results are reported, they are accompanied by an estimate of the experimental error, called the uncertainty. This uncertainty indicates how reliable the experimenter believes the results to be. Before starting the error estimation of the current experimental results, let us first consider some important terms shall be considered, that are commonly used in error analysis. These terms are especially crucial for understanding the uncertainty analysis of the experimental results [92]. Error in a measurement is defined as the difference between its true value and the measured value. Uncertainty is used to refer to a possible value that an error may have.

5.1 Types of Errors

In order to determine the uncertainty for a measurement, the nature of the errors affecting the experiment must be examined. There are many different types of errors that can occur in an experiment, but they will generally fall into one of two categories: random errors or systematic errors.

5.1.1 Random errors

Random errors usually result from human and from accidental errors. Accidental errors are brought about by changing experimental conditions that are beyond the control of the experimenter; examples are vibrations in the equipment, changes in the humidity, fluctuating temperatures, etc. Human errors involve such things as miscalculations in analyzing data, the incorrect reading of an instrument, or

a personal bias in assuming that particular readings are more reliable than others. By their very nature, random errors cannot be quantified exactly since the magnitude of the random errors and their effect on the experimental values is different for every repetition of the experiment. So statistical methods are usually used to obtain an estimate of the random errors in the experiment. Even in a carefully designed experiment, random errors can still affect the results. The causes of random errors are not always easy to identify or to do something about. Since they are random, they are just as likely to give a measured value that is high as it is low. Because of this, it is possible to analyze random errors statistically, and to be more confident of a result based on multiple measurements.

5.1.2 Systematic errors

A systematic error is an error that will occur consistently in only one direction each time the experiment is performed, i.e., the value of the measurement will always be greater (or lesser) than the real value. Systematic errors most commonly arise from defects in the instrumentation or from using improper measuring techniques. For example, measuring a distance using the worn end of a meter stick, using an instrument that is not calibrated, or incorrectly neglecting the effects of viscosity, air resistance and friction, are all factors that can result in a systematic shift of the experimental outcome.

Although the nature and the magnitude of systematic errors are difficult to predict in practice, some attempt should be made to quantify their effect whenever possible. In any experiment, care should be taken to eliminate as many of the systematic and random errors as possible. Proper calibration and adjustment of the equipment will help reduce the systematic errors leaving only the accidental and human errors to cause any spread in the data. In the current study all the equipments (such as gas mass flow controllers and thermocouples) were calibrated periodically according to the standards. Although there are statistical methods that will permit the reduction of random errors, there is little use in reducing the random errors below the limit of the precision of the measuring instrument.

5.2 Precision vs. Accuracy

If repeated determinations of a measurement are made, and the repetitions are grouped closely together, the measurement is said to be precise. If a measurement is very close to the true value, the measurement is said to be accurate. In an experiment one tries to be precise and accurate. Systematic errors are more likely to affect the accuracy of an experiment while random errors are more likely to affect the precision of an experiment. Failure to correct for systematic errors can cause precise results that are wrong (i.e., they are inaccurate).

5.3 Absolute Error

There are several ways to express the error in a measurement. If the error is expressed in the same units as the measurement, it is known as an absolute error. Absolute errors are typically stated to one significant figure. The absolute error with a meter stick might be ± 0.001 m.

5.4 Relative Error

The fractional or relative error is the absolute error, divided by the measurement. The percent error is the fractional error multiplied by 100. For example, if you measured an object to be 0.567±0.001 m, the percent error would be:

$$\frac{0.001}{0.567}100\% = 0.18\%$$

5.5 Mean

If an infinite number of measurements is made, the average of these measurements will be mean $\overline{x}$. Suppose N measurements of some quantity were taken, and denoted by x_1, x_2, … x_N, then the mean $\overline{x}$ is given by:

$$\overline{x} = \frac{1}{N}\sum_{i=1}^{N} x_i \qquad (5.1)$$

This estimate of the mean is often referred to as the sample mean in statistical analysis. It will be referred to here as the mean, even though it is really only an estimate of the mean.

5.6 Standard Deviation

The standard deviation is often denoted by the Greek letter sigma, σ. The variance is σ^2. For a finite number of measurements, x_i, the standard deviation is given by:

$$\sigma = \left(\frac{1}{N-1} \sum_{i=1}^{N} (x_i - \bar{x})^2 \right)^{1/2} \tag{5.2}$$

The standard deviation tells us something about how close our measurements are to the mean. If σ is small, that means random errors are small, and the precision of the measurements is high. This can be seen by examining the formula for σ.

5.7 Root-Sum-Square (RSS) combination:

The objective of this scheme is to express the uncertainty in the calculated result at the same odds as were used in estimating the uncertainties in the measurements [93] . The effect of uncertainty in a single measurement on the calculated result would be:

$$\delta R_{X_i} = \frac{\partial R}{\partial X_i} \delta X_i \tag{5.3}$$

Where δ is the error and ∂ is the partial derivative. If R is the sum and difference of several quantities X_i, then the uncertainty in R is given by [92] :

$$\delta R = \sqrt{(\delta X_1)^2 + ... + (\delta X_i)^2} \tag{5.4}$$

If R is the product and quotient of several quantities X_i, then the uncertainty in R is given by:

$$\frac{\delta R}{R} = \sqrt{\left(\frac{\delta X_1}{X_1}\right)^2 + \ldots\ldots\ldots + \left(\frac{\delta Xi}{Xi}\right)^2} \tag{5.5}$$

When several independent variables are used in the function R, the individual terms are combined by the root-sum-square method:

$$\delta R = \left\{ \sum_{i=1}^{N} \left(\frac{\partial R}{\partial X_i} \delta X_i \right)^2 \right\}^{1/2} \tag{5.6}$$

This is the basic equation of uncertainty analysis. Each term represents the contribution made by the uncertainty in one variable δX_i, to the overall uncertainty in the result, δR. The estimated uncertainty in the result has the same probability of encompassing the true value of the result as the uncertainties in the individual measurements have of encompassing their true values. Whenever the equation describing the result is a pure product form such as:

$$R = X_1^a X_2^b X_3^c \ldots\ldots X_M^m \tag{5.7}$$

then the relative uncertainty can be found out directly by:

$$\frac{\delta R}{R} = \left\{ \left(a \frac{\delta X_1}{X_1} \right)^2 + \left(b \frac{\delta X_2}{X_2} \right)^2 + \ldots\ldots + \left(m \frac{\delta X_m}{X_m} \right)^2 \right\}^{1/2} \tag{5.8}$$

5.8 Error Estimation

The following subsections of this chapter will include the detailed estimation of errors in the current study, including the calibration data, the lifetime, the surface temperatures measured on both side of the ceramic coated plate, the thermal conductivity , and finally the calculated heat fluxes.

5.8.1 Calibration data (lifetime) error estimation

As mentioned in 4.2.1, the coated ceramic plate was calibrated before it was used for surface temperature measurement. The phosphorescence was excited with a green LED at about 30 different temperatures in range of 295-600K.The emission

signal of the phosphorescence was recorded and the decay time was evaluated. This process was repeated two times and the errors were estimated as given in the table no.5.1:

Plate surface temperature (K)	Lifetime first measurement (ms)	Lifetime second measurement (ms)	Average Lifetime (ms)	Error (ms)	Relative Error %
303.15	3.06	3.03	3.045	0.021213	0.696657
308.15	3.01	2.98	2.995	0.021213	0.708287
313.15	2.95	2.92	2.935	0.021213	0.722767
318.15	2.9	2.87	2.885	0.021213	0.735293
323.15	2.83	2.8	2.815	0.021213	0.753577
328.15	2.76	2.75	2.755	0.007071	0.256663
333.15	2.71	2.68	2.695	0.021213	0.787132
338.15	2.64	2.61	2.625	0.021213	0.808122
343.15	2.56	2.55	2.555	0.007071	0.276754
353.15	2.43	2.42	2.425	0.007071	0.29159
358.15	2.35	2.33	2.34	0.014142	0.604365
363.15	2.27	2.26	2.265	0.007071	0.312188
368.15	2.22	2.2	2.21	0.014142	0.639916
373.15	2.16	2.14	2.15	0.014142	0.657774
378.15	2.11	2.09	2.1	0.014142	0.673435
383.15	2.05	2.04	2.045	0.007071	0.345773
388.15	2.01	1.99	2	0.014142	0.707107
393.15	1.93	1.94	1.935	0.007071	0.36543
398.15	1.85	1.87	1.86	0.014142	0.76033
403.15	1.78	1.81	1.795	0.021213	1.181794
413.15	1.66	1.67	1.665	0.007071	0.424689
428.15	1.47	1.48	1.475	0.007071	0.479394
438.15	1.32	1.33	1.325	0.007071	0.533665
443.15	1.26	1.27	1.265	0.007071	0.558978
448.15	1.22	1.21	1.215	0.007071	0.581981
453.15	1.16	1.17	1.165	0.007071	0.606959
458.15	1.12	1.1	1.11	0.014142	1.274066
463.15	1.06	1.04	1.05	0.014142	1.34687
478.15	0.9	0.91	0.905	0.007071	0.781333
483.15	0.86	0.87	0.865	0.007071	0.817464
488.15	0.83	0.82	0.825	0.007071	0.857099
493.15	0.79	0.77	0.78	0.014142	1.813094
498.15	0.75	0.73	0.74	0.014142	1.911099
503.15	0.71	0.69	0.7	0.014142	2.020305
508.15	0.67	0.66	0.665	0.007071	1.063318
513.15	0.62	0.63	0.625	0.007071	1.131371
523.15	0.57	0.58	0.575	0.007071	1.229751

Table 5-1 Lifetime decay calibration errors of Cr^{+3}:Al_2O_3 (ruby)at different temperatures

Figure 5.1 shows the relative errors in the lifetimes are below 2%, which give good indication that, the thermographic phosphors using the lifetime method for measuring the surface temperatures was very precise.

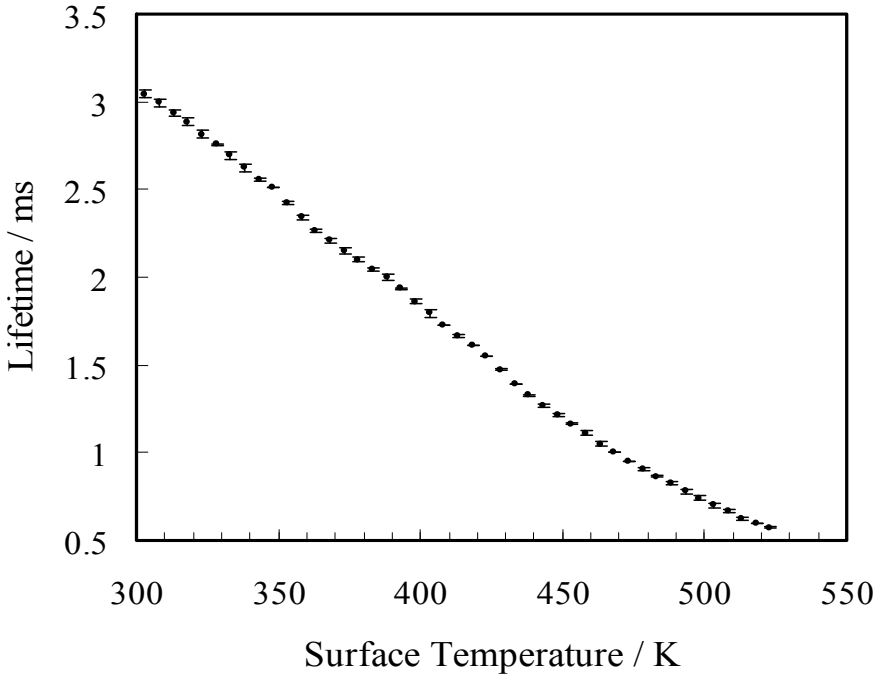

Figure 5-1 Lifetime decay of $Cr:Al_2O_3$ (ruby) at different temperatures

5.8.2 Experimental measurements error estimation

5.8.2.1 Heat flux error estimation

As mentioned previously in 2.5.1 the one dimensional heat flux is calculated using the formula:

$$\dot{q} = -k\frac{\Delta T}{\Delta x}$$

where ΔT is the temperature difference between the two surfaces i.e. the flame side and the water side and Δx is the thickness of the plate. So in order to calculate the error in the heat flux we have to calculate the errors in ΔT and thermal conductivity k. Since the thickness of the plate is known (6±0.1 mm), the

error in Δx was neglected. In the following sub-sections detailed analysis of these errors will presented.

5.8.2.2 Temperature error estimation

- **Plate heated side (flame side) :**

Mass flux (Kg/ sm²)	First temperature measurement (K)	Second temperature measurement (K)	Third temperature measurement (K)	Average temperature (K)	Error (K)	Relative Error %
0	296.88	295.88	295.85	296.20	0.5862025	0.1979026
0.13	335.72	337.45	334.74	335.97	1.372188	0.4084258
0.26	347.62	344.83	347.65	346.70	1.619537	0.4671292
0.38	364.15	362.98	363.98	363.70	0.6321656	0.1738135
0.51	370.85	372.09	371.55	371.49	0.621718	0.1673549
0.64	377.12	378.96	379.45	378.51	1.2284543	0.32455
0.89	385.54	385.34	384.52	385.13	0.5404936	0.1403393
1.14	400.12	397.69	398.31	398.70	1.2626295	0.3166813
1.27	402.63	405.21	408.91	405.58	3.1566015	0.7782868
1.53	412.72	413.19	410.14	412.01	1.6421429	0.3985623

Table 5-2 Surface temperature error on ceramic plate (flame side)

- **Plate cooled side (water side) :**

Mass flux (Kg/ sm²)	First temperature measurement (K)	Second temperature measurement (K)	Third temperature measurement (K)	Average temperature (K)	Error (K)	Relative Error %
0	296.88	295.13	296.21	296.20	0.8826219	0.2979741
0.13	307.08	307.73	308.31	307.70	0.6153319	0.1999735
0.26	314.81	313.29	315.69	314.59	1.2141389	0.3859351
0.38	323.35	321.55	324.56	323.15	1.5146067	0.468696
0.51	327.71	326.92	331.56	328.73	2.4824786	0.7551725
0.64	336.68	335.65	336.25	336.19	0.5173329	0.1538796
0.89	340.43	338.56	338.25	339.08	1.1830296	0.3488918
1.14	346.89	347.66	346.85	347.13	0.4560132	0.1313652
1.27	351.405	353.43	349.54	351.45	1.9455483	0.5535644
1.53	353.16	354.74	351.48	353.12	1.6302556	0.4616631

Table 5-3 Surface temperature error on ceramic plate (water side)

Figure 5.2 shows the relative errors for surface temperature measurement on both sides of the plate. The errors are relatively small, but there are some fluctuations in the temperatures measurement due to some random errors, such as very small changes in the water cooling flow rates, which are very difficult to be observed. Also changes of the flame structure may affect the measurements, which also are difficult to control. As a result these types of errors will increase the total errors in the heat fluxes.

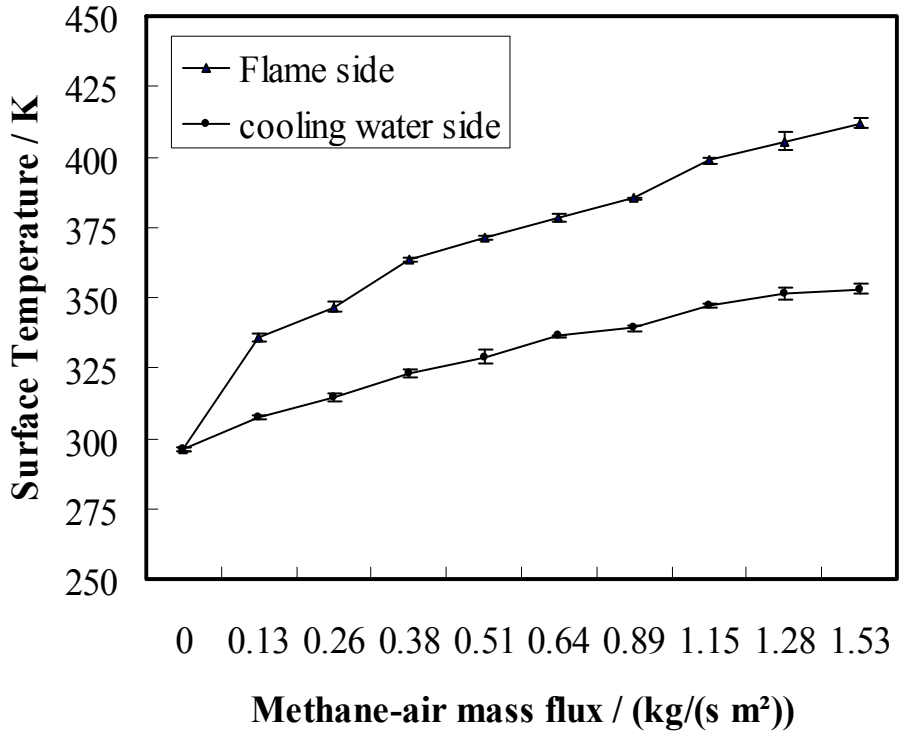

Figure 5-2 surface temperature measurement on both sides of the ceramic plate (at φ = 1 and H = 15 mm)

5.8.2.3 Temperature difference (ΔT) error estimation

$$\Delta T = T_{average}\ (FS) - T_{average}(WS) \tag{5.9}$$

Where, FS and WS are the heated side (flame side) and cooled side (water side) of the ceramic plate respectively, therefore:

$$\delta\Delta T = \sqrt{(\delta T(FS))^2 + (\delta T(WS))^2} \tag{5.10}$$

Mass flux (Kg/ (sm²)	ΔT (K)	Error (K)	Relative error %
0.13	28.26	1.503839	5.320814
0.26	32.10	2.024113	6.304993
0.38	40.55	1.641239	4.047446
0.51	42.76	2.559147	5.983975
0.64	42.31	1.332941	3.149921
0.89	46.05	1.300650	2.824358
1.14	51.57	1.342453	2.603032
1.27	54.12	3.708003	6.850815
1.53	58.89	2.313950	3.929275

Table 5-4: Surface temperature difference (ΔT) errors

5.8.2.4 Thermal Conductivity (k) error estimation

As mentioned in 2.5.1 the average values of thermal conductivity on the both sides the used alumina plate were used. It turns out that the published absolute thermal conductivities of alumina were obtained from three different techniques; namely, calorimetry, hot-wire, and Laser-flash [94]. The measured thermal conductivity values of three methods varied by about 20%, so it is so difficult to know which value could be used for the calculation of the heat fluxes. As a result the calculated values of the heat fluxes will be different, depending on which thermal conductivity values have been used. Due to this the total measurement uncertainty is increased.

The thermal conductivity values, which were used to calculate the heat fluxes in the current study were obtained using Laser flash thermal technique. Table 5.5 shows the estimated relative errors of the thermal conductivity due to surface temperature variation. Their errors were relatively small. The Laser-flash technique yielded average calculated thermal conductivity values ranging from 22.2 W/mK at 298 K to10 W/mK at 673 K.

Mass flux (Kg/ sm²)	Average k1 (W/m.K)	Average k2 (W/m.K)	Average k3 (W/m.K)	Average k (W/m.K)	Error (W/m.K)	Relative Error %
0	22.2607557	22.3267457	22.3015942	22.296365	0.0333043	0.1493709
0.13	21.084	21.02688	21.078	21.06296	0.0313899	0.1490288
0.26	20.61288	20.71632	20.59104	20.64008	0.0669227	0.3242367
0.38	20.0112	20.08248	19.98624	20.02664	0.0499433	0.2493841
0.51	19.74576	19.73496	19.63656	19.70576	0.0601718	0.3053511
0.64	19.38	19.36056	19.3344	19.35832	0.0228824	0.1182044
0.89	19.0877663	19.1376	19.16472	19.130029	0.0390315	0.2040328
1.14	18.582912	18.6228	18.62736	18.611024	0.0244522	0.1313858
1.27	18.41436	18.30384	18.3084	18.3422	0.062534	0.3409295
1.53	18.13008	18.08088	18.23232	18.14776	0.0772525	0.4256864

Table 5-5: Thermal conductivity (k) errors on both sides of the ceramic plate

According to the root-sum-square method (Kline and McClintok) [95] the error in the heat flux is given by:

$$\delta\dot{q} = \sqrt{(\delta\Delta T)^2 + (\delta\Delta x)^2 + (\delta k)^2} \tag{5.11}$$

Since the thickness of the plate is exactly known we neglect the error in Δx and only the errors in ΔT and k contribute to the error in heat flux. In the current study, the error in heat flux was calculated using the standard deviation of the results obtained from the formula of heat flux and also by the root sum square method. Both the errors calculated are given in the tables below:

Mass flux (Kg/ sm²)	First Heat Flux (kW/m²)	Second Heat Flux (kW/m²)	Third Heat Flux (kW/m²)	Average Heat Flux (kW/m²)	Error (kW/m²)	Relative Error %
0.13	100.640	104.153	92.848	99.214	5.785750	5.8315732
0.26	112.718	108.898	109.681	110.432	2.017433	1.8268418
0.38	136.076	138.669	131.309	135.351	3.733055	2.7580395
0.51	141.972	148.571	130.877	140.473	8.941497	6.3652473
0.64	130.621	139.750	139.207	136.526	5.121451	3.7512478
0.89	143.487	149.209	147.791	146.829	2.979720	2.0293711
1.14	164.855	155.283	159.760	159.966	4.789359	2.9939798
1.27	157.212	157.962	181.161	165.445	13.61575	8.2297565
1.53	179.971	176.137	178.251	178.120	1.920039	1.0779464

Table 5-6: Calculated heat flux errors using standard deviation

Using Root-Sum-Square method:

Mass flux (Kg/(sm²)	ΔT (K)	Relative Error ΔT %	Average Thermal conductivity (k) (W/m.K)	Thermal conductivity Relative Error %	Average Heat Flux (kW/m²)	Heat Flux Error	Relative Error %
0	0	0	22.2963	0.14937	0	0	0
0.13	28.263	5.3208	21.0629	0.14902	99.2142	5.2810755	5.322901
0.26	32.103	6.3049	20.6400	0.32423	110.432	6.9719832	6.313325
0.38	40.550	4.0474	20.0266	0.24938	135.351	5.4886786	4.055122
0.51	42.766	5.9839	19.7057	0.30535	140.473	8.416848	5.991762
0.64	42.316	3.1499	19.3583	0.11820	136.526	4.3035077	3.152138
0.89	46.051	2.8243	19.1300	0.20403	146.829	4.1578047	2.831718
1.14	51.572	2.6030	18.6110	0.13138	159.966	4.1692769	2.606347
1.27	54.125	6.8508	18.3422	0.34092	165.445	11.348388	6.859293
1.53	58.890	3.9292	18.1477	0.42568	178.120	7.0397847	3.952267

Table 5-7: Calculated heat flux errors using Root-Sum-Square method

Figure 5.3 shows the error bars for the calculated heat fluxes using the root sum square method.

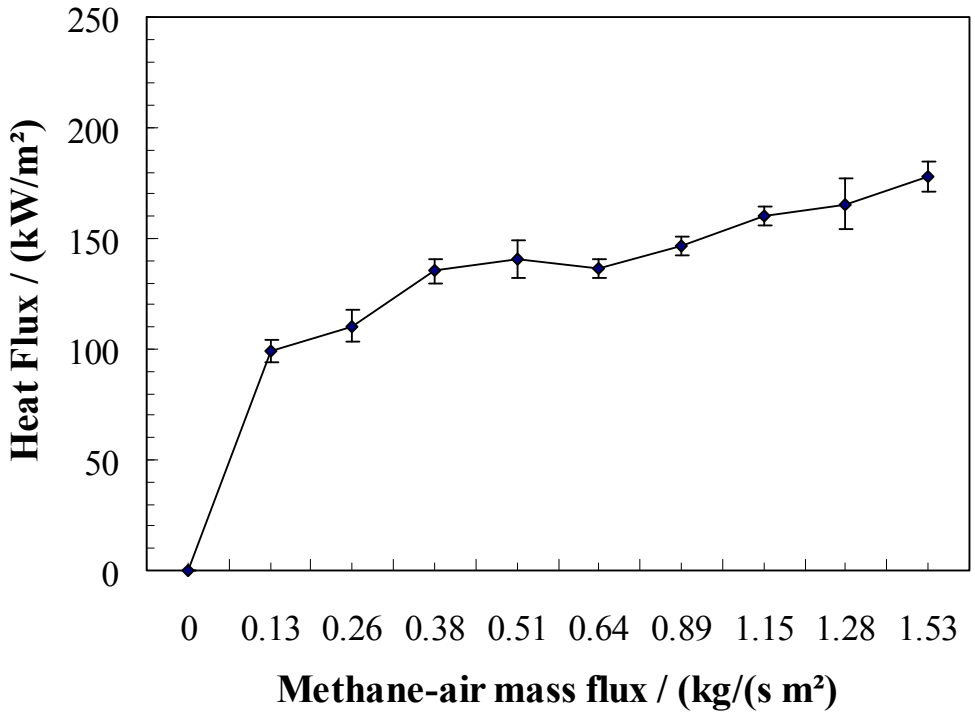

Figure 5-3 Stagnation point heat flux for stoichiometric methane flame (φ = 1 and H = 15 mm)

CHAPTER SIX

RESULTS AND DISCUSSION

6 Results and Discussion

6.1 Methane / air Premixed flames

6.1.1 Surface temperature measurement

Methane/air flames of three different stoichiometries were investigated at three burner to plate distances. For each of those the cold gas velocity was varied. The signal-to-noise ratio was very good even for the small distance of 15 mm between the burner and the stagnation plate Figure 6.1 shows the surface temperature measurement on both side of the ceramic plate as a function of methane air mixture

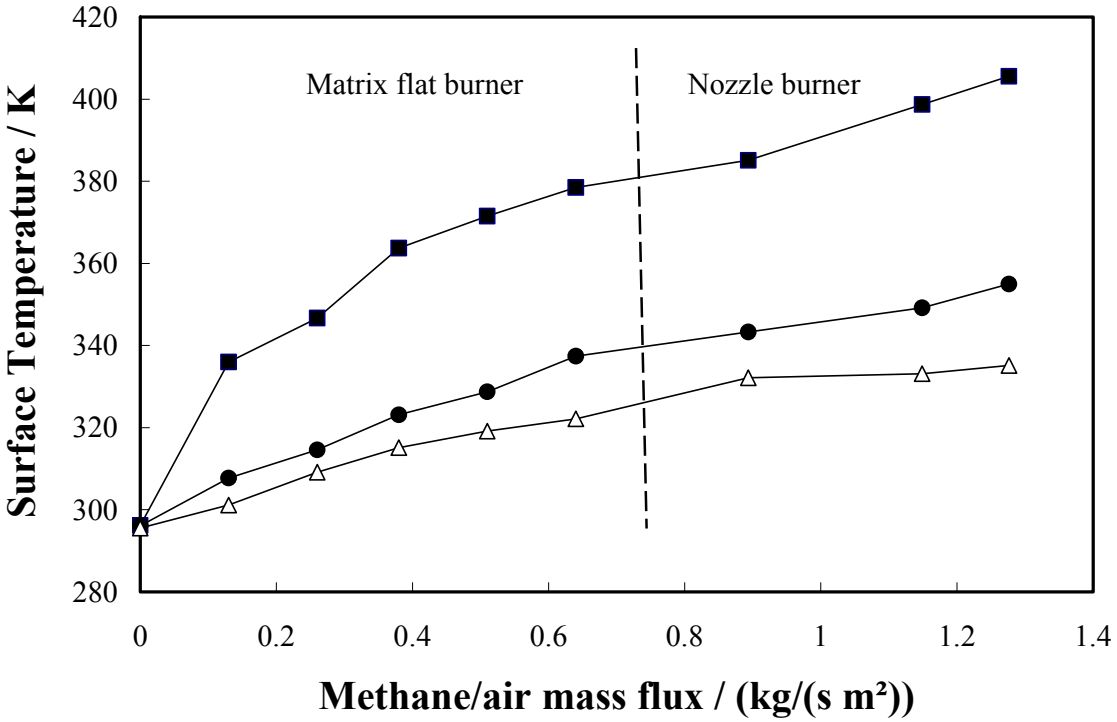

Figure 6-1 Surface temperature measurement on the heated side and cooled side for stoichiometric methane flame (solid square heated side (TP), solid circle cooled side (TP), hollow triangle cooled side (Thermocouple))

flux for stoichiometric flame (φ=1). The matrix flate burner was used for mass fluxes below 0.7 kg/(m^2 s)at the smallest distance of 15 mm, which can be regarded

effectively as one dimensional and the nozzle burner was used for higher mass fluxes. In both cases, the increase of the temperature on both sides of the plate is observed; however, there was no observable effect of replacing the flat burner by the nozzle burner regarding the slop of the surface temperature vs. mass flux curve.

Accompanying thermocouple measurement of the plate surface on the cooling water side, which are lower by 2-10 K, demonstrating the problem of thermal contact resistance. In order to reduce the uncertainty and prove the reproducibility of the measurements, they were repeated several times; the relative errors in the lifetime measurement were below 0.5 % at temperatures below 500 K and the error in the temperature is estimated to be below 2-5 K, depending on the exact temperature. . The temperature differences between the flame side and the water cooled side vary between 20K and 56K.

Figure 6.2 shows the surface temperature measurement on both sides of the ceramic plate as a function of methane-air mixture mass fluxes and with stoichiometries of 0.75, 1 and 1.25 at a distance of 15 mm. For the stoichiometric flame, the temperatures on the water side vary between 310 and 345K for the different flames. The value at a mass flux of 0 is the cold gas measurement. On the flame side, temperatures between 335K and 410 K were found. With an increasing mass flux of the fresh gases, the temperature difference increases and also the heat flux increases.

As expected, the highest surface temperatures were found for the stoichiometric flame. Interestingly, the surface temperatures for the rich flame were found to be very close to the stoichiometric flame. It was initially supposed that since the flame was burning at ambient conditions, additional air may have leading to lower real stoichiometries. However, even if air entrainment plays some role, it is unlikely that air from the surrounding can contribute considerably to the stoichiometry at the investigated small distance of 15 mm, regarding the burner diameter of 30 mm. Since a similar trend regarding the heat flux is also found in modeling, it is concluded that the air entrainment effect may be a minor one.

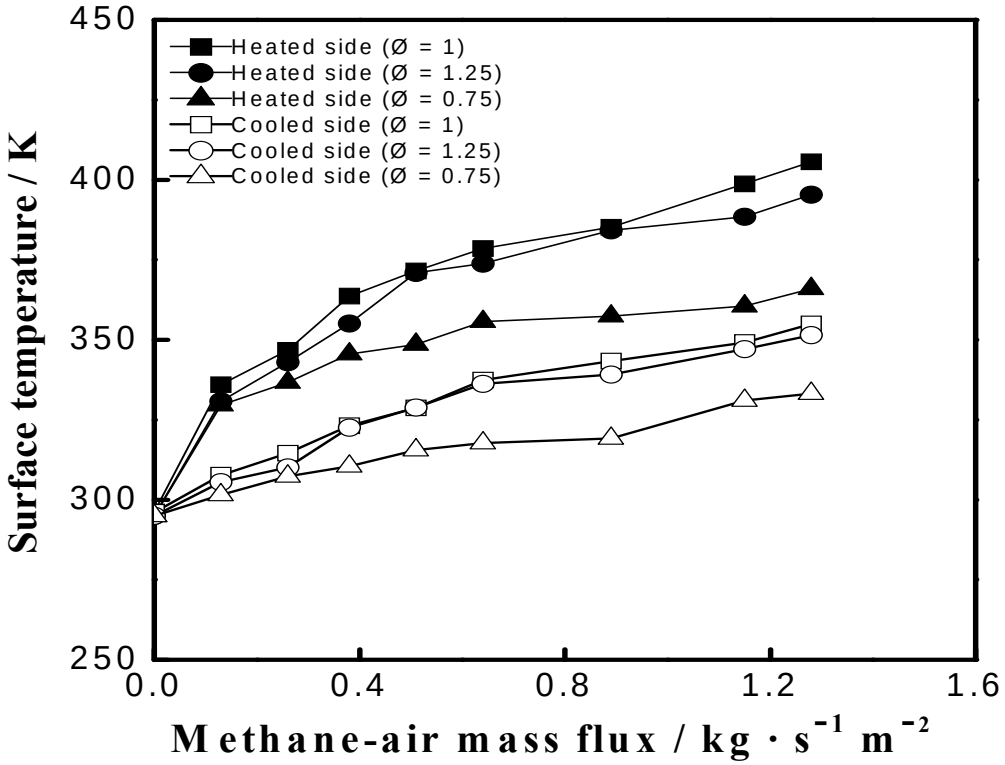

Figure 6-2 Surface temperature measurement at (H = 15 mm) for various equivalence ratios

Analysis of the heat fluxes (see also below) lead to the conclusion that the higher surface temperature should be due to an increased heat flux of the fuel rich flame compared to the lean flame. This stems from the partial reaction to carbon monoxide, which is also exothermal, and due to this leads to a higher reaction enthalpy per mass flux.

The lowest surface temperatures are observed for the lean methane flame. The surface temperature on the flame side was used to choose the boundary condition in modeling. Since the exact surface temperature only slightly influenced the calculated heat flux, surface temperatures of either 350K or 390K were used for modeling. The differences in the modeled heat fluxes between these two temperatures as boundary condition were below 2%, so additional calculations seemed not to be needed.

Figure 6.3 compares the measured temperatures for the three distances investigated experimentally. The temperatures on both sides are highest for the small distance, while the differences between the three distances get smaller with mass flux. This is due to the fact that with increasing mass flux the boundary layer thickness is reduced and the stagnation point is shifted towards the plate, while the temperature difference between the plate and the maximum flame temperature is only affected slightly. The reduction of the slope of the temperature vs. mass flux curve is most pronounced for the flame at a distance of 15 mm and smaller for the distances of 30 and 60 mm. These temperatures are used in the following for the heat flux evaluation.

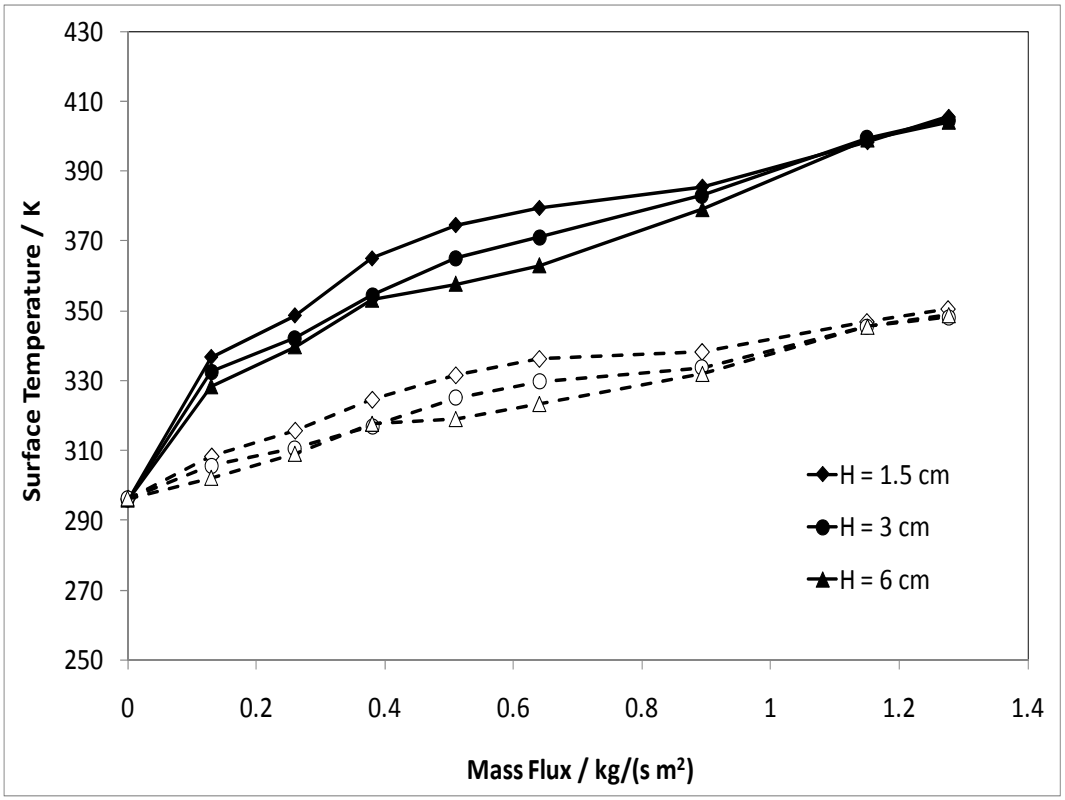

Figure 6-3 Surface temperature for three burner to plate distances
(solid symbols: heated side, hollow symbols: cooled side)

6.1.2 The stagnation heat fluxes

Based on the measured temperatures on both sides of the ceramic plate the heat fluxes were calculated. Figure 6.4 shows the experimental heat fluxes calculated for the stoichiometric methane flame at three different burner to plate distances. Also the modeling results for 15 and 30 mm are included. The experimental heat fluxes were calculated by using the average thermal conductivity of Al_2O_3 of the two ceramic plate sides. Since the absolute values of the published thermal conductivity of α - alumina was found to vary by about 40% [96], this could be a main contribution to the absolute errors.

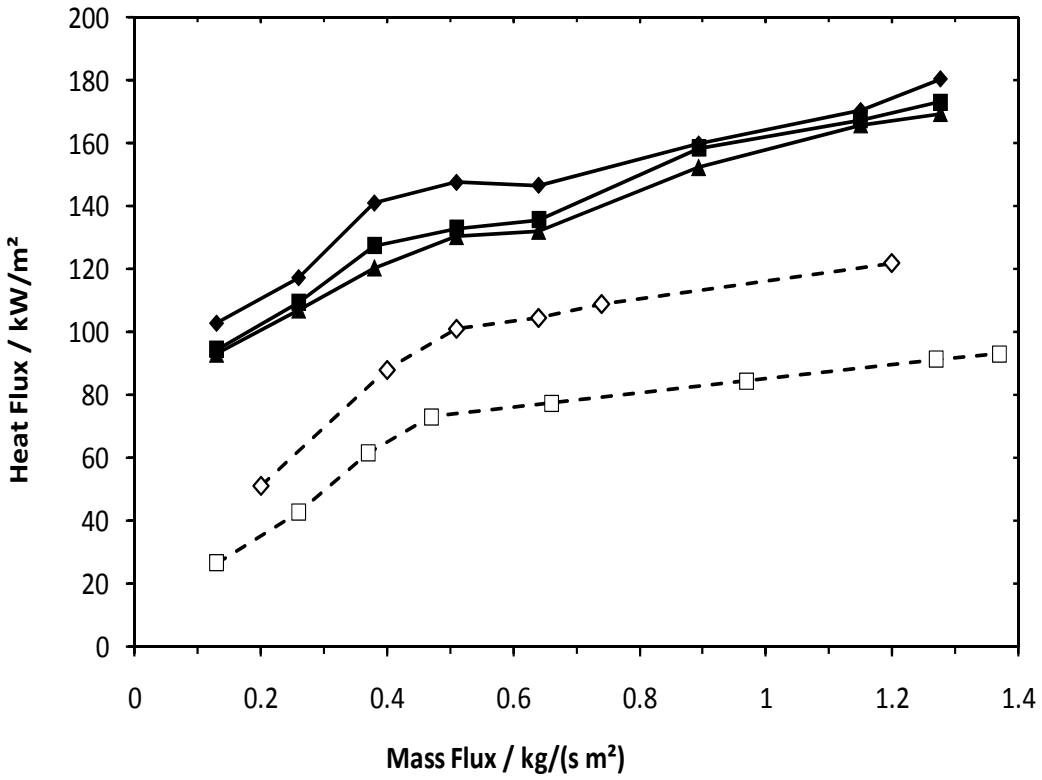

Figure 6-4 Stagnation point heat fluxes for stoichiometric flames at various burner to plate distances, comparison of measurement and model (solid symbol: measurement, hollow symbol: model; diamonds: H = 15 mm, squares: H = 30 mm, triangles: H = 6 mm)

All experiments were repeated several times (3-5), so the statistical errors for the differences were calculated. This relative error is larger in the lower temperature regime, because the temperature difference itself is smaller and also because the

temperature dependence of the ruby decay time is lower in the low temperature regime and gets larger with increasing temperature. The experimentally determined heat fluxes vary between 93 and 180 kW/m^2 and show a slight change in slope at mass fluxes around 0.5 kg/(m^2 s).

The heat flux for the smallest distance is highest, while it is slightly lower for the other two larger distances between burner and stagnation plate. The small change of the heat flux with the mass flux mainly shows that the increased gas flow leads not to an increase in the temperature gradient near the surface but to an increased flow of high enthalpy gases in the horizontal direction. In heating, this would be regarded as losses.

The modeled heat fluxes are throughout lower, while the relative discrepancy is larger at low mass fluxes. However, also in the modeled heat fluxes a change in slope is observed at mass fluxes of around 0.5 kg/(m^2 s), where convergence of the simulation was also more time consuming. This change can be easily understood in terms of flame stabilization mechanisms. At low mass fluxes the cold gas velocity is below the free flame velocity of 0.47 m/s for a stoichiometric methane air flame, leading to a burner stabilized flame.

Above this value the flame is stabilized due to the reduced flow velocities in the vicinity of the stagnation plate. The reason for the higher experimental heat flux values in not resolved yet. A part of the discrepancy could be explained by the experimental uncertainties, but it cannot be ruled out that the boundary conditions are deviating from the ones used in modeling, where a one-dimensional flow through a non-reacting surface is assumed.

This is further seen in the model. Calculated temperature and OH profiles for the stoichiometric flame with the stagnation plate at 15 mm distance from the burner are shown in Figure 6.5. The temperatures rise steeply adjacent to the burner for the low mass fluxes, indicating heat losses to the burner. Due to these heat losses, the maximum temperature in the flame is lowest for the lowest mass flux and increasing until the flame starts to detach from the burner. With further increasing mass flux the

high temperature zone gets narrower and is shifted further towards the stagnation surface.

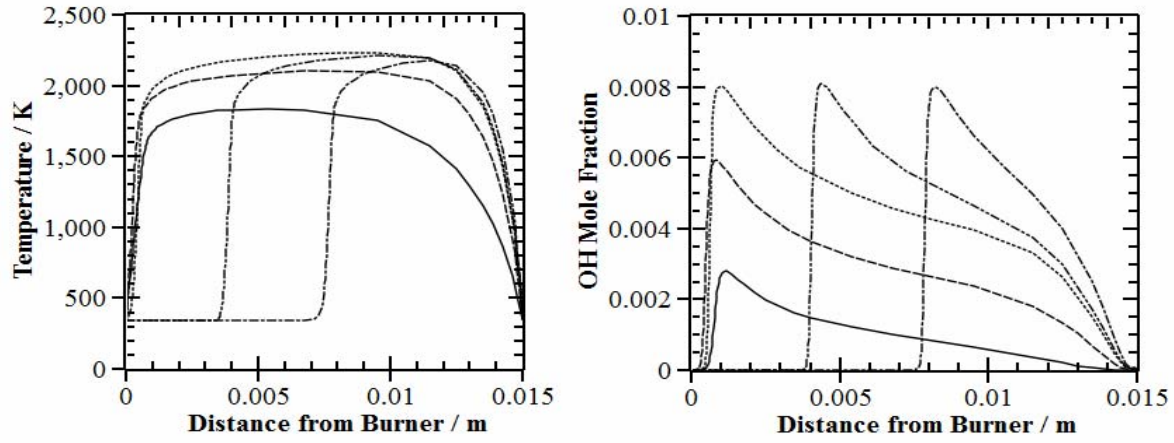

Figure 6-5 Effect of mixture cold gas velocity on flame temperature and OH concentration profiles (stoichiometric flame) (— 0.1 kg/(m^2 s), - - 0.3 kg/(m^2 s), ··· 0.47 kg/(m^2 s), -··- 0.64 kg/(m^2 s), -·-· 1.2 kg/(m^2 s),)

The temperature gradients at the stagnation surface are increasing at first with increasing mass flux until eventually the differences for the plate stabilized flames get relatively small. Similar trends are also seen for OH, which was also plotted as one important flame intermediate, and which was also used for flame temperature determination. The modeled maximum OH mole fraction first increases by more than a factor of three for the investigated velocity range and then remains constant if the flame is no longer burner stabilized. It is recognized that the OH mole fraction in the vicinity of the stagnation plate is negligible, which makes measurements of the temperature gradient in the gas phase using OH LIF challenging.

The variation of the distance between the burner and the stagnation plate was also investigated by modeling. Some results are compared in Fig. 6.6. For distances of 15 and 30 mm, two mass fluxes are compared: 0.1 and 1.2 kg/(m^2 s). For the slow mass flux, the initial temperature and OH profiles match well, while the temperature gradient next to the plate is smaller for the larger distance. For the large distance, the temperature rise again appears to be similar for both distances, but strongly shifted in

space. Again the temperature decay was steeper for the small distance, resulting in a larger heat flux. The findings for OH are similar.

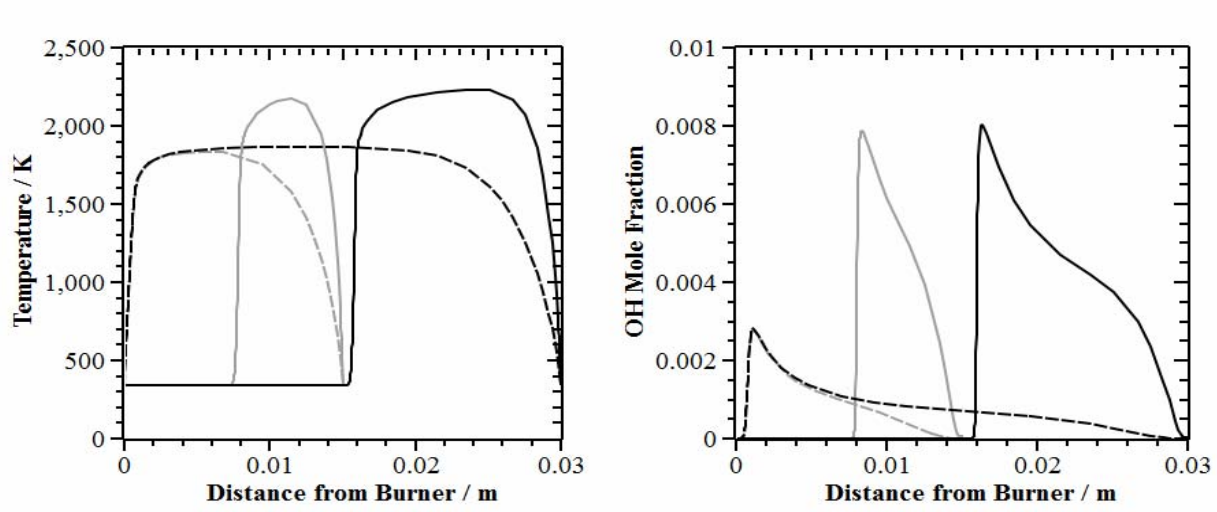

Figure 6-6 Effect of burner-to-plate distance on the flame temperature and OH concentration profiles. (black: 30 mm distance, grey: 15 mm distance; solid line: 1.2 kg/(m^2 s) mass flux, dashed: 0.1 kg/(m^2 s), mass flux)

Stoichiometry was varied at a fixed distance of 15 mm in the next series of experiments. The heat fluxes as a function of mass flux are shown for three stoichiometries in Figure 6.7. Again it can be seen that the experimental results are higher than the modeled ones, although the tendencies are similar, mainly for the high mass fluxes. The difference between the stoichiometric and the rich flame is much smaller, than the difference between the stoichiometric and the lean flame.

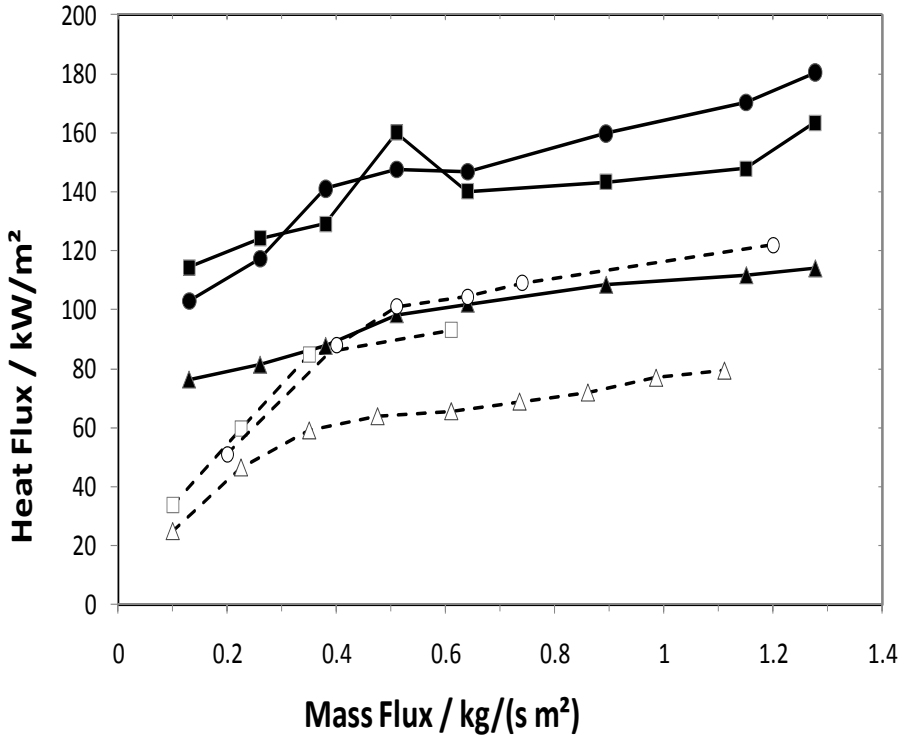

Figure 6-7 Stagnation point heat fluxes (H = 15 mm) for various equivalence ratios, comparison of measurement and model (solid symbol: measurement, hollow symbol: model; triangles: $\varphi = 0.75$, circles: $\varphi = 1$, squares: $\varphi = 1.25$)

However, due to the experimental uncertainties all differences below 15% should not be considered as significant. The trend of higher heat flux in the richer flames, as observed above, can also be nicely seen in the modeled temperature and OH profiles (Figure 6.8). These are shown for one low and one high mass flux, for the three selected stoichiometries. For the low mass flux all three flames are burner stabilized. The gradient for the stoichiometric flame is highest at the burner leading to the highest heat loss for this flame, which leads to similar maximum temperature for the stoichiometric and rich flame, although the adiabatic flame temperature is higher for the stoichiometric one. This is approximately reached at the high velocity.

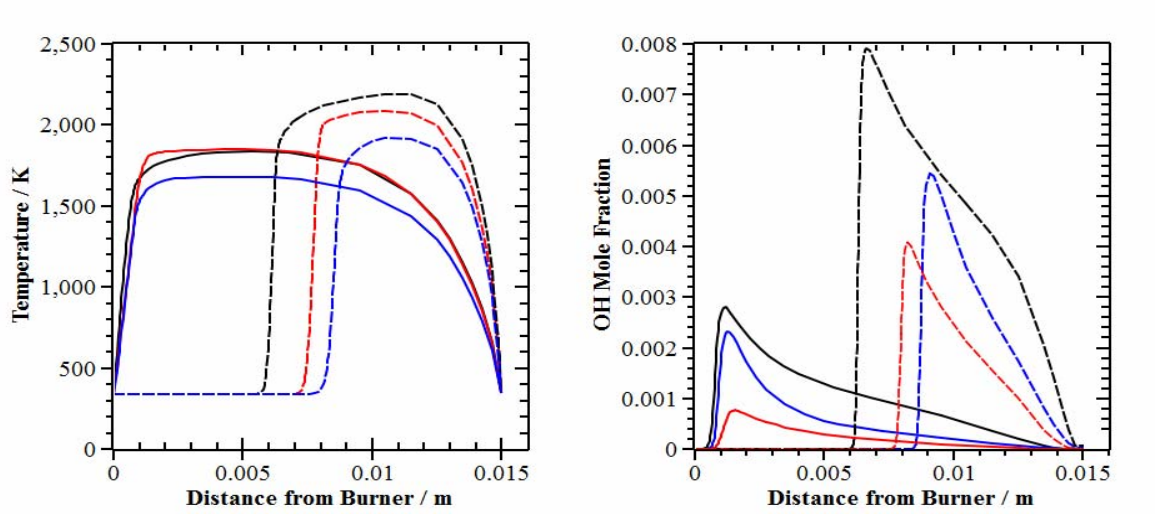

Figure 6-8 Effect of stoichiometry and mixture velocity on the flame temperature and OH concentration profiles (blue: lean mixture, black: stoichiometric mixture, red: rich mixture; lines: 0.1 kg/(m^2 s), dashed: 0.9 kg/(m^2 s))

Regarding the temperature gradients at the stagnation surface, it is seen that they are nearly identical for the low flux rich and stoichiometric flames, while it is smaller for the fuel lean flame. For the high mass flux the differences are getting larger and the differences in the adiabatic flame temperatures also scale approximately with the heat fluxes. As expected, the OH mole fractions are not only depending on temperature, but also on stoichiometry. The OH mole fractions rise strongly with temperature, but are thus lowest in the fuel rich flame.

Overall, these results show that intrinsic mechanisms of flame stabilization are most important for the heat flux from flames to walls. Generally convective heat transfer is discussed in terms of relations between the Nusselt number and the Reynolds number. The first being a measure of the dimensionless temperature gradient at the surface, while the latter compares the inertia forces with the viscous forces.

However, regarding the modeling results, the slope of the heat flux rate vs. the mass flux is mainly determined by its relation to the mass flux of a free flame. If the mass flux rate leads to a linear flow velocity below the laminar flame speed, the flame

is burner stabilized. In this regime the heat transfer is strongly influenced by the mass flow rate; the reason for this is the large heat flux to the burner. While at higher flow rates the slope of the heat flux with mass flow is much lower, because the velocity only slightly reduces the thickness of the boundary layer leading to a larger mass flux in the radial direction, but only weakly influencing the heat transfer rate to the plate. Surely this will change, if flame quenching starts at even higher flow rates. Thus, instead of the most often used Reynold's number, the cold gas velocity relative to the free flame speed may be a more useful independent dimensionless parameter in the studies of heat transfer from flames.

6.1.3 Flame temperature measurement

In order to prove the model predictions for some flames the gas phase temperatures of the stoichiometric flame with a distance of 15 mm were measured by S.Staude(Salem et al.[83]. Figure 6.9 shows the maximum flame temperatures that were obtained using OH-LIF for four different stoichiometric flames as a function of cold gas velocity, compared to the modeled results.

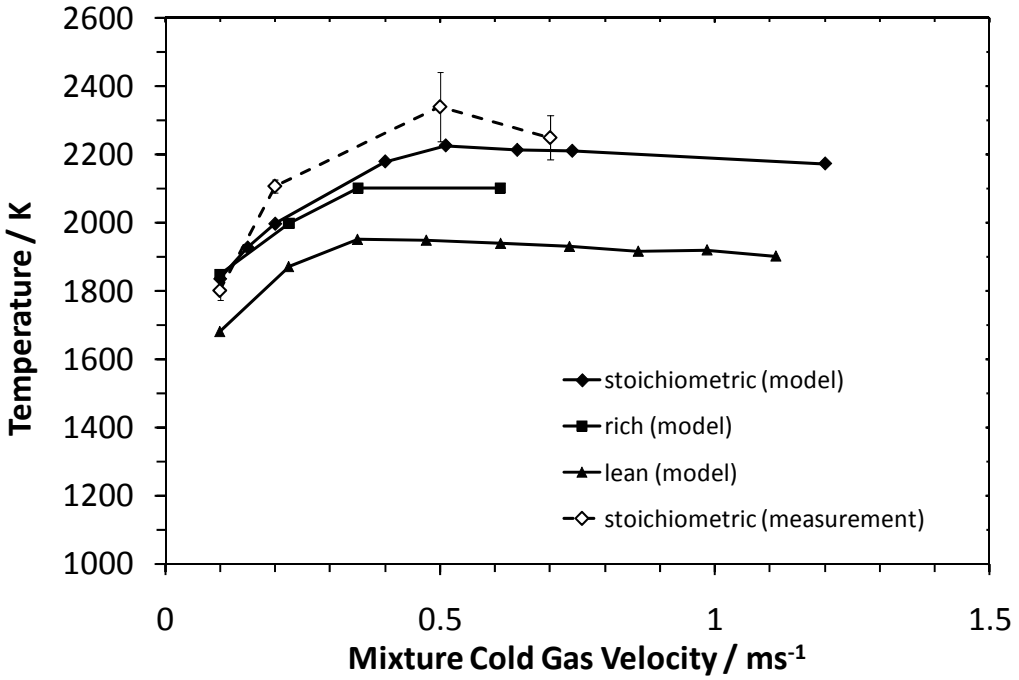

Figure 6-9 Maximum flame temperature as a function of mixture velocity. Comparison of model and measurement results

Initially, the flame temperature rises with increasing cold gas velocity. This is expected since the slower flames have a higher rate of heat transfer to the burner matrix. As the cold gas velocity increases to beyond the flame velocity, the flame is no longer burner stabilized, and the heat transfer to the burner becomes minimal. The measured temperatures coincide well within the experimental statistical uncertainties with the modeling results.

Initially, it was also aimed to measure temperature gradients in the gas phase in order to evaluate the heat flux independently also from the gas phase. However, the temperature gradients at the plate could not be resolved for the investigated flames. This has a number of reasons. Firstly, the OH concentration rapidly drops with the temperature near the plate, resulting in a very poor signal from the OH-LIF. If the modeled OH signals are regarded this becomes apparent. Further, the optical setup, chosen to avoid the saturation of the optical OH transition, only allows a resolution of about half a millimeter. For temperature measurements a good signal to noise ratio is needed to resolve smaller lines, which is quite difficult in the most interesting spatial region, the final 0.5-1mm adjacent to the stagnation wall.

Both reasons together lead to a bias in the measured temperatures near the plate, since the main OH signal in the excitation volume probably stems from the region most far away from the plate, preventing the measurement of correct temperature gradients. However, the maximum temperatures are found to be present in a relatively large spatial region, the temperature profile being quite flat (not shown), as also predicted by the model (see Fig 6.7).

6.2 Hydrogen/Methane/air premixed flames

6.2.1 Surface temperature measurement

Figures 6.10 shows a typical phosphorescence signal from the water cooled side, while two typical phosphorescence signals for the flame side of the stagnation plate are shown in Fig. 6.11, as measured for the flame with 10% H_2 in the fuel and cold gas velocities of 0.1 and 0.5 m/s. The evaluated surface temperatures on the flame side from the decay times are 343 K and 376 K, respectively.

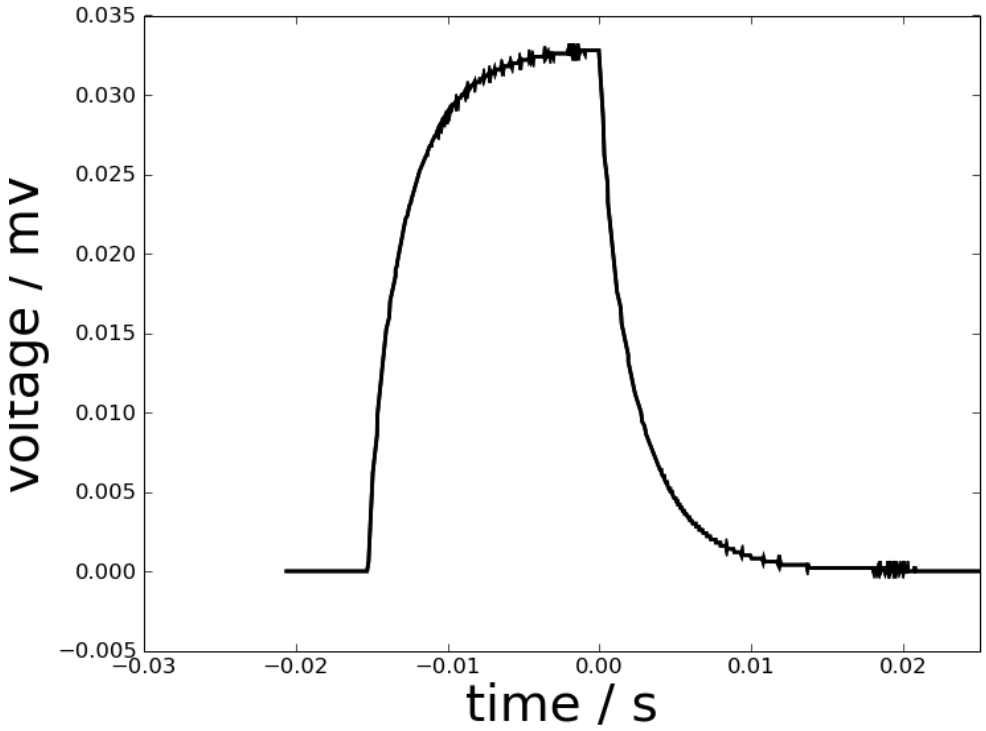

Figure 6-10 Phosphorescence signal from the cooled plate side using LED excitation.

It is seen that a very good signal to noise ratio is obtained. However, in this relatively low temperature range an important disadvantage of the used ruby phosphor is also seen. Although the difference in lifetime is easily recognized, it is seen that the decay time varies only slightly with temperature in this low temperature range. The same information can in principle be obtained from the calibration curve of the phosphor, which has a relatively small temperature dependence in the temperature

range between room temperature and 370K and which is getting steeper between 370 and 500K. The observed scatter on repeat measurements was between +/- 2K and +/-6 K, depending on the flame and temperature range.

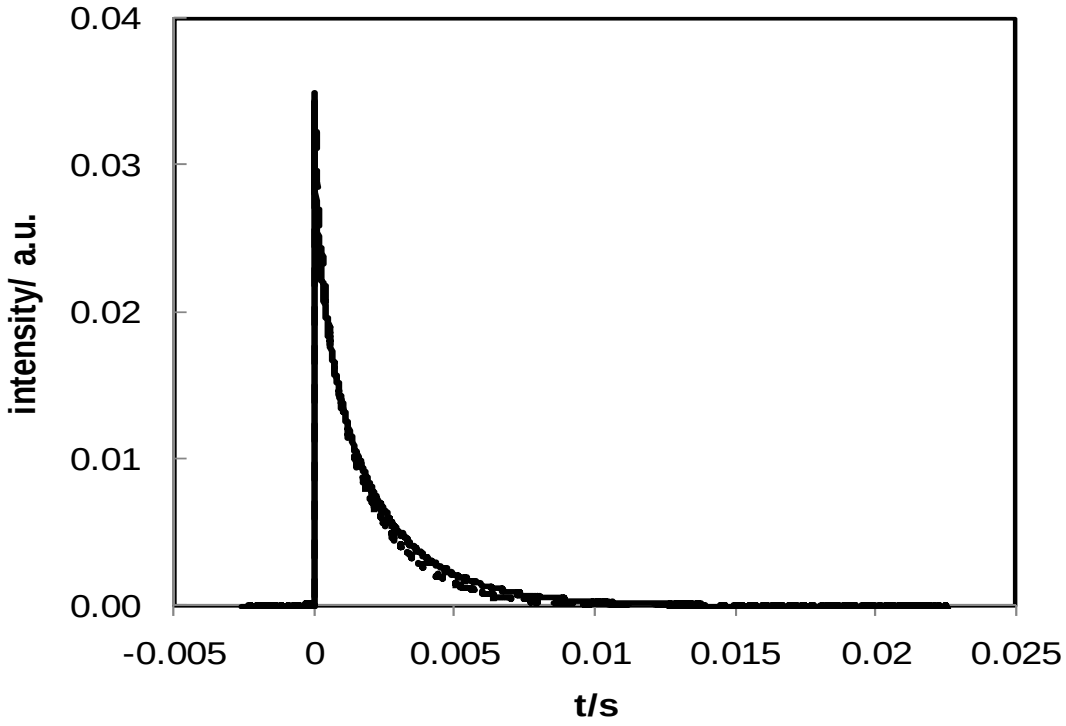

Figure 6-11 Typical phosphorescence signals after laser excitation for the flame heated plate side; both measured for the flame with 10% hydrogen in the fuel. The solid line was measured for a flow velocity of 0.1 m/s, the dotted line for 0.5 m/s.

Figure 6.12 shows the surface temperature measurement on the both sides of the ceramic plate for four different hydrogen/methane/air flames as a function of the total mass fluxes, all mixtures being stoichiometric. From the measured temperatures, only very small changes are recognized. The temperature levels rise with flow velocity, while the temperature difference between the flame heated front side and the water cooled back side also rises and remains in the order of 30-50 K. The temperature levels are only slightly affected by the fuel mixture. This indicate that only small effect on surface temperatures, due to the addition of hydrogen to the methane flames.

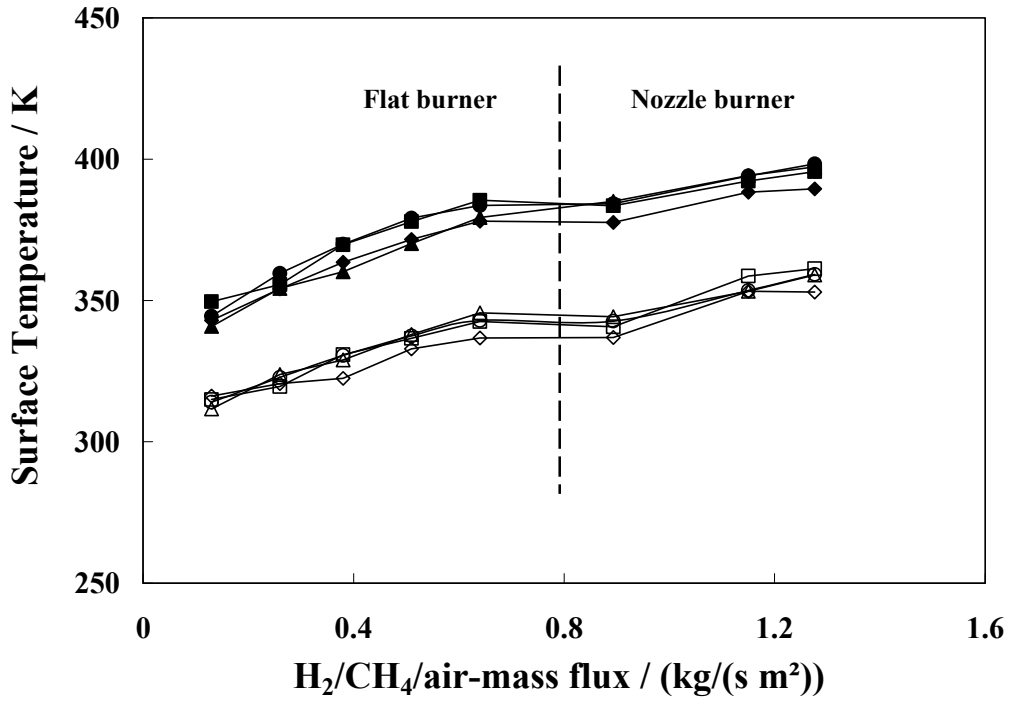

Figure 6-12 Surface temperatures measured for four different hydrogen-methane-fuel mixtures as a function of the mass flux. Triangles: 10% H_2, circles: 25% H_2, square: 50% H_2, diamonds: 75%H_2.

6.2.2 The stagnation heat fluxes

Based on the measured temperatures on both sides of the ceramic plate the heat flux density was calculated. Figure 5.13 shows the heat fluxes calculated for the four investigated stoichiometric hydrogen/methane flames. The heat fluxes were calculated using the average thermal conductivity of Al_2O_3 at the temperatures of the two ceramic plate sides. The value at room temperature of 22 W/(K m) was taken as provided by the supplier [96].

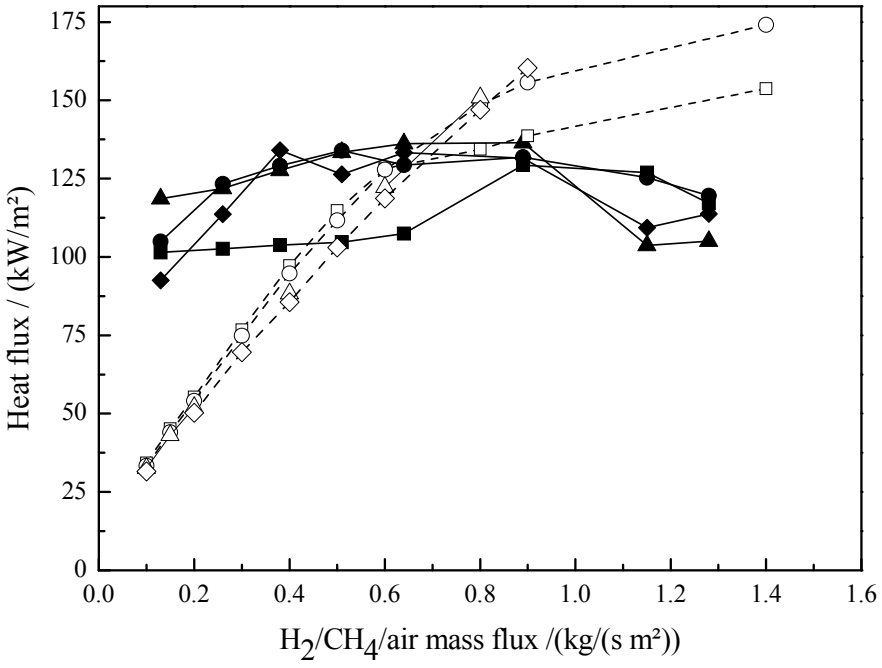

Figure 6-13 Measured (filled symbols) and calculated (open symbols) heat fluxes for four different fuel mixtures, as a function of mass flux rate. squares: 10% H_2, circles: 25% H_2, triangles: 50% H_2, diamonds: 75% H_2.

The heat fluxes for all four flames were quite similar if the experimental uncertainties are taken into account. The temperature difference of 30-50 K with uncertainties of +/-4 to +/-12 K results in uncertainties of 20-40%. Due to this, smaller deviations of the different curves will not be discussed. At the lowest flux of 0.13 kg/(m^2 s) the values range between 90 and 120 kW/m^2. The heat fluxes to the surface only vary slightly with the mass flux. As the burner setup is changed to the nozzle burner at mass fluxes above 0.64 kg/(m^2 s) for the flames with the higher flame speeds (25-75% H_2 content) the heat fluxes to the surface decrease. In these cases, the flame stabilizes in the tube and the assumption of a one-dimensional flame is no longer justified. The maximum experimentally observed heat fluxes are in the range of 130-140 kW/m^2. The modeling results are included in Figure 6.13. As can be seen, the model predicts only very small differences in the heat fluxes of the different

flames at the low to moderate mass fluxes. However, an important difference between the modeled heat fluxes and the experimentally determined ones is also seen. A much stronger mass flux dependence of the heat fluxes is predicted than determined experimentally. In this burner stabilized regime, the increase in heat flux mainly comes from the reduction of heat losses to the burner with increasing flow velocity. Due to this, the model also predicts increasing flame temperatures until the flow velocity equals the free flame speed. In order to prove this model prediction, the (maximum) flame temperatures were studied by OH LIF thermometry, as described in the following.

6.2.3 Flame temperature measurement

Figure 6.14 shows the temperatures that were obtained using OH-LIF by S.Staude(Salem et al), for four different flames as a function of the position in the flame. As can be seen, the flame temperature rises with increasing gas velocity from a maximum temperature of around 2000K at 0.1 m/s to 2460K at 0.5 m/s. This is expected since the slower flames have a higher rate of heat transfer to the burner matrix. By the same token, the temperature gradient as the plate is approached also increases with increasing velocity. In contrast, the increase in hydrogen in the mixture (from 25% to 50%) does not have a measurable effect on the flame temperature.

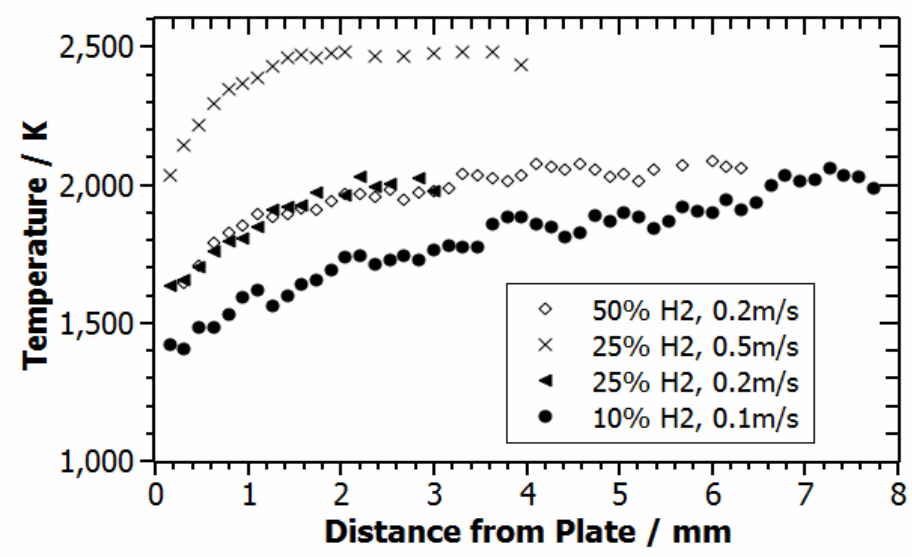

Figure 6-14 Flame temperature profiles obtained with OH-LIF

As mentioned previously in 5.1.3 the gradients could not be resolved for the investigated flames. Since the main OH signal in the excitation volume probably stems from the region most far away from the plate, preventing the measurement of correct temperature gradients. Especially the faster flames (higher cold gas velocity and/or higher concentration of hydrogen) have such steep gradients, where the temperature, according to modeling, drops from the maximum to the plate in less than a millimeter, that they could not be resolved here. However, the maximum temperatures are found to be present in a relatively large spatial range, so the measured maximum temperatures are shown in Fig. 6.15 as a function of cold gas velocity and compared to the modeled results.

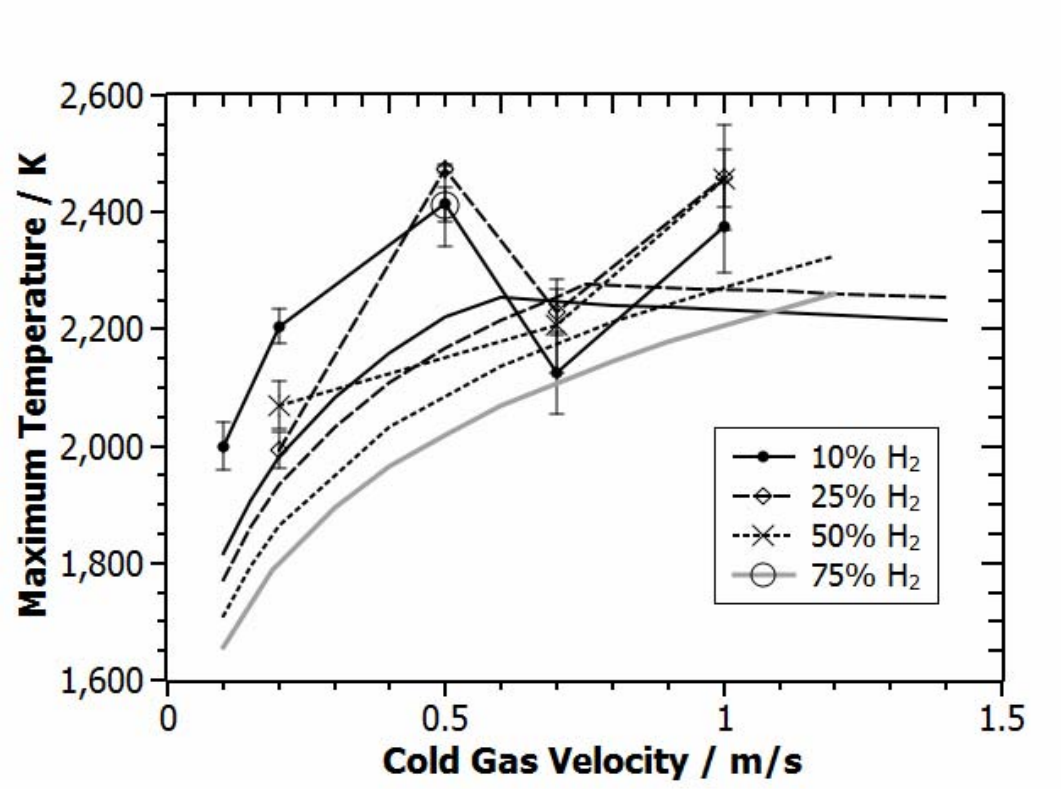

Figure 6-15 Maximum flame temperatures. Measured using OH-LIF (symbols with lines) and modelled (lines)

Firstly, it can be seen that the measured temperatures always lie a good 200 K above the simulated values. Only in the case of the 0.7 m/s flames can this trend not be observed. It is likely that here the heat transfer to the nozzle burner, which is not

included in the model and leads to horizontal heat losses, drastically reduces the actual flame temperature. Generally, the maximum temperature decreases as more hydrogen is added to the mixture. This is due to the fact that the hydrogen increases the free flame speed so that more heat is transferred to the burner at gas velocities below the free flame speed, thus reducing the maximum flame temperature. This trend changes at higher cold gas velocities.

The slower flames with 10-25% hydrogen would become stabilized on the plate at around 0.6 m/s flow velocity, shown by the kink in the modeled temperature profile. This effect can also be seen in the measurements at 1 m/s, where the 10% hydrogen flame is now around 100 K colder than the others. In the case of the 10% hydrogen flame, where most points have been measured, the modeled flame

temperature follows the measured profile very well.As can be seen from the error bars of the measured temperatures, there is considerable uncertainty in some of the measurement. This could be improved by increasing the averaging, as was done for the 25% hydrogen flame at 0.5 m/s, where averaging was increased from 16 pictures to 64 pictures, reducing the statistical variation in the temperature from ± 70 K to ±10 K. However, this value only accounts for the statistical variation and not for the total error.

6.2.4 Modeled OH mole fractions and temperatures

In Fig. 6.16, some selected temperature profiles and OH mole fraction profiles are shown from the model. All profiles are shown for the 10% H_2 flame. At a mass flux of 0.1 kg/(m^2 s) it is seen that the maximum temperature is lowest, and the temperature gradient at the stagnation surface at 15 mm is also the smallest, leading to the smallest predicted heat flux of 34 kW/ m^2. With increasing mass flux, the heat losses to the burner are reduced and the flame temperature approaches the adiabatic flame temperature. The OH mole fraction also increases with this trend. However, in direct vicinity of the surface the OH concentration is negligible.

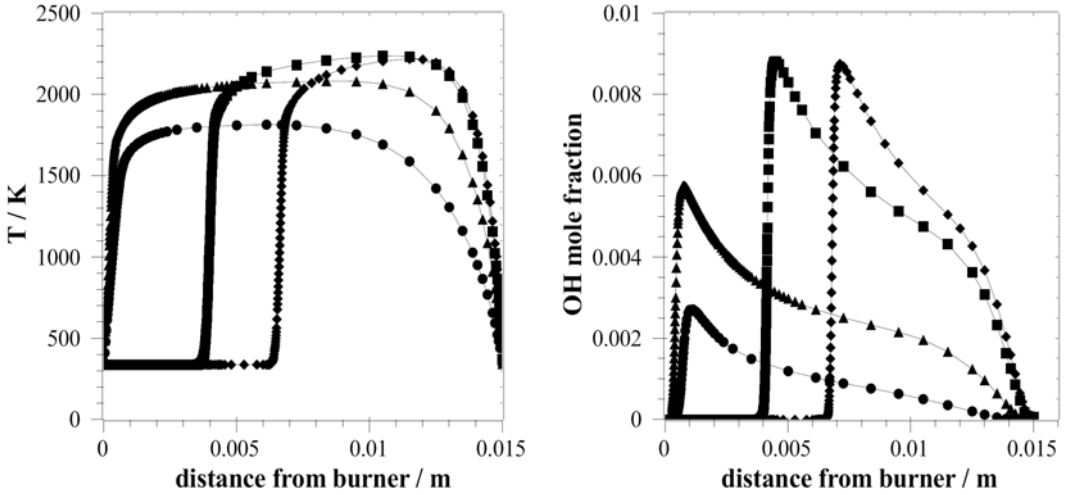

Figure 6-16 Modeled temperature and OH profiles for 10%H_2/CH_4 flames with four different mass fluxes (values in kg/(m^2 s)): circles: 0.1, triangles: 0.4, squares: 0.8, diamonds: 1.2.

For the two highest mass fluxes shown, the flow velocity is higher than the free flame speed and the flame is stabilized at the stagnation plate. The maximum temperatures are nearly the same and the temperature gradient near the surface only slightly depends on the mass flux, leading to similar heat fluxes of around 140 kW/m^2.

The question remains why the measured heat fluxes are so high at the low mass fluxes. The experimental errors are largest for these relatively low surface temperatures, which may be part of the problem. However, the discrepancy could also come from non-idealities in the flow. Although a standard porous plug burner was used, as is also used for many other flame studies, the measured heat flux could indicate that the flow is not really one dimensional in the direct vicinity of the burner, or additional effects like surface reactions at the burner might influence the total heat flux. This problem has to be resolved in future studies.

6.2.5 Surface temperature measurement using LED excitation on both sides of the plate

As mentioned previously in 4.1 the surface temperature was measured on both sides of the plate; the flame side and the cooling water side by using the green LED, as a light source for phosphorescence excitation and the heat fluxes were calculated. The investigated flames were stiochiometric hydrogen/methane/air flames with 10%, 20% hydrogen, and pure methane flame for lower fuel air mixture velocity (0.05-0.5 m/s) and burner to plate distance (15 mm). Figure 6.17 shows the surface temperatures on both sides of the ceramic plate for different hydrogen/methane/air

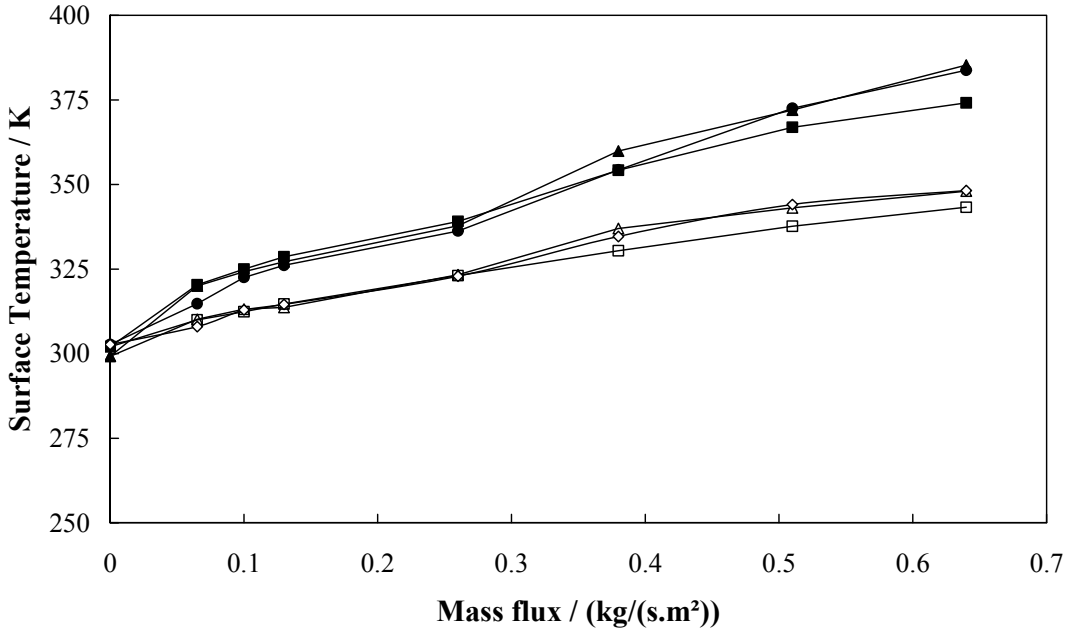

Figure 6-17 Surface temperature measured for different hydrogen-methane-fuel mixtures as a function of the mass flux (solid symbols: heated side, hollow symbols: cooled side; squares: 100 CH_4, triangles: 10% H_2, circles: 20% H_2)

flames as a function of total mass fluxes, all mixtures being stoichiometric. Only very small changed in temperatures were seen. The temperature increased with flow velocities.

Figure 6.17 shows the stagnation heat fluxes for pure methane/air flame compared with modeling. The measurement gave a very good agreement with, modeling results, which were slightly higher but the trend were the same.

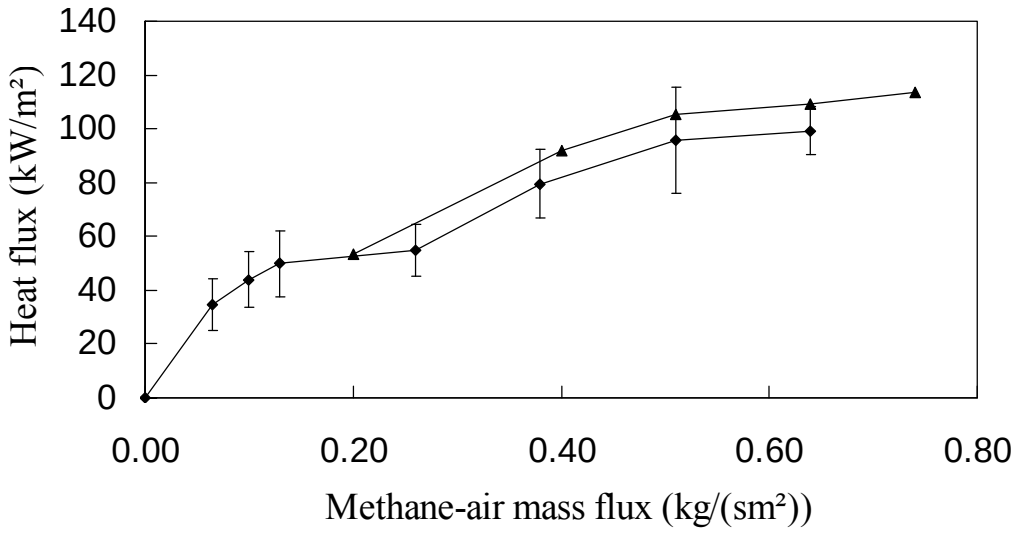

Figure 6-18 Stagnation heat flux for stoichiometric methane flame (H=15 mm), comparison of measurement and model. Diamonds: measurement, triangles: model.

The surface temperature measurements were repeated for methane flames with 10% and 20% of hydrogen in order to study the effect of the hydrogen addition on the heat fluxes. Figures 6.19 shows again, the comparison between the measurement and modeled heat fluxes for methane flame with 10% hydrogen, which shows a good agreement spatially at lower flow rates. Figure 6.20.shows the heat fluxed for different hydrogen contents. The heat fluxes for pure methane flame and methane flame with 10% are nearly the same. The heat fluxes increased with the flow rate and vary between 40 kW/m² at flow velocity 0.05 m/s to 100 kW/m² at flow velocity 0.5 m/s. For methane flame with 20% hydrogen the heat flux decreases, this maybe due to the heat losses to the burner.

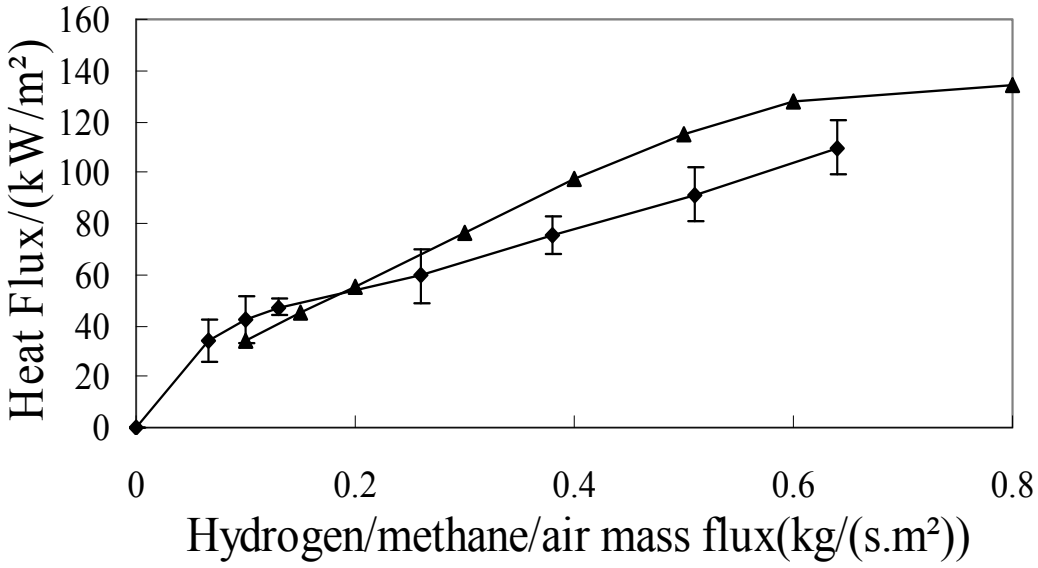

Figure **6-19** Stagnation heat flux for stoichiometric hydrogen-methane flame (10% H_2) and (H=15 mm), comparison of measurement and model. Diamonds: measurement, triangles: model.

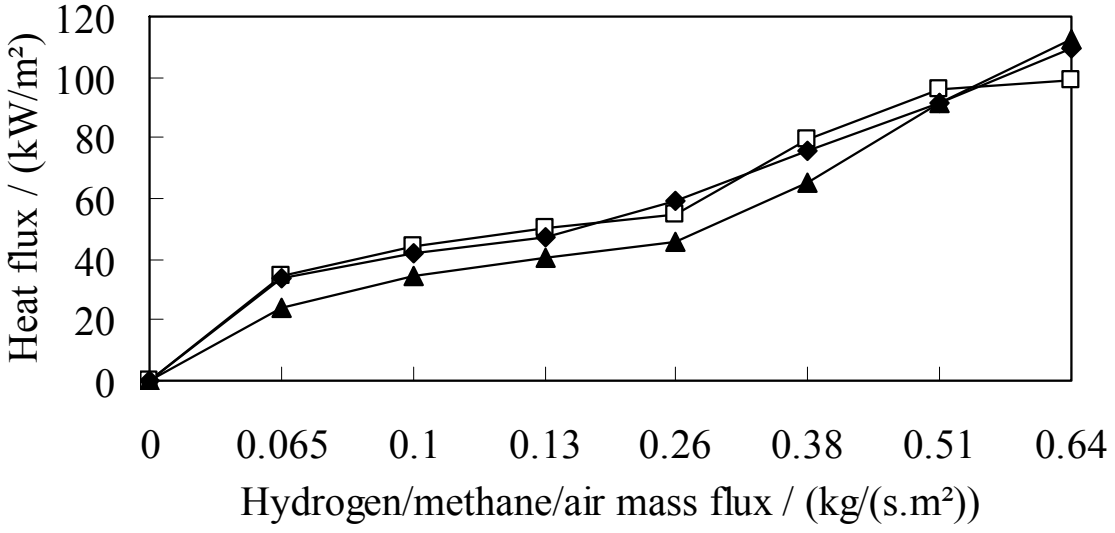

Figure 6-20 Stagnation point heat fluxes for stiochiometric flames for different fuel mixtures, as a function of mass flux rates (H=15 mm).Hollow squares:100% methane, diamonds: 10% H_2, triangles: 20% H_2.

Finally the findings of both measurement and model were compared with Kee correlation [51], which already mentioned in 2.4. Figure 6.21 shows comparison of the heat fluxes obtained. The figure shows clearly a difference between the heat fluxes calculated using two different sources of excitation on the flame side; the heat fluxes calculated by using laser excitation on the flame side were higher than the heat fluxes using LED excitation on the flame side. The heat fluxes calculated by using the LED on both side give a very good agreement to the model and Kee correlation findings. From the present results, it is seen that, using excitation LEDs on both sides is a better approach as compared to using a laser because it gives better results.

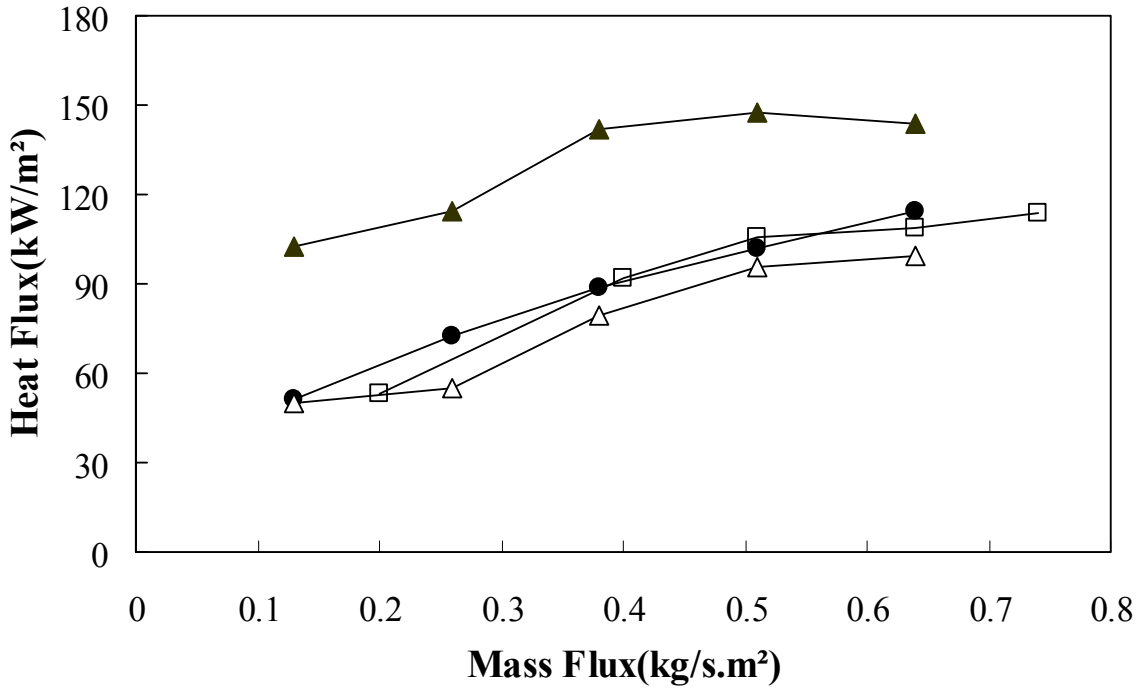

Figure 6-21 Stagnation point heat flux for stoichiometric methane, comparison of measurement, model, and Kee Correlation (solid triangles: using Laser excitation on flame side, hollow symbol: using LED excitation on both sides, hollow squares: model, solid circles: Kee Correlation)

CHAPTER SEVEN

SUMMARY AND CONCLUSIONS

7 Summary and Conclusions

A new experimental setup was designed to measure the surface temperatures and heat fluxes in stagnation flow flames, using phosphor thermometry. Methane-air flames with equivalence ratios of $\varphi=1$, $\varphi=0.75$ and $\varphi=1.25$ and stoichiometric hydrogen-methane-air flames (with 10%, 20%, 25%, 50% hydrogen content) were investigated at ambient pressure as a function of mass flux, stoichiometry and distance between burner and stagnation plate. The distances were chosen such, that a nearly one-dimensional flame was stabilized, which could also be modeled with detailed chemistry. Surface temperatures were measured using thermographic phosphors which were coated on both sides of an alumina plate. The phosphorescence was measured from both sides: the flame impingement and the water cooled side. From the surface temperatures also the local heat fluxes were determined, an important parameter which is not too often investigated. Thus the stagnation point heat flux for one dimensional methane-air flames and hydrogen-methane-air flames could be determined.

From these experimental results, two distinct regimes can be distinguished: At low flow rates the flame is burner stabilized. In this regime, an increase of the cold gas velocity does not only increase the total combustion enthalpy flux but also reduces the heat loss to the burner. This leads to an increased flame temperature. Since the boundary layer is also reduced with the fresh gas velocity, both effects lead to a strongly increasing heat flux. As soon as the fresh gas velocity exceeds above the flame speed, which is an intrinsic property of the gas mixture, the flame will be stabilized at the surface.

The adiabatic flame temperature will be reached if one does not approach flame quenching velocities. The heat flux continues to increase, but the rate of increase is reduced since the main effect now is a change in the boundary layer thickness. A large amount of high enthalpy gases are now transported convectively perpendicular to the surface and do not contribute to the heat transfer to the surface.

From the present results it is seen that, the flame speed is an important intrinsic factor, influencing the heat transfer from the flame. Due to this, the velocity relative to the flame speed seems to be a parameter in flame heat transfer at least as important as the Reynolds number.

Recent developments and applications demonstrate phosphor thermometry being very flexible and successful in measuring temperatures in many different applications areas ranging from gas turbine measurements, internal combustion engine piston and value measurements, pyrolysis studies, to supersonic and hypersonic wind tunnel experiments. In this study, the technique has also been extended to measure the surface temperatures and the local heat flux in stagnation point laminar premixed one dimensional flames.

All experiments were repeated several times (3-5), so the statistical errors for the differences were calculated. This relative error is larger in the lower temperature regime, because the temperature difference itself is smaller and also because the temperature dependence of the ruby decay time is lower in the low temperature regime and gets larger with increasing temperature. The experimentally determined heat fluxes vary between 93 and 180 kW/m^2 and show a slight change in slope at mass fluxes around 0.5 $kg/(m^2 s)$.

The uncertainty analysis was carried out using the method of Kline and McClintock [95]. The minimum and the maximum uncertainties in lifetime measurements were 0.2% and 2%. The minimum and the maximum uncertainties in surface temperature difference measurements were 3% and 7%.

As discussed previously in chapter 5, since the absolute values of the published thermal conductivity of α-alumina was found to vary by about 20%, we fear that this will be a main contribution to the absolute errors. The experimental temperature differences from which the heat fluxes are calculated, have estimated errors of +/-40% for the lower temperature range and +/-20% for the higher temperature range.

From OH-LIF measurement by Staude (Salem et al. [83]); it was see that temperature gradients near walls are difficult to be measure, since the concentration of OH rapidly falls. Some improvement of the spatial resolution will be possible, but other methods like NO-LIF or CARS spectroscopy [66] may be a better choice for temperature measurements near the wall. However, the NO levels predicted by the model are in the range of 20-130 ppm, which will make doping necessary in order to measure reliable temperatures.

The experimental geometry used in this study, may be well suited for further studies of the elementary flame wall interaction. Accompanied by modeling, this system is a good choice for fundamental heat transfer studies in reactive flows. Although the surface temperature measurements are quite accurate, So far, the experimental uncertainty is relatively large and the errors in the determined temperature gradients and therefore in the heat fluxes get relatively large. This can be reduced in the future studies by using plates with higher thermal resistances. In addition the experimental measurements show reasonable agreement with the modeling results.

In the current study, the green light emitting diodes (LEDs) was used as excitation source on both sides of the ceramic plate is a better approach as compared to using a laser, since the LEDs are much cheaper and easy to operate as compared to a laser. So it would be better if in the future LEDs could be used to carry out the experiments for higher flame velocities also. If good results are also obtained for the higher velocities then the use of LED will be a very good technique for surface temperature measurements. As a result the stagnation point heat fluxes can easily be evaluated.

References

1. Cappelli, M.A. and P.H. Paul, An investigation of diamond film deposition in a premixed oxyacetylene flame. Journal of Applied Physics, 1990. 67(5): p. 2596-2602.
2. Branch, M.C., et al., Surface modification of polypropylene films by exposure to laminar, premixed methane-air flames. Symposium (International) on Combustion, 1998. 2: p. 2807-2813.
3. McCarty, K.F., et al., Scaleable stagnation-flow reactors for uniform materials deposition: Application to combustion synthesis of diamond. Applied Physics Letters, 1993. 63(11): p. 1498-1500.
4. Murayama, M., S. Kojima, and K. Uchida, Uniform deposition of diamond films using a flat flame stabilized in the stagnation-point flow. Journal of Applied Physics, 1991. 69(11): p. 7924-7926.
5. Goodwin, D.G., N.G. Glumac, and H.S. Shin, Diamond thin film deposition in low-pressure premixed flames. Symposium (International) on Combustion, 1996. 26(2): p. 1817-1824.
6. Milson, A. and N.A. Chigier, Studies of methane and methane-air flames impinging on a cold plate. Combustion and Flame, 1973. 21(3): p. 295-305.
7. Rigby, J.R. and B.W. Webb, An experimental investigation of diffusion flame jet impingement heat transfer. Proceedings of the ASME/JSME Thermal Engineering Joint Conference, 1995. 3: p. 117-126.
8. Dong, L.L., C.S. Cheung, and C.W. Leung, Heat transfer characteristics of an impinging butane/air flame jet of low Reynolds number. Experimental Heat Transfer, 2001. 14(4): p. 265-282.
9. Dong, L.L., C.S. Cheung, and C.W. Leung, Heat transfer from an impinging premixed butane/air slot flame jet. International Journal of Heat and Mass Transfer, 2002. 45(5): p. 979-992.
10. Kwok, L.C., C.W. Leung, and C.S. Cheung, Heat transfer characteristics of slot and round premixed impinging flame jets. Experimental Heat Transfer, 2003. 16(2): p. 111-137.
11. Chander, S. and A. Ray, An experimental and numerical study of stagnation point heat transfer for methane/air laminar flame impinging on a flat surface. International Journal of Heat and Mass Transfer, 2008. 51(13-14): p. 3595-3607.
12. Viskanta, R., Heat transfer to impinging isothermal gas and flame jets. Experimental Thermal and Fluid Science, 1993. 6(2): p. 111-134.
13. Viskanta, R., Convective and radiative flame jet impingement heat transfer. Int. J. Transport Phenomena, 1998. 1: p. 1-15.
14. Chander, S. and A. Ray, Influence of burner geometry on heat transfer characteristics of methane/air flame impinging on flat surface. Experimental Heat Transfer, 2006. 19(1): p. 15-38.
15. Chander, S. and A. Ray, Flame impingement heat transfer: A review. Energy Conversion and Management, 2005. 46(18-19): p. 2803-2837.

16. Baukal Jr, C.E. and B. Gebhart, A review of empirical flame impingement heat transfer correlations. International Journal of Heat and Fluid Flow, 1996. 17(4): p. 386-396.
17. Sagot, B., et al., Jet impingement heat transfer on a flat plate at a constant wall temperature. International Journal of Thermal Sciences, 2008. 47(12): p. 1610-1619.
18. Baukal, C.E. and B. Gebhart, A review of flame impingement heat transfer studies .1. Experimental conditions. Combustion Science and Technology, 1995. 104(4-6): p. 339-357.
19. Remie, M.J., et al., Analysis of the heat transfer of an impinging laminar flame jet. International Journal of Heat and Mass Transfer, 2007. 50(13-14): p. 2816-2827.
20. Remie, M.J., et al., Flame jet properties of Bunsen-type flames. Combustion and Flame, 2006. 147(3): p. 163-170.
21. Kleijn, C.R., Heat transfer from laminar impinging methane air flames. Computational Technologies for Fluid/Thermal/Structural/Chemical Systems with Industrial Applications, 2005. 424 PVP: p. 259-269.
22. Poinsot, T., T. Echekki, and M.G. Mungal, A study of the laminar flame tip and implications for premixed turbulent combustion. Combustion Science and Technology, 1992. 81(1-3): p. 45-73.
23. Childs, P.R.N., J.R. Greenwood, and C.A. Long, Review of temperature measurement. Review of Scientific Instruments, 2000. 71(8): p. 2959-2978.
24. Wolfrum, J., Advanced laser spectroscopy in combustion chemistry: From elementary steps to practical devices. Faraday Discussions, 2001. 119: p. 1-26.
25. Kohse-Hoinghaus, K., et al. Combustion at the focus: Laser diagnostics and control. in Proceedings of the Combustion Institute. 2005.
26. Allison, S.W. and G.T. Gillies, Remote thermometry with thermographic phosphors: Instrumentation and applications. Review of Scientific Instruments, 1997. 68(7): p. 2615-2650.
27. Brübach, J., A. Dreizler, and J. Janicka, Gas compositional and pressure effects on thermographic phosphor thermometry. Measurement Science and Technology, 2007. 18(3): p. 764-770.
28. Brübach, J., et al., Determination of surface normal temperature gradients using thermographic phosphors and filtered Rayleigh scattering. Applied Physics B: Lasers and Optics, 2006. 84(3): p. 537-541.
29. Brübach, J., A. Patt, and A. Dreizler, Spray thermometry using thermographic phosphors. Applied Physics B: Lasers and Optics, 2006. 83(4): p. 499-502.
30. Atakan, B., C. Eckert, and C. Pflitsch, Light emitting diode excitation of Cr3+:Al2O 3 as thermographic phosphor: Experiments and measurement strategy. Measurement Science and Technology, 2009. 20(7).
31. Hartlieb, A.T., B. Atakan, and K. Kohse-Hoinghaus, Temperature measurement in fuel-rich non-sooting low-pressure hydrocarbon flames. Applied Physics B-Lasers and Optics, 2000. 70(3): p. 435-445.
32. Tian, K., et al., Influence of ferrocene addition to a laminar premixed propene flame: Laser diagnostics, mass spectrometry and numerical simulations. Proceedings of the Combustion Institute, 2009. 32: p. 445-452.

33. Halter, F., C. Chauveau, and I. Gökalp, Characterization of the effects of hydrogen addition in premixed methane/air flames. International Journal of Hydrogen Energy, 2007. 32(13): p. 2585-2592.
34. Halter, F., et al. Characterization of the effects of pressure and hydrogen concentration on laminar burning velocities of methane-hydrogen-air mixtures. in Proceedings of the Combustion Institute. 2005.
35. Halter, I.F., et al. Characterization of the effects of pressure and hydrogen concentration on laminar burning velocities of methane-hydrogen-air mixtures. in International Symposium on Combustion, Abstracts of Accepted Papers. 2004.
36. Hu, E., et al., Experimental and numerical study on laminar burning characteristics of premixed methane-hydrogen-air flames. International Journal of Hydrogen Energy, 2009. 34(11): p. 4876-4888.
37. Zhang, Y., J. Wu, and S. Ishizuka, Hydrogen addition effect on laminar burning velocity, flame temperature and flame stability of a planar and a curved CH4-H2-air premixed flame. International Journal of Hydrogen Energy, 2009. 34(1): p. 519-527.
38. Johnson, R.W., The handbook of fluid dynamics. 1998: Springer.
39. Gaydon, A.G. and H.G. Wolfhard, Flames: Their Structure. Radiation and Temperature, 1979.
40. El-Mahallawy, F. and S.E.D. Habik, Fundamentals and technology of combustion. 2002: Elsevier.
41. Barnard, J.A. and J.N. Bradley, Flame and combustion. 1985: Chapman and Hall New York.
42. Kuo, K.K., Principles of combustion. 1986: Wiley New York et al.
43. Glassman, I., Combustion. 1996: Academic Pr.
44. Williams, F.A., Combustion theory. 1965: Citeseer.
45. Griffiths, J.F. and J.A. Barnard, Flame and combustion. 1995: CRC.
46. Turns, S.R., An introduction to combustion. 1996: McGraw-Hill New York.
47. Warnatz, J., U. Maas, and R.W. Dibble, Combustion: physical and chemical fundamentals, modeling and simulation, experiments, pollutant formation. 2006: Springer Verlag.
48. Fristrom, R.M. and A.A. Westenberg, Flame structure. 1965: McGraw-Hill.
49. Laidler, K.J., A glossary of terms used in chemical kinetics, including reaction dynamics. Pure and Applied Chemistry, 1996. 68(1): p. 149-192.
50. Vandermeer, T.H., Stagnation point heat transfer from turbulent low Reynolds number jets and flame jets. Experimental Thermal and Fluid Science, 1991. 4(1): p. 115-126.
51. Kee, R.J., M.E. Coltrin, and P. Glarborg, Chemically reacting flow. 2003: Wiley-Interscience Hoboken, NJ.
52. Polat, S., et al., Numerical flow and heat transfer under impinging jets: A review. Annual Review of Numerical Fluid Mechanics and Heat Transfer, 1989. 2: p. 157-197.
53. Baukal, C.E., et al., Heat transfer mechanisms in flame impingement heating. Proc. Int. Gas Res. Conf., 1996. 2(2): p. 2277-2287.
54. Baukal, C.E., Heat transfer in industrial combustion. 2000: CRC.

55. Baukal, C., E. and Gebhart, B. A Review of Semi-analytical Solutions for Flame Impingement. Int. J. Heat and Mass Transfer, 1996, 39(4), 2006.
56. Hargrave, G.K., M. Fairweather, and J.K. Kilham, Forced convective heat transfer from premixed flames .2. inpingement heat transfer. International Journal of Heat and Fluid Flow, 1987. 8(2): p. 132-138.
57. Mizuno, K., R. Mital, and R. Viskanta, An experimental study of premixed flame impingement heat transfer. American Society of Mechanical Engineers, Heat Transfer Division, (Publication) HTD, 1996. 335: p. 245-252.
58. Beer , J.M. and N.A. Chigier, Impinging jet flames. Combustion and Flame, 1968. 12(6): p. 575-586.
59. Jackson, E.G. and J.K. Kilham, Heat transfer from combustion products by forced convection. Ind. Eng. Chem., 1956. 48(11): p. 2077-2079.
60. Cremers, M.F.G., et al., Thermochemical heat release of laminar stagnation flames of fuel and oxygen. International Journal of Heat and Mass Transfer, 2010. 53(5-6): p. 952-961.
61. Giedt, W.H., L.L. Cobb, and E.J. Russ, Effect of hydrogen recombination on turbulent flow heat transfer. ASME Paper, 1960.
62. Siegel, R. and J.R. Howell, Thermal radiation heat transfer. 2002: Taylor & Francis.
63. Modest, M.F., Radiative heat transfer. 2003: Academic Pr.
64. Ivernel, A. and P. Vernotte, Experimental Study on Improvement of Convective Heat Transfer Rates in Furnaces by Oxygen Injection. ETUDE EXPERIMENTALE DE L'AMELIORATION DES TRANSFERTS CONVECTIFS DANS LES FOUR PAR SUROXYGENATION DU COMBURANT., 1979. 18(210-211): p. 375-391.
65. Popiel, C.O., T.H. van der Meer, and C.J. Hoogendoorn, Convective heat transfer on a plate in an impinging round hot gas jet of low Reynolds number. International Journal of Heat and Mass Transfer, 1980. 23(8): p. 1055-1067.
66. Brübach, J., et al., Simultaneous phosphor and CARS thermometry at the wall-gas interface within a combustor. Proceedings of the Combustion Institute, 2009. 32: p. 855-861.
67. Urban, G., et al., High-resolution thin-film temperature sensor arrays for medical applications. Sensors and Actuators A: Physical, 1989. 22(1-3): p. 650-654.
68. Turner, R.C., et al., Materials for high temperature acoustic and vibration sensors: A review. Applied Acoustics, 1994. 41(4): p. 299-324.
69. Alaruri, S., et al., Mapping the surface temperature of ceramic and superalloy turbine engine components using laser-induced fluorescence of thermographic phosphor. Optics and Lasers in Engineering, 1999. 31(5): p. 345-351.
70. Vander Wal, R.L., P.A. Householder, and T.W. Wright, Phosphor thermometry in combustion applications. Applied Spectroscopy, 1999. 53(10): p. 1251-1258.
71. Feist, J.P., et al. Phosphor thermometry for high temperature gas turbine applications. in ICIASF Record, International Congress on Instrumentation in Aerospace Simulation Facilities. 1999.

72. Pflitsch, C., D. Viefhaus, and B. Atakan, CVD of thin ruby films on Si(100) and stainless steel for surface temperature sensor applications. Chemical Vapor Deposition, 2007. 13(8): p. 420-426.
73. Eckert, C., C. Pflitsch, and B. Atakan. Dy3+:Al2O3 and (Dy3++Cr 3+): Al2O3 films for temperature sensor applications derived by thermal cvd and sol-gel techniques. in ECS Transactions. 2009.
74. Nebatti, A., et al., Sol-gel-deposition of thin TiO2:Eu3+ thermographic phosphor films. Progress in Organic Coatings, 2010. 67(3): p. 356-360.
75. Eckert, C., C. Pflitsch, and B. Atakan, Sol-gel deposition of multiply doped thermographic phosphor coatings Al2O3:(Cr3+, M3+) (M = Dy, Tm) for wide range surface temperature measurement application. Progress in Organic Coatings, 2010. 67(2): p. 116-119.
76. Tobin, K.W., et al., High-temperature phosphor thermometry of rotating turbine blades. AIAA journal, 1990. 28(8): p. 1485-1490.
77. Vander Wal, R.L., P.A. Householder, and T.W. Wright Ii, Phosphor thermometry in combustion applications. Applied Spectroscopy, 1999. 53(10): p. 1251-1258.
78. Brübach, J., et al., Determination of surface normal temperature gradients using thermographic phosphors and filtered Rayleigh scattering. Applied Physics B: Lasers and Optics, 2006. 84(3): p. 537-541.
79. Seyfried, H., et al., Laser-induced phosphorescence for surface thermometry in the afterburner of an aircraft engine. AIAA Journal, 2007. 45(12): p. 2966-2971.
80. Lakowicz, J.R. and B.R. Masters, Principles of fluorescence spectroscopy. Journal of Biomedical Optics, 2008. 13: p. 029901.
81. Skoog, D.A., F.J. Holler, and T.A. Nieman, Principles of instrumental analysis. 1985.
82. Shionoya, S., H. Yamamoto, and W.M. Yen, Phosphor handbook. 1999: CRC press New York.
83. Salem, M., et al., Heat flux measurements in stagnation point methane/air flames with thermographic phosphors. Experiments in Fluids, 2010: p. 1-11.
84. Pflitsch, C., R.A. Siddiqui, and B. Atakan, Phosphorescence properties of sol-gel derived ruby measured as functions of temperature and Cr3+ content. Applied Physics A: Materials Science and Processing, 2008. 90(3): p. 527-532.
85. Brübach, J., J. Janicka, and A. Dreizler, An algorithm for the characterisation of multi-exponential decay curves. Optics and Lasers in Engineering, 2009. 47(1): p. 75-79.
86. Seat, H.C. and J.H. Sharp, Dedicated temperature sensing with C-axis oriented single crystal ruby (Cr3+ Al2O3) fibers: Temperature and strain dependences of R-line fluorescence. IEEE Transactions on Instrumentation and Measurement, 2004. 53(1): p. 140-154.
87. Kohse-Höinghaus, K., Laser techniques for the quantitative detection of reactive intermediates in combustion systems. Progress in Energy and Combustion Science, 1994. 20(3): p. 203-279.
88. Kohse-Höinghaus, K. and J.B. Jeffries, Applied combustion diagnostics. 2002: CRC.

89. Crosley, D.R., Laser-induced fluorescence in spectroscopy, dynamics, and diagnostics. Journal of Chemical Education, 1982. 59(6): p. 446-455.
90. Atakan, B., J. Heinze, and U.E. Meier, OH laser-induced fluorescence at high pressures: Spectroscopic and two-dimensional measurements exciting the A-X (1,0) transition. Applied Physics B-Lasers and Optics, 1997. 64(5): p. 585-591.
91. Goodwin, D.G., An open-source, extensible software suite for CVD process simulation. Chemical Vapor Deposition XVI and EUROCVD, 2003. 14: p. 2003-08.
92. Taylor, J.R., An introduction to error analysis. 1982: University Science Books Mill Valley, CA.
93. Moffat, R.J., Describing the uncertainties in experimental results. Experimental Thermal and Fluid Science, 1988. 1(1): p. 3-17.
94. Hemrick, J.G., et al., Thermal conductivity of alumina measured with three techniques. Journal of Testing and Evaluation, 2003. 31(5): p. 438-442.
95. Kline, S.J. and F.A. McClintock, Describing uncertainties in single sample experiments. Mech. Eng., 1970. 75: p. 359-371.
96. Hemrick, J.G., et al., Thermal conductivity of alumina measured with Three techniques. Journal of testing and evaluation, 2003. 31(5): p. 438-442.

Curriculum Vitae

Personal Data

Name: Mohamed Salem Elmnefi

Sex: Male

Date of Birth: 16 February 1964

Place of Birth: Benghazi, Libya

Marital Status: Married

Nationality: Libyan

Language: Arabic, English and German

E-mail: mohamed.salem@uni-due.de

ACADEMIC QUALIFICATIONS

2007-2010: Ph.D. student, Chair of Thermodynamics, Institute of Combustion and Gas Dynamics, Department of Mechanical Engineering , Faculty of Engineering, University Duisburg-Essen, Duisburg-Germany.

1994-1996: M.Sc. Degree, Mechanical Engineering specializing in Thermodynamics and Fluid Mechanics, Energy Systems Division, Faculty of Engineering, University of Strathclyde, Glasgow, Scotland, U .K .

Thesis title: **"**Comparison of Two-Phase flow Characteristics of Valves and Orifices in a Large Diameter horizontal Pipeline "

1982-1986: B.Sc. Degree in Mechanical Engineering department, Faculty of Engineering, Bright Star University of Technology Brega, Libya.

Work Experience

1986-1987 : Mechanical Engineer in construction and maintenance department at COMME (Company of Mechanical and Electrical Engineering) in Benghazi-Libya The company specializing in maintenance and operation of steam and gas turbines, such as Benghazi North power station and Sousa power station.

1987-1994 : Mechanical Engineer in maintenance department in Sarir Oil Field in the Arabian Gulf Oil Company (AGOCO) responsible for the maintenance and operation of gas turbines including major overhauling and preventive maintenance.

1994-1996 : Study of M.Sc. Degree at the University of Strathclyde, Glasgow, Scotland, U.K.

1996-2000 : Project engineer in the department of engineering and construction in the Arabian Gulf Oil Company at Benghazi, supervising many new projects such as tie-ins of 8" oil and gas flow lines from the oil wells to the main oil pumping stations and installation of new storage tanks, oil separators, gas compressors, gas turbines and installation of fire fighting systems.

ACADEMIC EXPERIENCE

From 2000: Assistance Lecturer Joined the department of Mechanical Engineering, Faculty of Engineering, Garyounis University, Benghazi-Libya.

Duties: teaching the following subjects:

- Thermodynamics 1
- Thermodynamics 2
- Refrigeration and air conditioning 1
- Internal combustion engines laboratory
- Supervising final year projects

Others: Teaching the following Training courses:

- Gas Turbines Operation and Maintenance
- Pumps and Compressors Maintenance
- Refrigeration and Air Condition
- Preventive Maintenance

Publication (2008-2010)

2010

- Mohamed Salem, Susanne Staude, Ulf Bergmann and Burak Atakan "Heat flux measurements in stagnation point Methane/air flames with thermographic phosphors", Journal of Experiments in Fluids, 2010. DOI 10.1007/s00348-010-0910-4.
- Mohamed Salem, Susanne Staude, Ulf Bergmann and Burak Atakan "Heat flux from stagnation point hydrogen/methane/air flames: experiment and modeling", International Journal of Heat and mass Transfer (currently in review process).

2009

- Prof. Dr. B. Atakan, C. Eckert, M. Salem, Dr. U. Bergmann, Dr.C. Pflitsch Thermographische Phosphore zur Messung von Oberflächentemperaturen hinter Flammen Methode, Herstellung und Anwendung VDI-Berichte Nr. 2056, 2009, 367-372.

2008

- M. Salem, U. Bergmann, B. Atakan " Heat Transfer From Flat Premixed Methane and Hydrogen Flames to Solid Walls: Experiment and Modeling" 6th International Seminar on Flame Structure September 14-17, 2008 Vrije Universiteit Brussel, Belgium.
- M.Salem, U. Bergmann, C. Pflitsch, B. Atakan "Wärmeübergang von laminaren Flammen auf Wände: Oberflächentemperaturmessung mit thermographischen Phosphoren und Modellierung" "Thermodynamik-Kolloquium" und "Ingenieurdaten" 24.-26. September 2008 Universität Erlangen-Nürnberg.

APPENDICES

APPENDIX A

MECHANICAL DRAWINGS

Appendix A Mechanical Drawings

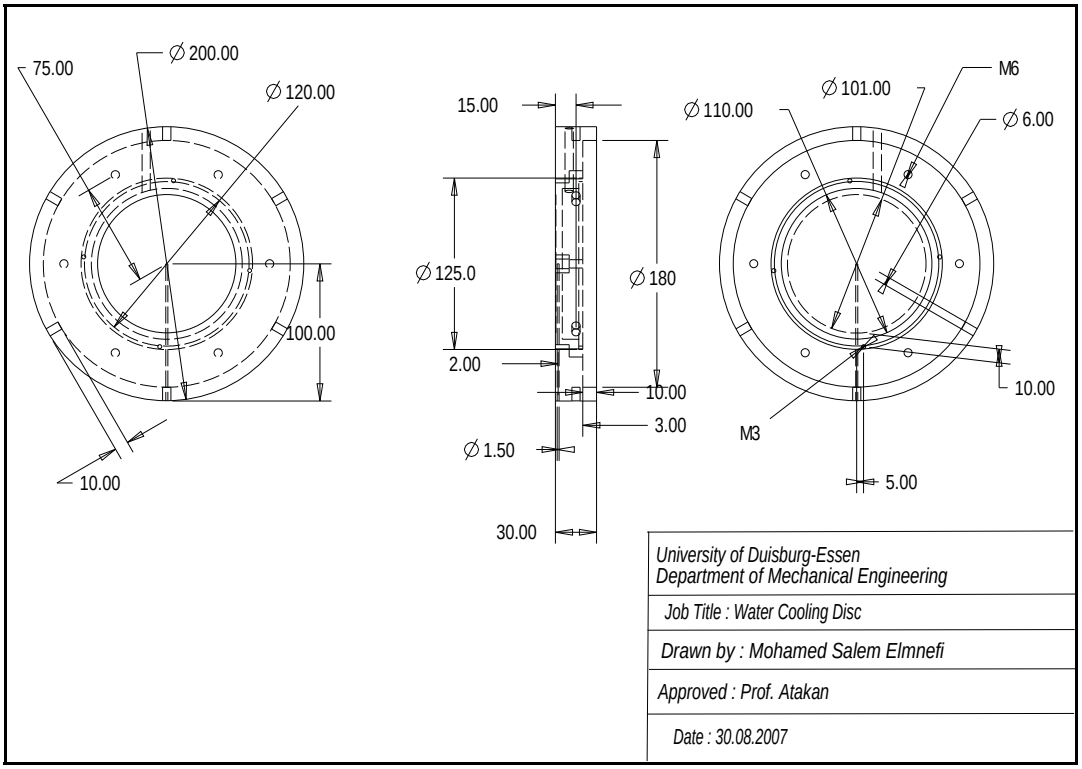

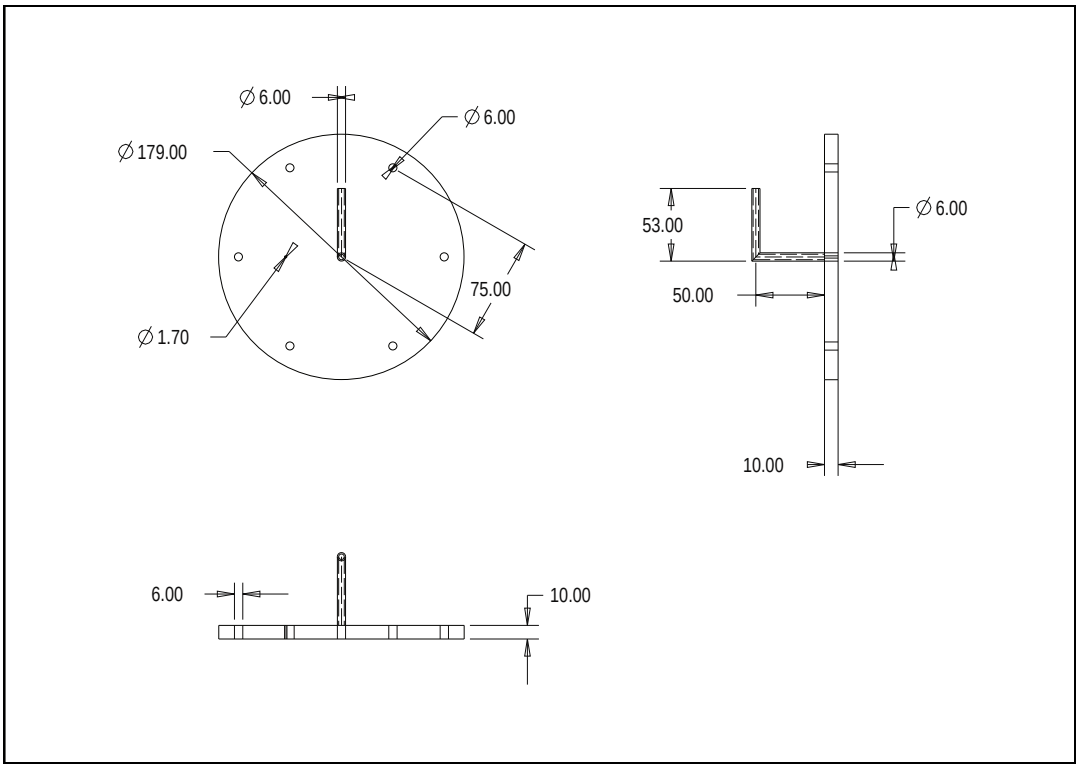

The water cooling disc and cover (first experimental setup)

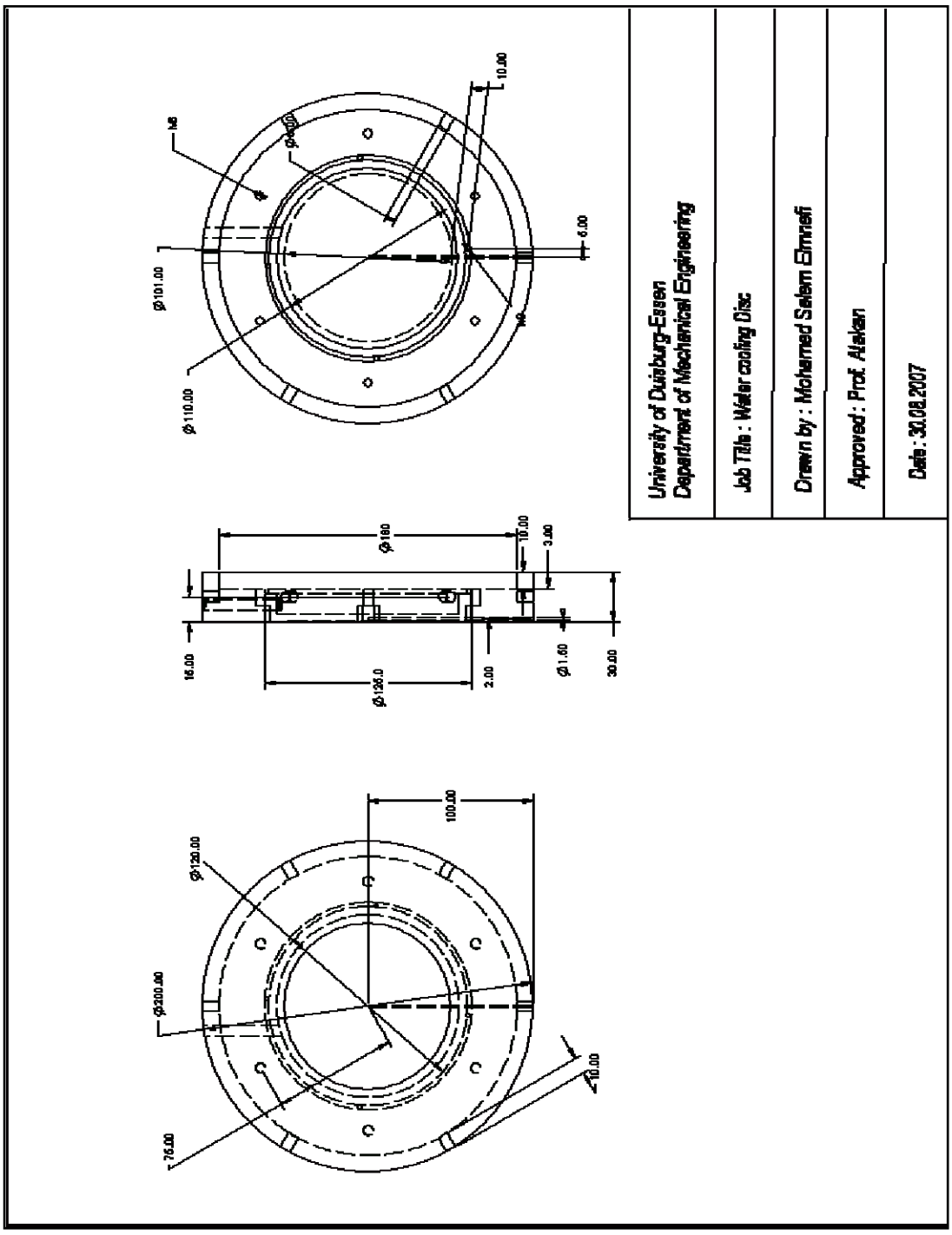

The water cooling disc (first experimental set up)

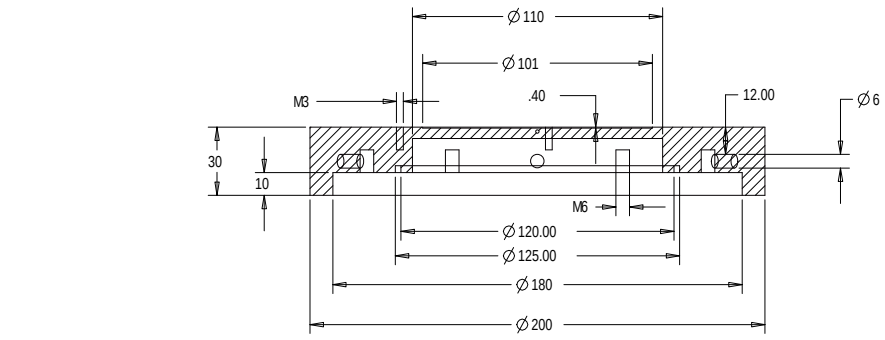

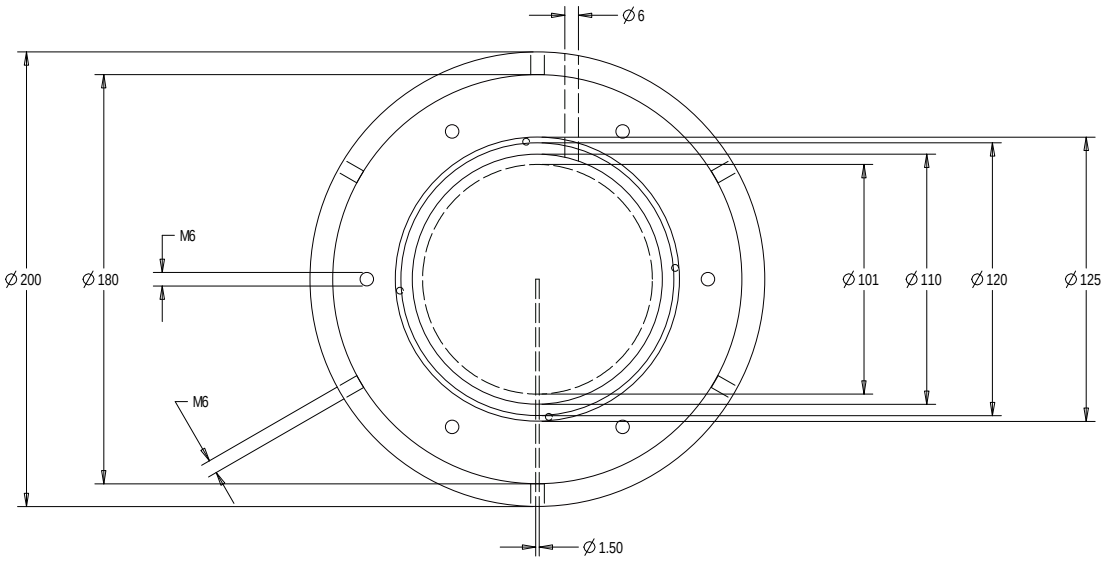

University of Duisburg-Essen *Department of Mechanical Engineering*
Job Title : Water Cooling Disc
Drawn by : Mohamed Salem Elmnefi
Approved : Prof. Atakan
Date : 30.08.2007

The water cooling disc (first experimental set up)

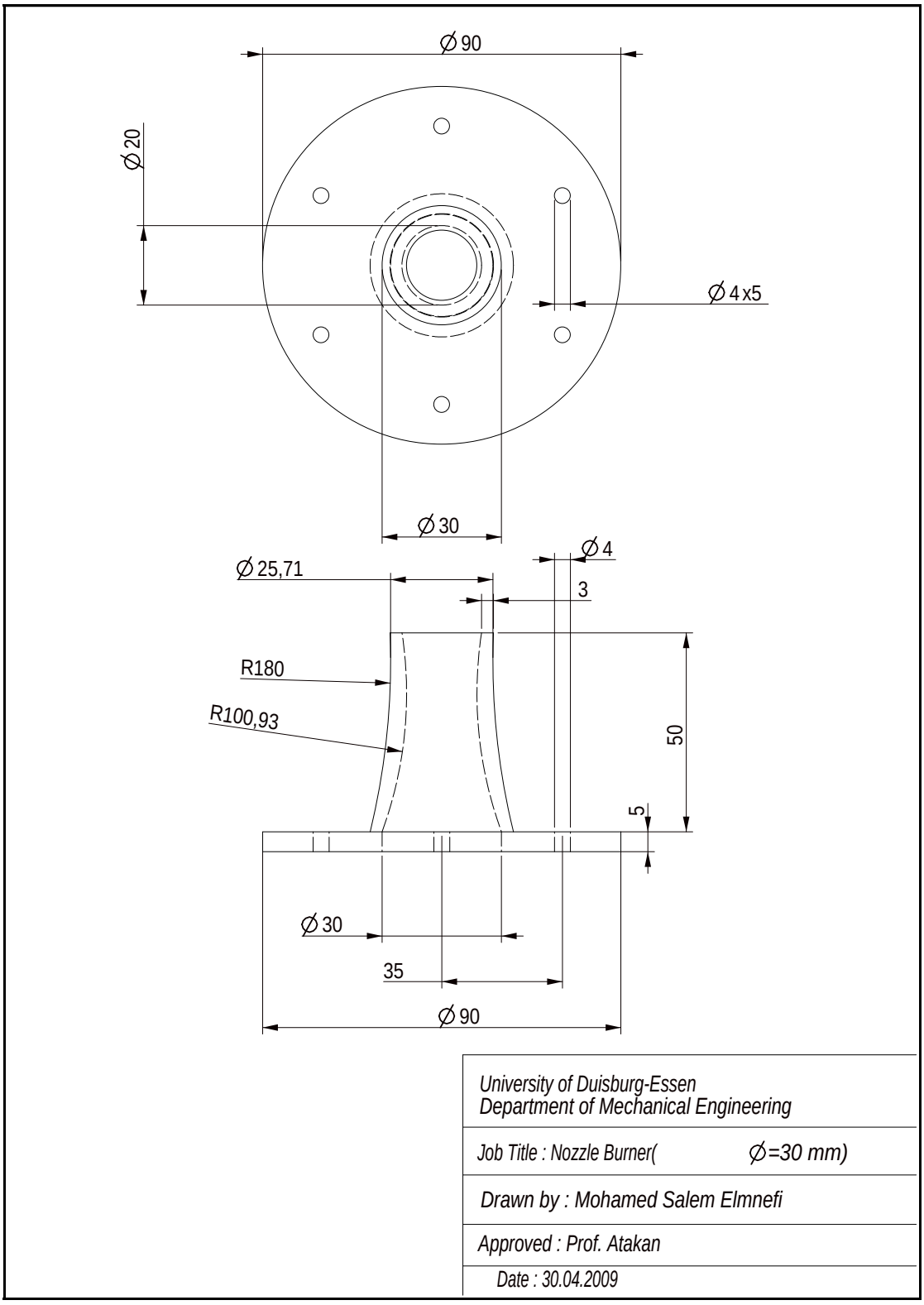

The nozzle burner (Ø = 30 mm)

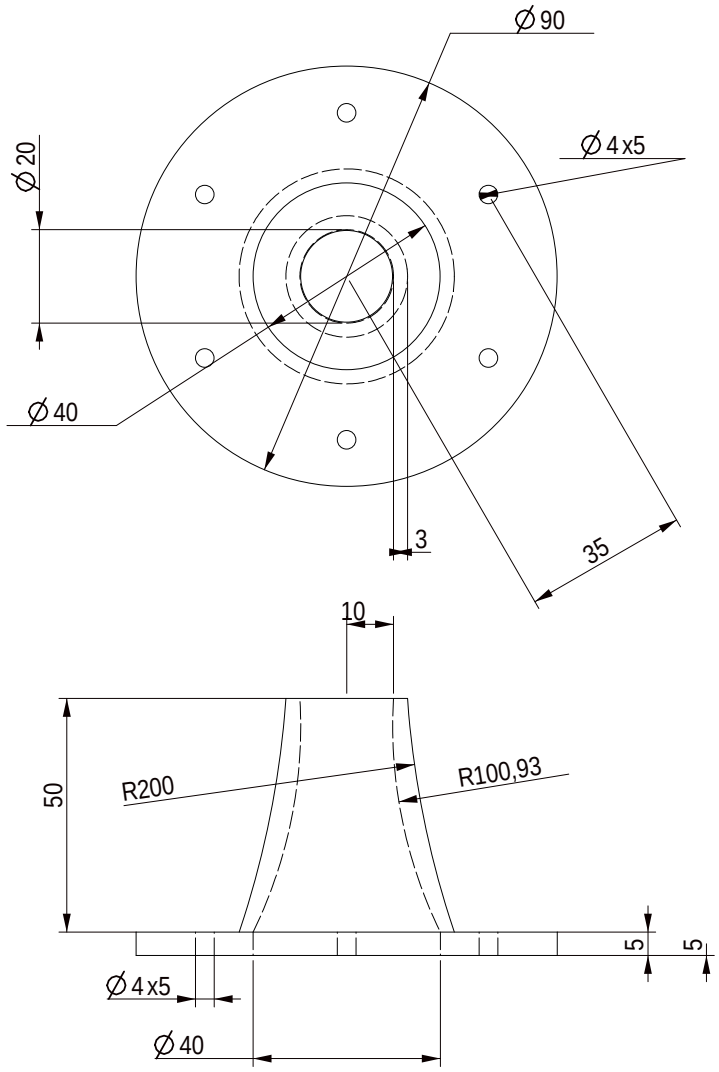

University of Duisburg-Essen *Department of Mechanical Engineering*
Job Title : Nozzle Burner (∅ = 40 mm)
Drawn by : Mohamed Salem Elmnefi
Approved : Prof. Atakan
Date : 30.04.2009

The nozzle burner (Ø = 40 mm)

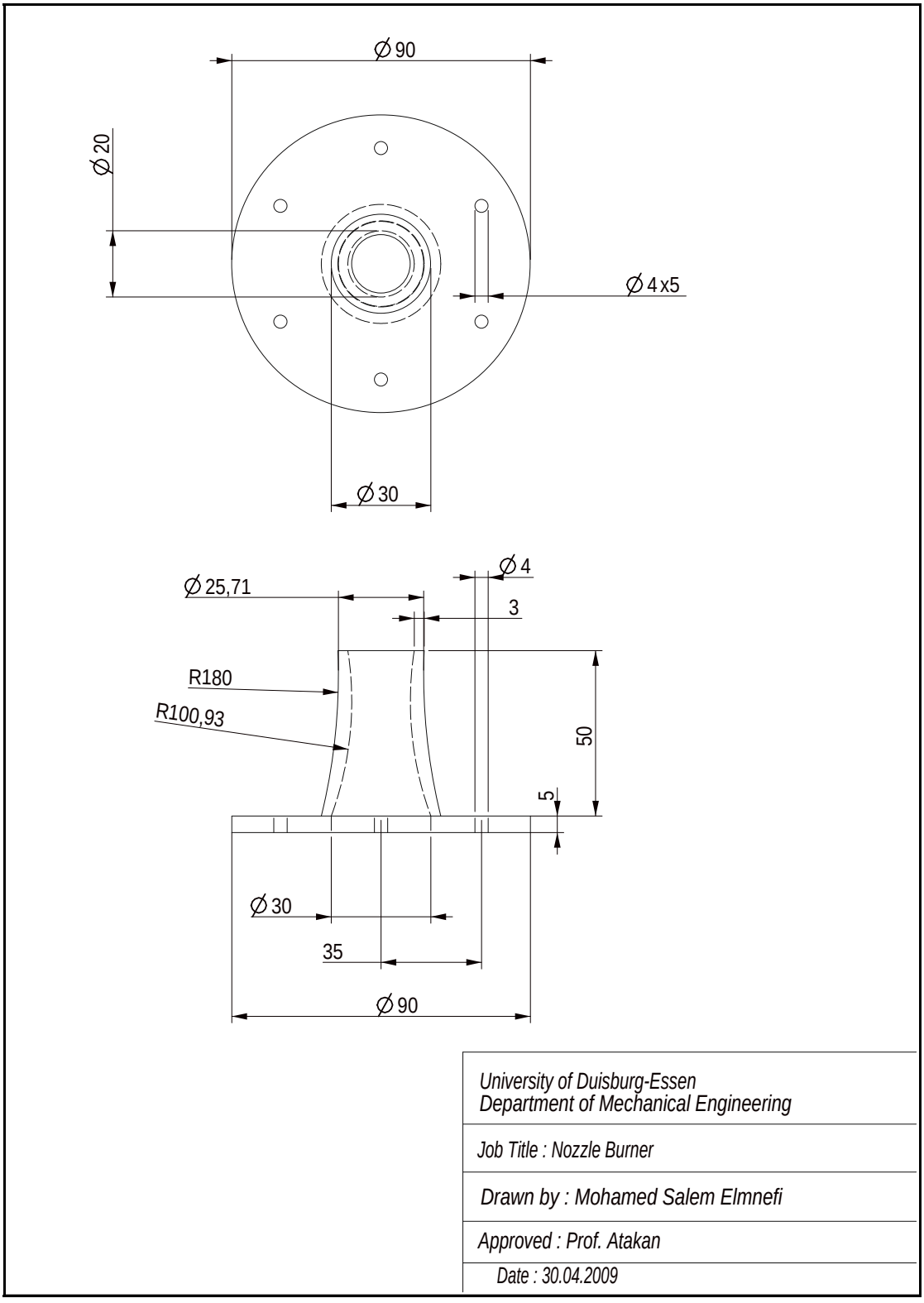

The nozzle burner

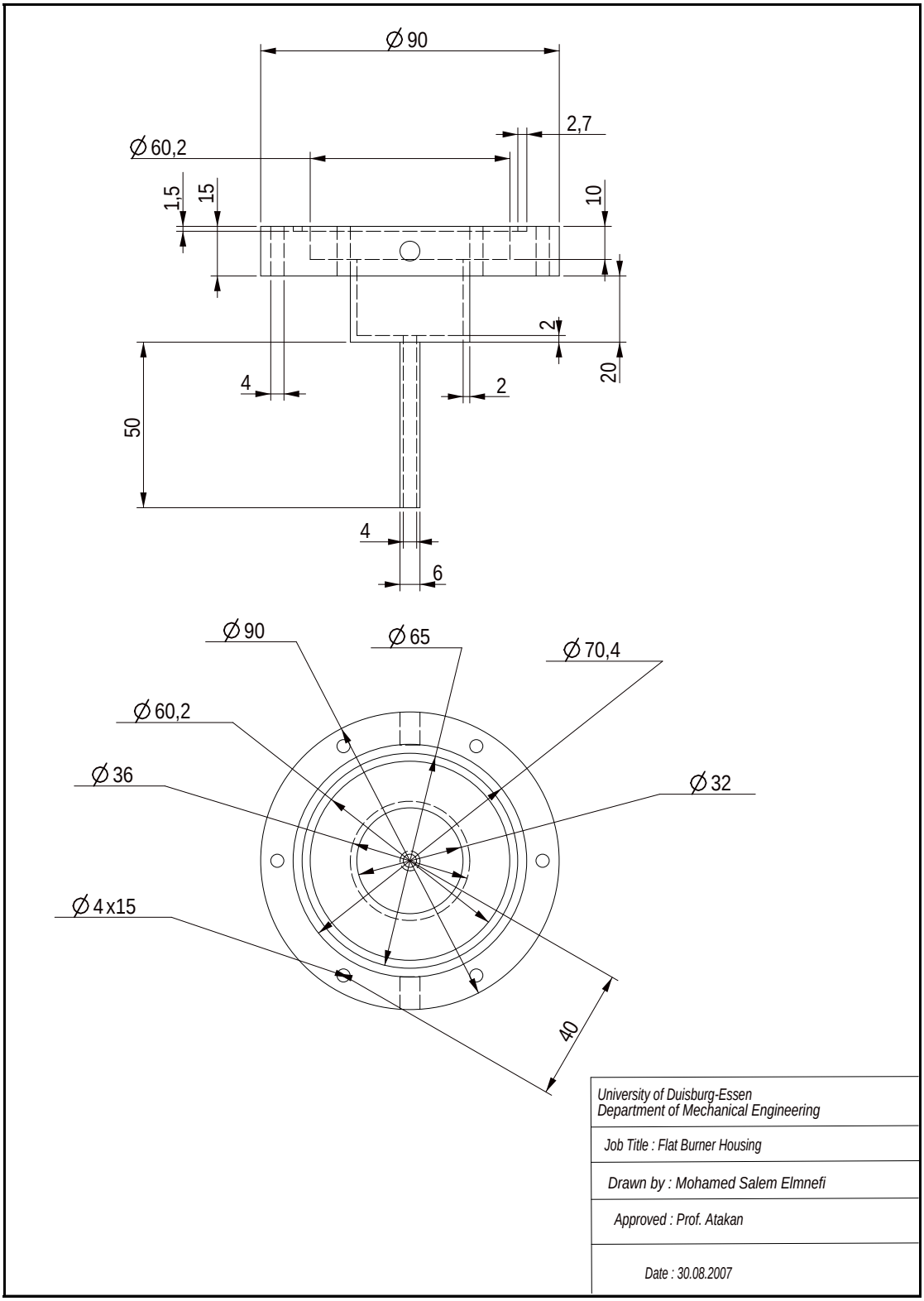

The flat burner housing

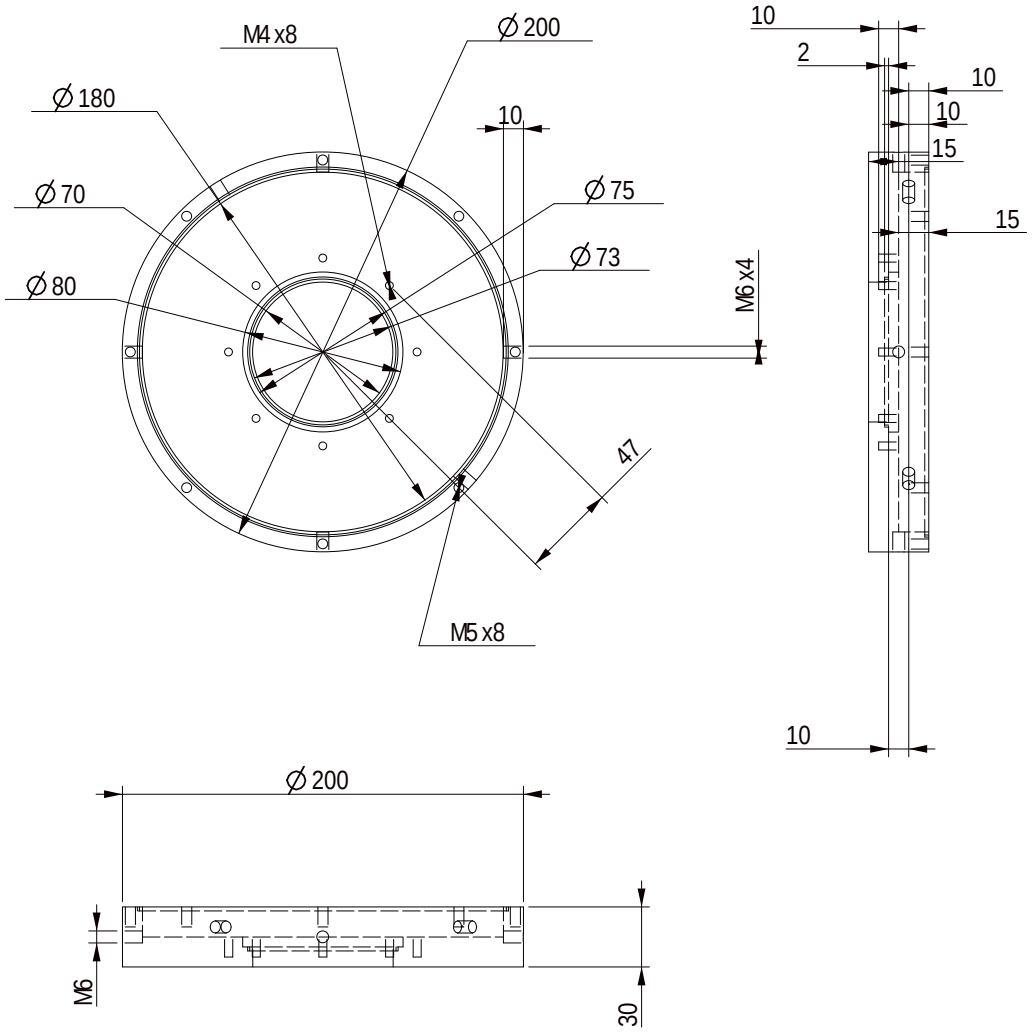

University of Duisburg-Essen *Department of Mechanical Engineering*
Job Title : Water steamed Disc
Drawn by : Mohamed Salem Elmnefi
Approved : Prof. Atakan
Date : 30.05.2008

The water streamed Disc

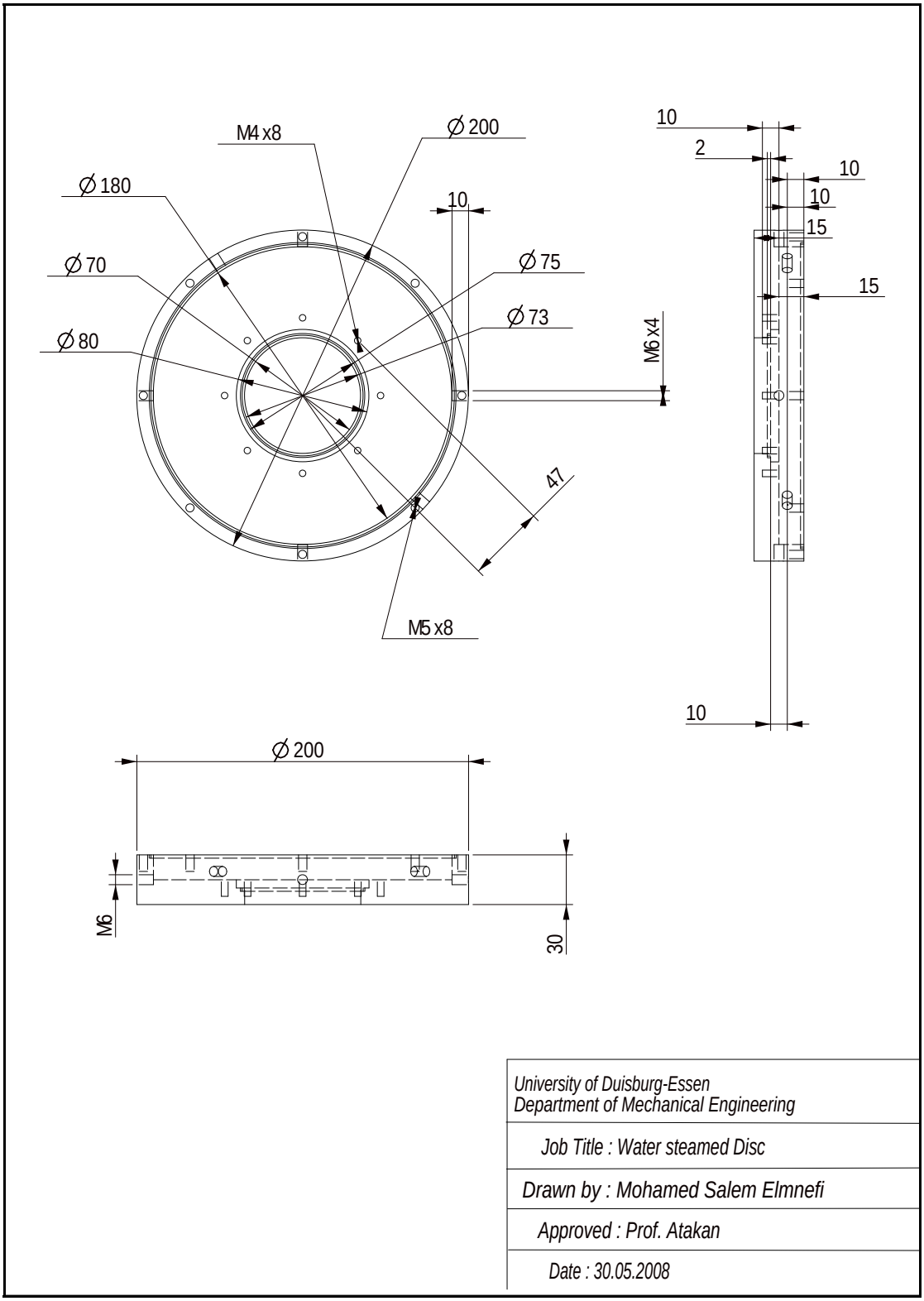

The water streamed Disc

APPENDIX B

EXPERIMENTAL SETUP PHOTOS

Appendix B Experimental setup photos

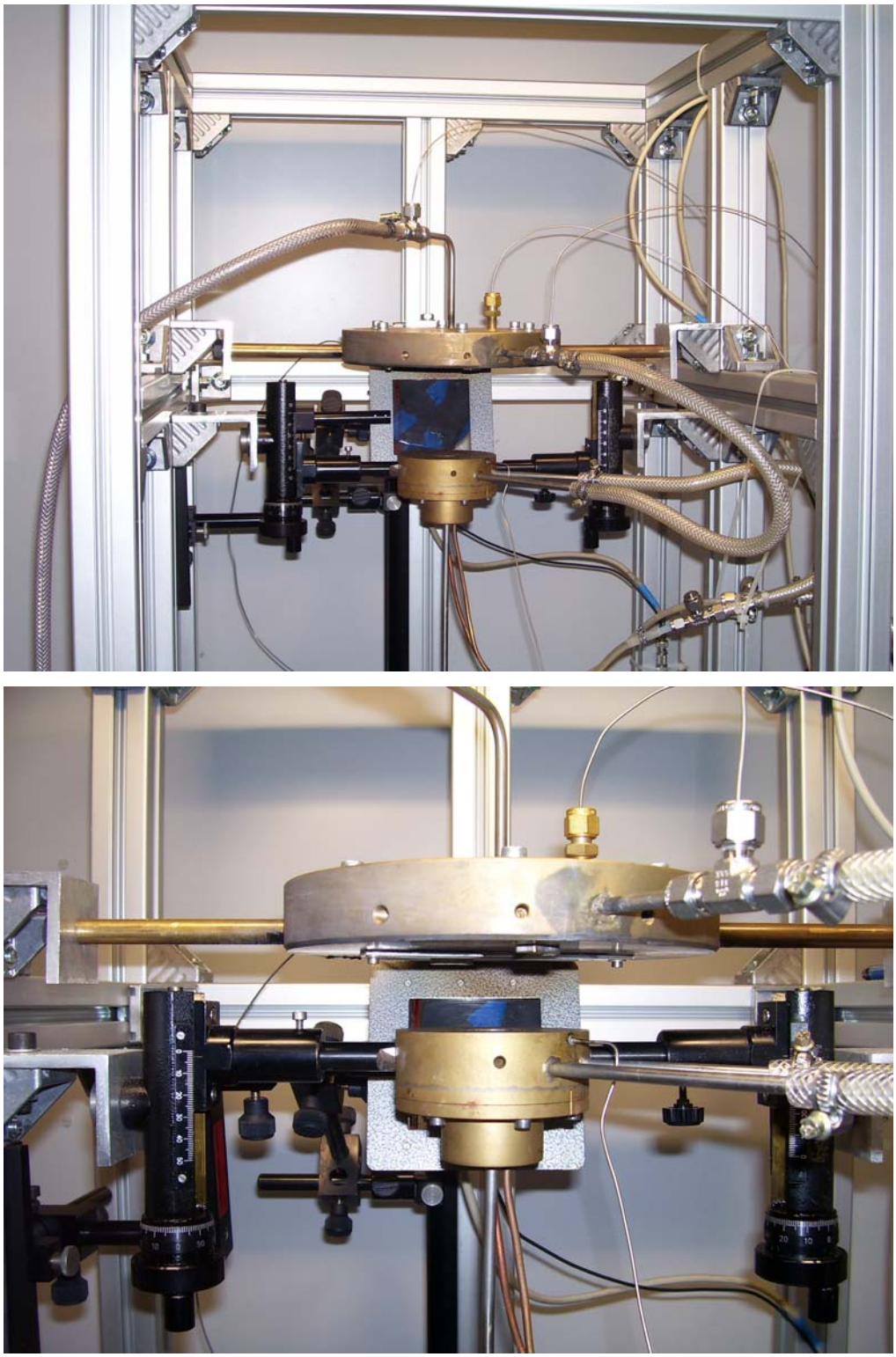

The flat burner (Ø = 30 mm)

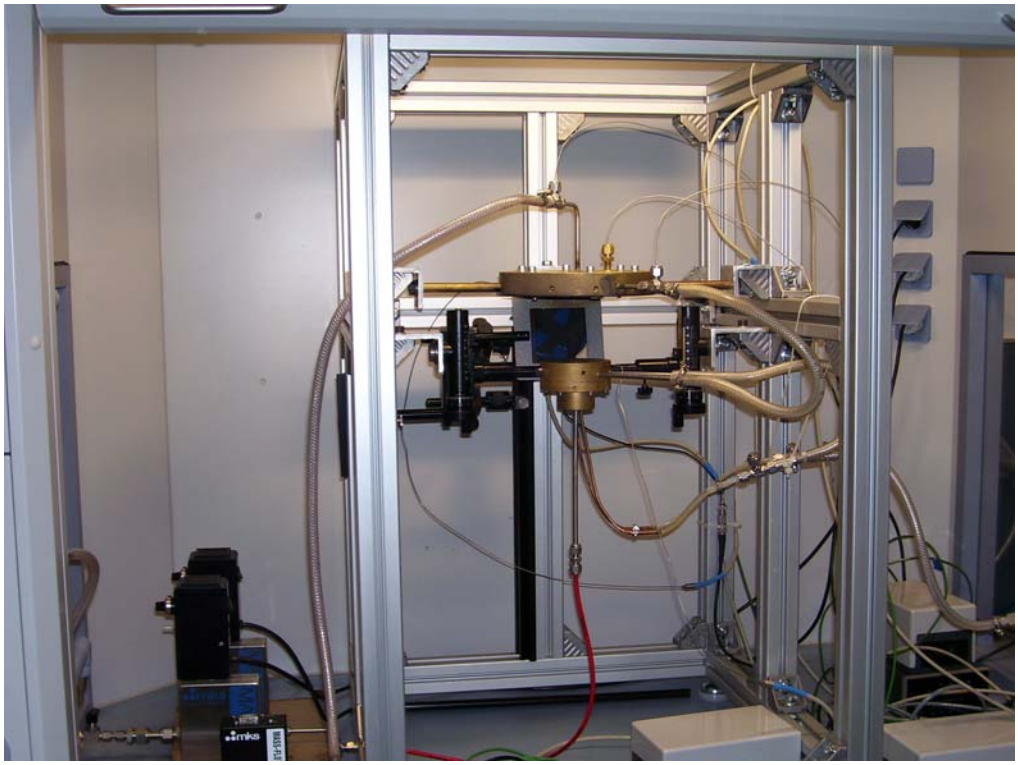

The first experimental setup

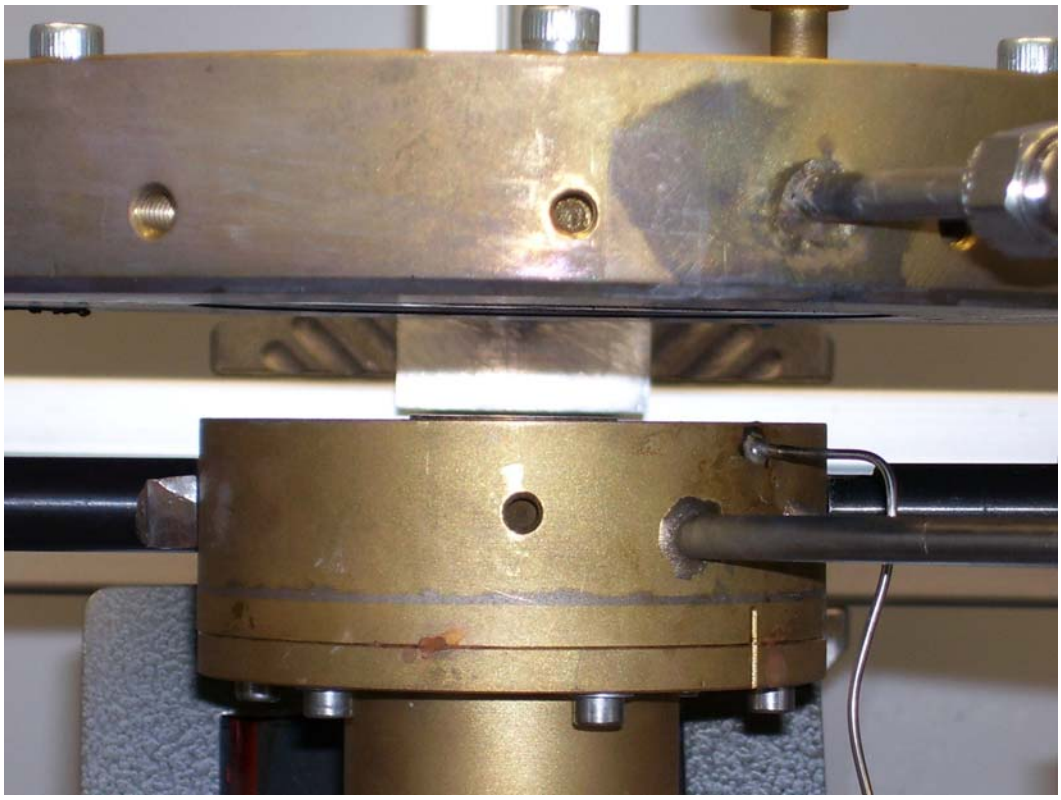

The first experimental setup

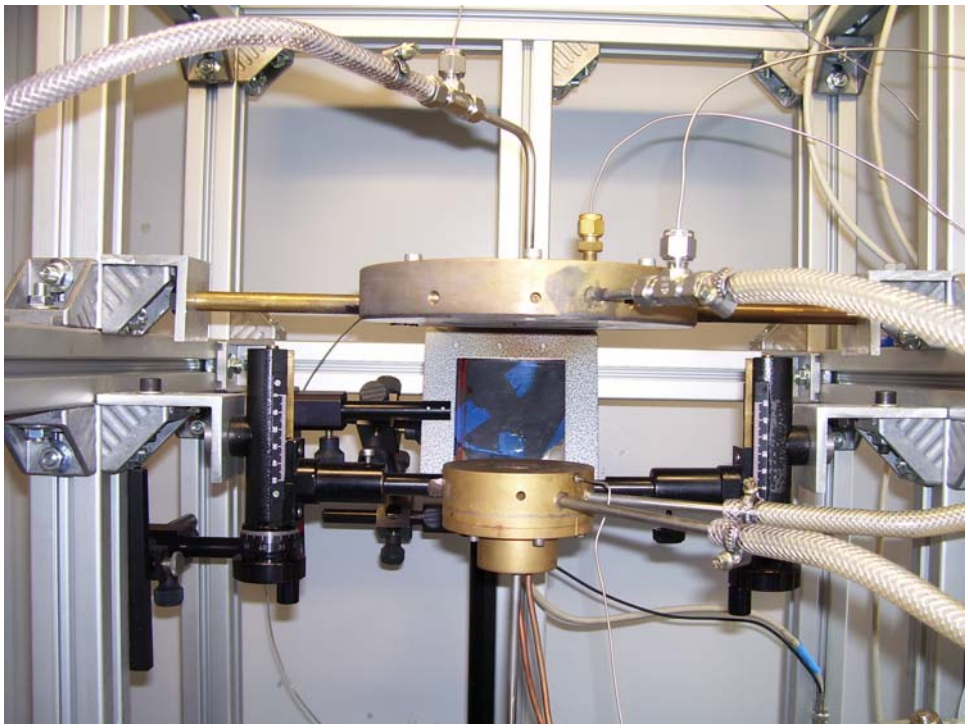

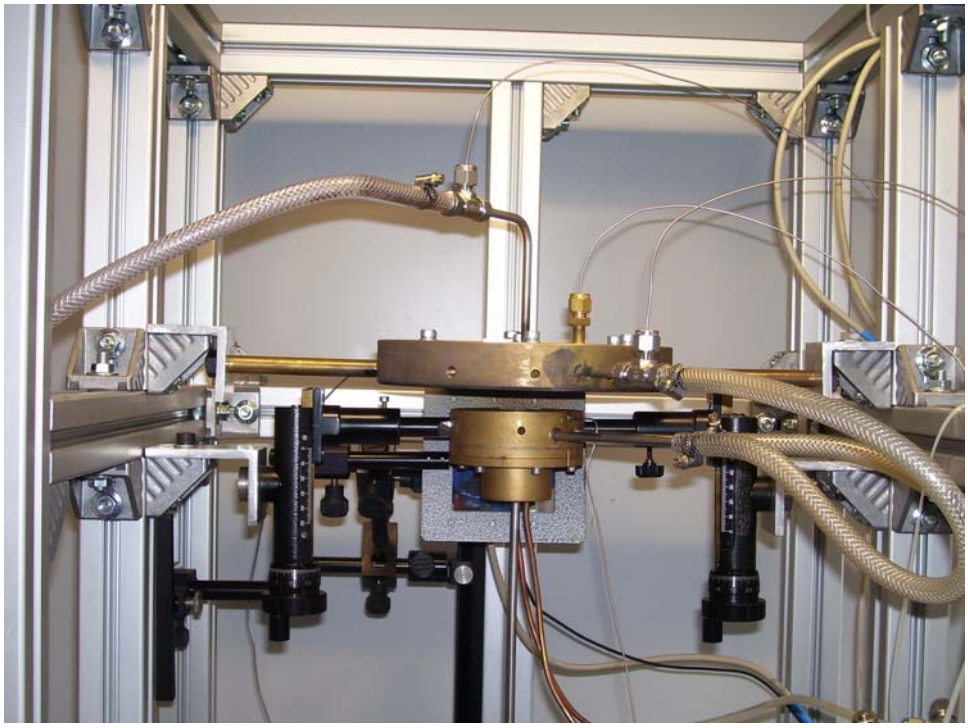

The water cooling system (the first setup)

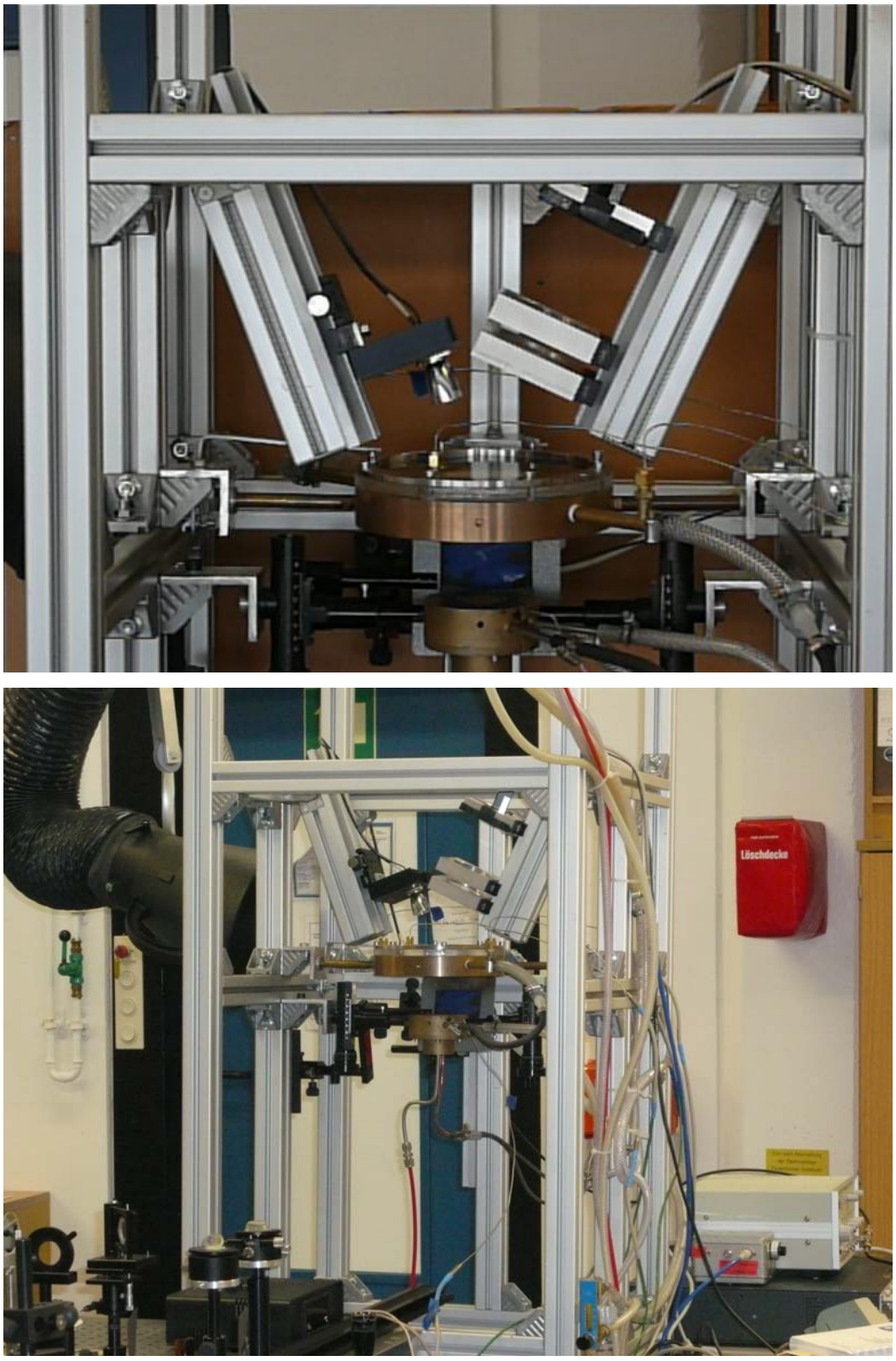

The new experimental setup (Laser and LED excitation)

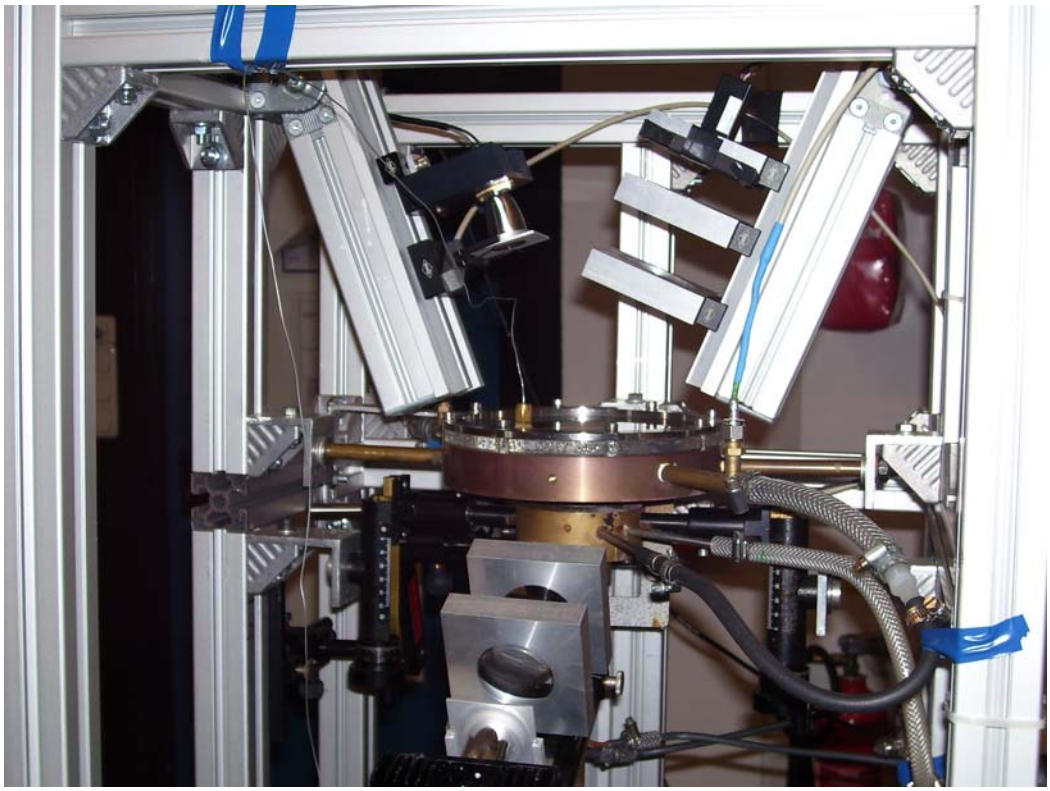

The new experimental setup (LED excitation on both sides)

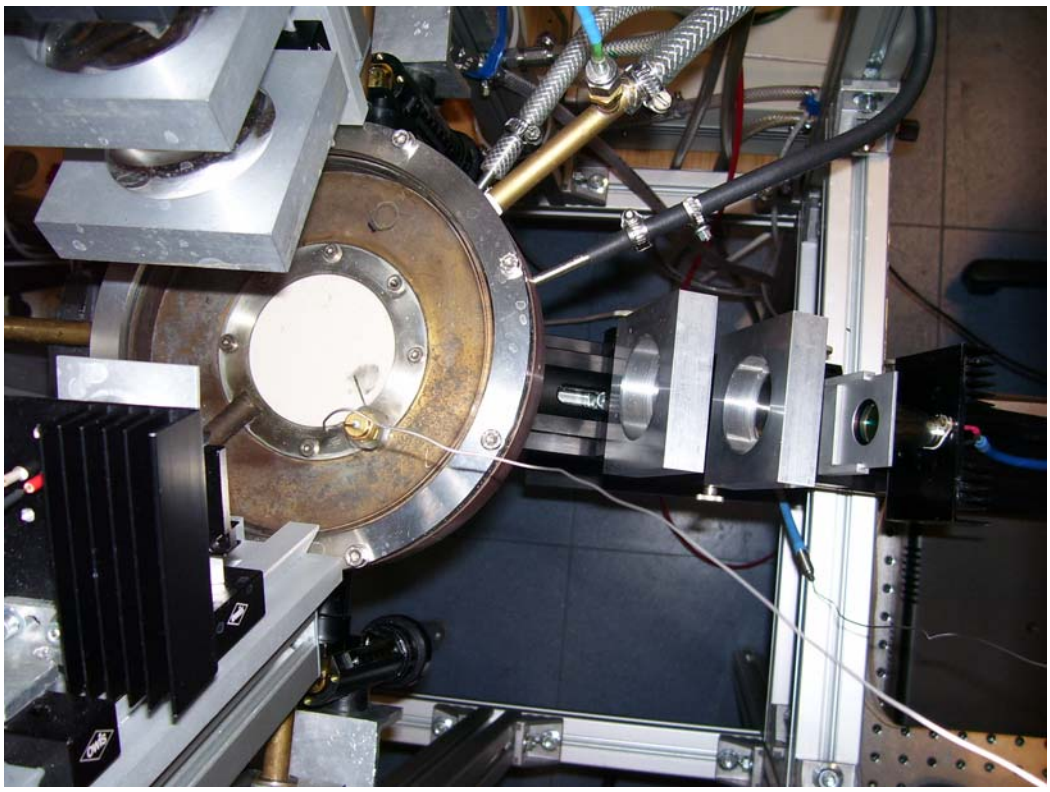

The new experimental setup (LED excitation on both sides)

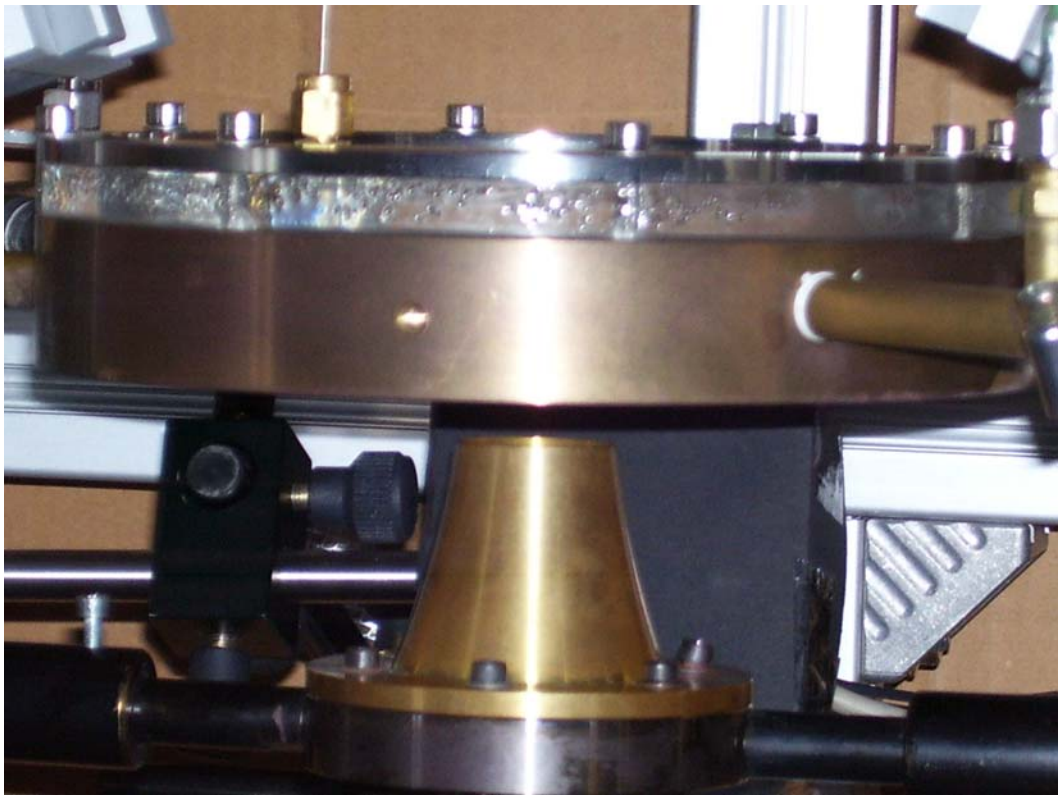

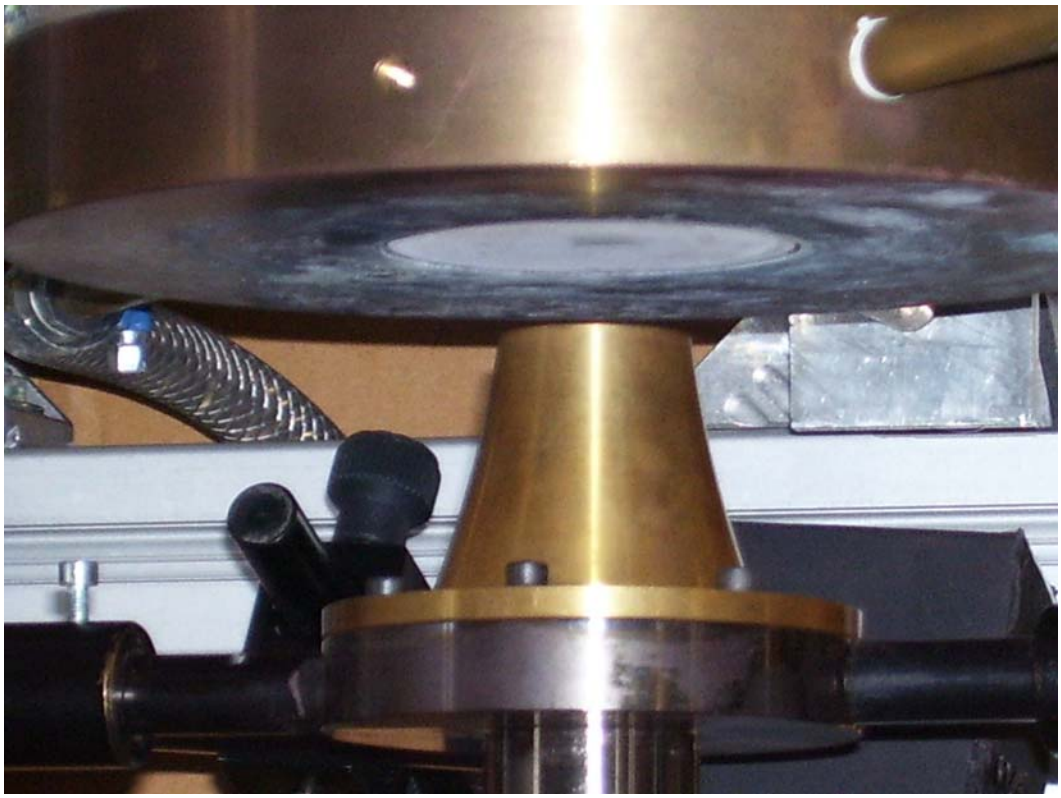

The nozzle burner and the coated ceramic plate

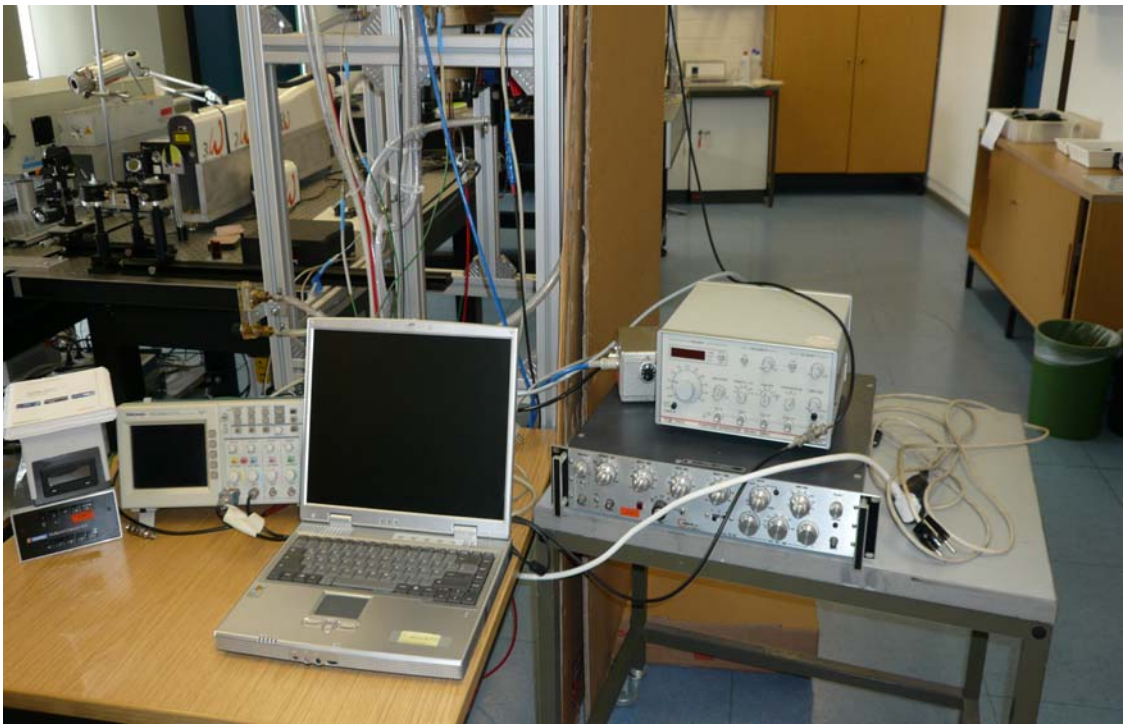

The experimental electronic devices

Both sides of Ceramic plate(Al_2O_3) coated with Cr^{+3}-doped Aluminum(Ruby)

APPENDIX C

LAMINAR FLAMES PHOTOS

Appendix C Laminar flames photos

(V = 0.1 m/s)

(V = 0.2 m/s)

(V = 0.3 m/s)

(V = 0.4 m/s)

The flat Burner

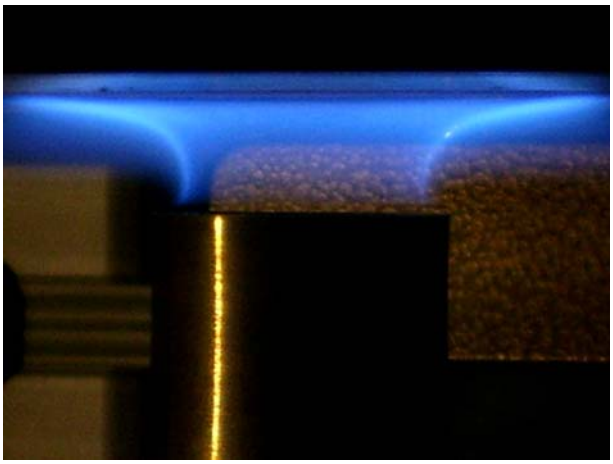

(V = 0.5 m/s)

(V = 0.7 m/s)

(V = 0.9 m/s)

(V = 1 m/s)

The nozzle Burner

Lebenslauf

Persönliche Daten

Name: Mohamed Salem Elmnefi
Geburtsdatum, -Ort: 16. Feb. 1964 Benghazi, Libyen
Familienstand: verheiratet
Staatsangehörigkeit: Libyen

Schulausbildung

1982: Schulabschluß: "Abitur", Salah Edinn Elayobi, Benghazi, Libyen.

Hochschulausbildung

1982–1986: Maschinenbaustudium an der Technishen Universität in Brega, Libyen, Abschluß: Bachelor of Mechanical and Production Engineering, Bacheloarbeit: Study of Cryogenic Systems.

1994-1996: Weiterführenden Studium an der Universität von Strathclyde, Glasgow, U.K. mit Abschluss Master of Science in Mechnical Engineering, Schwerpunkt: Comparison of Two-Phase flow Characteristics of Valves and Orifices in a Large Diameter horizontal Pipeline.

2007–2010: Doktorand an der Universität Duisburg-Essen, Lehrstuhl für technische Thermodynamik, Promotionsthema: Eine neue optische Methode zur Messung der Wärmestromdichte in laminaren Methan-Luft- und Wasserstoff-Methan-Luft-Staupunktflammen auf der Basis thermo- graphischer Phosphore.

Tätigkeiten

1986-1987: Arbeit als Ingenieur in Bereich Konstruktion and Wartung für die COMME (Staatöl-Energie-Versorgungsunternehmen) in Benghazi, Libyen.

1987-2000: Arbeit als Ingenieur in verschiedenen Bereichen für die AGOCO (Arabian Gulf Oil Company). Arbiet als Projektingenieur, betreuung mehrerer Projekte**.**

Ab 1997: berufsbegleitende Arbeit als Dozent an der Fakultät für Ingenieurwesen Abteilung Maschinenbau der Universität von Garyounis in Benghazi, Libyen.

2000-2007: Arbeit als Wissenschaftlicher Mitarbeiter an Fakultät für Ingenieurwesen Abteilung Mashinenbau der Universität von Garyounis in Benghazi, Libyen.

Veröffentlichungen

2009

Prof. Dr. B. Atakan, C. Eckert, M. Salem, Dr. U. Bergmann, Dr. C. Pflitsch Thermographische Phosphore zur Messung von berflächentemperaturen hinter Flammen Methode, Herstellung und Anwendung VDI-Berichte Nr. 2056, 2009, 367-372

2010

Mohamed Salem, Susanne Staude, Ulf Bergmann and Burak Atakan “Heat flux measurements in stagnation point Methane/air flames with thermographic phosphors”, Journal of Experiments in Fluids, 2010. DOI 10.1007/s00348-010-0910-4.

Mohamed Salem, Susanne Staude, Ulf Bergmann and Burak Atakan “Heat flux from stagnation point hydrogen/methane/air flames: experiment and modeling”, International Journal of Heat and mass Transfer (currently in review process).

Konferenzbeiträge

2008

- "Thermodynamik-Kolloquium" und "Ingenieurdaten"
  24.-26. September 2008
  Universität Erlangen-Nürnberg

  M. Salem, U. Bergmann, C. Pflitsch , B. Atakan(Lecture)
  Wärmeübergang von laminaren Flammen auf Wände: Oberfläch-entemperaturmessung mit thermographischen Phosphoren und Modellierung.

- Selected Topics in Combustion
  The Combustion Institute 20TH "JOURNEES D'ETUDES"
  of the Belgian Section
  May 6-8, 2008
  Universiteit Gent , Belgium

  M. Salem, U. Bergmann and B. Atakan: (Lecture) Heat Transfer From Flat Premixed Methane Flames to Solid Walls: Experiment and Modeling.

- 6th International Seminar on Flame Structure
  September 14-17, 2008
  Vrije Universiteit Brussel, Belgium

  M. Salem, U. Bergmann, B. Atakan (Lecture) Heat Transfer From Flat Premixed Methane and Hydrogen Flames to Solid Walls: Experiment and Modeling